POINT-CONTACT ANDREEV REFLECTION STUDIES ON SUPERCONDUCTORS

BY

XIN LU

DISSERTATION

Submitted in partial fulfillment of the requirements
for the degree of Doctor of Philosophy in Physics
in the Graduate College of the
University of Illinois at Urbana-Champaign, 2010

Urbana, Illinois

Doctoral Committee:

Professor James N. Eckstein, Chair
Professor Laura H. Greene, Director of Research
Professor Anthony J. Leggett
Professor Jen-Chieh Peng

Abstract

Point-contact Andreev reflection spectroscopy (PCARS) and planar tunneling spectroscopy are used to investigate the density of states and superconducting gap structure of several novel superconducting systems. Theoretical and experimental background is given with an emphasis on PCARS as applied to various unconventional superconductors, such as $NbSe_2$, the borocarbide family RNi_2B_2C (R=Lu, Y) and the recently-discovered, iron-based superconductors AFe_2As_2 (A=Ba, Sr) with both hole and electron doping.

The superconducting gap distribution observed from point-contacts on $NbSe_2$, with energies between 0.9 and 1.5 meV at 2 K, is consistent with the multigap scenario claimed by other experiments. The superconducting gap follows the BCS temperature dependence.

PCARS probes a small gap anisotropy in both $LuNi_2B_2C$ and YNi_2B_2C for the three major crystallographic orientations, while point-nodes are reported to exist in a and b axes and predicted to originate from the antiferromagnetic fluctuations due to nesting structure on the 17th band Fermi surface. This can be explained by the other Fermi surface sheets, with $\Delta \geq 2.1$ meV in [100] direction, masking the point-node feature and resulting in a small gap anisotropy, as observed in our PCARS. A large tunneling cone in PCARS measurements, which would smear the differences in three directions, may be another origin of the observed small gap anisotropy.

For the Fe-122 family of the iron-based superconductors, Andreev reflection is present for PCARS on $(Ba_{0.6}K_{0.4})Fe_2As_2$ and $Ba(Fe_{0.9}Co_{0.1})_2As_2$ crystals but measured conductances are distinct. A V-shape conductance valley (VCV) feature is observed for point-contacts on $Sr(Fe_{0.9}Co_{0.1})_2As_2$ and $(Sr_{0.6}Na_{0.4})Fe_2As_2$ crystals. This VCV feature is also observed for the non-superconducting parent compound $BaFe_2As_2$ and the superconducting $(Ba_{0.6}K_{0.4})Fe_2As_2$ crystals. The coexistence of phase-separated magnetic and superconducting orders on the mesoscopic scale is considered to explain the range of behaviors in the superconducting samples.

Acknowledgments

First I would like to thank my advisor, Prof. Laura Greene, who made this work possible with her great assistance and thoughtful advices. I will always remember her enlightening education and kind patience to transform me into an independent researcher. Under years of advisory from her, I am forced to plan the experiment and analyze the data more carefully with her sharp opinions and comments. She always encourages me to be more self-confident whenever presenting the data in the conference or talking with other scientists, even though I am still not as good as she expected. I deeply appreciate all the precious supports she has given me, even with her tight schedule, from magically obtaining the samples right the next day after our discussion to recommending me to every possible career opportunity without any reservation. Meanwhile, I always benefit a lot from patient instructions and stimulating discussions with Prof. Wan Kyu Park from the very beginning moment of me joining the group and I am really indebted to him. I appreciate his continuing support despite of the frustration I may cause sometimes, especially before I just started to behave like an experimentalist.

I'd also like to thank other group members with whom I have always had the pleasure to work either short term or long term. I enjoyed valuable advice, discussions and collaborations through the long journey of graduate study with Matt Brinkley, Heiko Stalzer, Julien Albert Ansermet, Jiongyi Tan, Veronica Jacome, Ryan Murphy, Yi-Hsuan Lin, Zhen-wah Tan, Adam

Ahmed, Anuj Tejpall, Hamood Arham ,Cassandra Hunt and Jose Garmilla. Special thanks are given to Ryan Murphy who constructed the new electronic circuit, which guaranteed the correctness of tunneling measurements in this work.

The work relies heavily on the smooth function of facilities at the center for Microanalysis of Materials and other Frederick-Seitz Materials Research Lab divisions. The training and generous suggestions from Mauro Sardela, Vania Petrova, Scott MacLaren, Rick Haasch, Bharat Sankaran and Tony Banks are indispensable for the success of this work. In addition, I am honored to thank Prof. Russ Giannetta, Prof. Jim Eckstein, Jasung Ku, Huiqiu Yuan and Elbert Chia for their invaluable support and immediate response.

Finally, I want to thank my wife, brother and parents for their priceless support and inspiration even when, sometimes, I was in a blue mood and lost my confidence to move forward.

All the work is supported by the U.S. Department of Energy under Award No. DEFG02-07ER46453 through the Frederick Seitz Materials Research Laboratory and the Center for Micro-analysis of Materials at UIUC. Meanwhile, I would thank the support from National Science Foundation DMR 07-06013.

Table of Contents

List of Figures . . . . . **vii**

Chapter 1 Introduction **1**
1.1 History & Background 1
1.2 Microscopic Theory of Superconductivity 6
1.3 Transport across the Interface 9
1.3.1 Tunneling 10
1.3.2 Andreev Reflection 13
1.3.3 BTK Model and Its Extension 21

Chapter 2 Planar Tunneling and Point-contact Andreev Reflection Spectroscopy **27**
2.1 Planar Tunneling 27
2.1.1 Junction Preparation and Measurement 28
2.1.2 NIS and SIS Junction 35
2.1.3 2^{nd} Harmonics and Phonon Structure 39
2.2 Point-contact Andreev Reflection Spectroscopy (PCARS) . . . 43
2.2.1 Configurations for PCARS 43
2.2.2 Different Contact Regimes 47
2.2.3 PCARS Diagnostics 50

Chapter 3 PCARS on $NbSe_2$ **58**
3.1 Introduction 58
3.2 Experimental Results and Discussions 61

Chapter 4 PCARS on Borocarbides **67**
4.1 Introduction 67
4.2 PCARS on $LuNi_2B_2C$ 70
4.2.1 Sample Preparation 70
4.2.2 Surface Treatment and Characterization 73
4.2.3 Experimental Results and Analysis 75
4.3 PCARS on YNi_2B_2C 79
4.4 Discussions 83

Chapter 5 PCARS studies on Iron-based Superconductors **89**
5.1 Introduction 89
5.2 PCARS on (Ba,K)Fe_2As_2 95
5.3 PCARS on $Ba(Fe_{0.9}Co_{0.1})_2As_2$ 102
5.4 PCARS on $(Sr_{0.6}Na_{0.4})Fe_2As_2$ & $Sr(Fe_{0.9}Co_{0.1})_2As_2$ 109
5.5 Discussions 114

Chapter 6 Concluding Remarks **119**

References **122**

List of Figures

1.1 Phase diagram of the cuprate superconductors 3
1.2 The order parameters for (a) s-wave (b) d-wave and (c) extended $s\pm$ superconductors. 4
1.3 Superconducting critical temperature (T_c) as a function of time in various classes of superconductors. 5
1.4 (a) Calculated dispersion relations for quasiparticle excitations in the superconducting state; (b) BCS gap as a function of temperatures; (c) Quasiparticle density of states dependent on the energy. 7
1.5 Schematic diagram of a typical quantum tunneling problem. . 10
1.6 Electron band illustration of fabricated junctions biased with voltage V for (a) a NIN sandwich structure; (b) a NIS structure. 12
1.7 (a) Normal specular reflection; (b) Andreev reflection for an electron incident at the normal metal and superconductor interface. 15
1.8 Multiple Andreev reflections induce (a) geometric bound states; (b) Andreev bound states (ABS) 19
1.9 Schematic diagram of transport processes across the N/S interface in the BTK model. 21
1.10 Calculated G(V) conductance curves after normalization for a N-S contact as a function of (a) barrier strength parameter Z; (b) quasiparticle smearing parameter Γ 23
1.11 Schematic Illustration of reflection and transmission process across the Normal metal and d-wave Superconductor interface. 24
1.12 Calculated G(V) curves for a contact junction between a normal metal and a d-wave superconductor as a function of the barrier strength Z, with the interface in the (a) gap antinodal direction [100]; (b) gap nodal direction [110]. 25

2.1 Illustration of different PVD thin film growth techniques: (a) Thermal evaporator; (b) Electron-beam evaporator; (c) Magnetron sputtering. 29

2.2 Illustration of the tunnel junction fabrication viewed from the top and cross-section. 33
2.3 Schematic electronic circuit for the differential conductance measurement. 34
2.4 Al-AlO_x-Pb tunnel junction measurement. 36
2.5 Nb(Al)-AlO_x-Ag junction tunneling conductance measurement and analysis. 37
2.6 Nb(Al)-AlO_x-Pb tunnel junction measurement. 39
2.7 2nd harmonic measurement of Al-AlO_x-Pb and Nb(Al)-AlO_x-Pb tunnel junctions to indicate the phonon spectra. 41
2.8 (a) Schematic illustration of the needle-anvil type point-contact setup; (b) the optical microscopic image of a Au tip prepared by the electrochemical etching method. 44
2.9 Differential micrometer PCARS probe: (Top) the illustration of probe design; (Bottom) the picture of built probe. 46
2.10 Schematic illustration of the contact junction in different regimes: (a) ballistic (Sharvin) limit when $d \ll l_{el}$; (b) diffusive regime where $l_{el} < d < l_{ie}$; (c) thermal regime when $l_{el} \gg d$ 48
2.11 Electron distribution function with a voltage bias, V, for the ballistic point-contact in both electrodes and the constriction. 49
2.12 Normalized G(V) curves of Au/Li_2Pd_3B(polycrystal) point-contact junctions with fine structures. 51
2.13 G(V) evolution of Au/Pb film point-contact junctions as a function of the contact resistance to show the effect of the surface oxide. 54
2.14 Various dip structures observed in the point-contact junctions between the Au tip and Nb film. 55
2.15 Temperature dependent G(V) curves of a Au tip/Nb film point-contact junction with a double-dip structure. 56
2.16 The calculated curves for the normal metal and superconductor point-contact junctions with the critical current effect. . . 57

3.1 Crystal structure of $NbSe_2$ and its Fermi surface sheets in the 2-D Brillouin zone. 59
3.2 Temperature dependent in-plane electrical resistance of the $NbSe_2$ single crystal. 61
3.3 Different differential conductance curves for the Au/$NbSe_2$ contact junctions with some contacts in the diffusive regime where dips can be observed shown with arrows. 62
3.4 Au/$NbSe_2$ point-contact junction G(V) curves and the BTK superconducting gap evolving with temperatures 63
3.5 G(V) curves for multiple Au/$NbSe_2$ point-contact junctions at $T \sim$2 K and the simulated BTK gap distribution. 65

4.1 Crystal unit cell of RNi_2B_2C and its Fermi surface shown in the Brillouin's zone. The superconductivity critical temperature, T_c, and antiferromagnetic Neel temperature, T_N, for RNi_2B_2C family is shown as a function of the De-Gennes factor, $dG = (g-1)^2 J(J+1)$. 68
4.2 Temperature-dependent electrical resistance of $LuNi_2B_2C$ crystals normalized to the value at 300 K. 71
4.3 X-ray diffraction (XRD) 2θ-ω scans for the prepared crystals with different crystallographic orientations. 72
4.4 Nonspectroscopic G(V) curves for Au-$LuNi_2B_2C$ point-contact junctions. 73
4.5 Auger electron spectroscopic investigation on the surface element compositions for $LuNi_2B_2C$ cyrstals with different surface preparation methods. 74
4.6 Normalized differential conductance spectra of the Au/$LuNi_2B_2C$ point-contact junctions along three major directions as a function of temperature. 76
4.7 Temperature dependence of the superconducting gap extracted from one-gap BTK model in $LuNi_2B_2C$ along (a) [001], (b) [110] and (c) [100] directions in comparison with the standard BCS curve. 77
4.8 Histogram counts for the superconducting gap values extracted from one-gap BTK model measured in (a) [001], (b) [110], and (c) [100] directions. 78
4.9 Temperature dependence of the superconducting gap extracted from one-gap BTK model along three major directions for the second set of $LuNi_2B_2C$ crystals. 80
4.10 Temperature-dependent electrical resistance for the YNi_2B_2C crystals. 81
4.11 Normalized differential conductance spectra of the Au/YNi_2B_2C point-contact junctions along (a) [001], (b) [110] and (c) [100] directions as a function of temperature. 82
4.12 Temperature dependence of the superconducting gap extracted from one-gap BTK model in YNi_2B_2C along (a) [001], (b) [110] and (c) [100] directions in comparison with the standard BCS curve. 83
4.13 (a) The experimental (top) and theoretical (bottom) FS topology of $LuNi_2B_2C$. (b) The observed FS from ARPES with symmetrization. (c) The superconducting gap sizes on different FS sheets probed by ARPES. 85
4.14 Calculated peak position Δ_{Peak}/Δ_0 for the conductance curves as a function of the tunneling cone Θ_D for different surface orientations at a low temperature, with an (a) s+g pairing symmetry and (b) anisotropic s-wave gap both with point-nodes. 87

5.1 Schematic crystal structure of LaFeAsOF and the common Fe-As corrugated layer of all iron-based superconductors. . . . 90
5.2 (a) Band structure calculation for LaFeAsO and $BaFe_2As_2$. (b) the Fermi Surface sheets for 10% e-doping LaAsFeO from a topview of the Brillouin zone. (c) The Fermi Surface of the 10% Co-doping $BaFe_2As_2$ in the 3D Brillouin zone. 92
5.3 Temperature-dependent electrical resistance and magnetic moment measurements of the $(Ba_{0.6}K_{0.4})Fe_2As_2$ crystals. 95
5.4 (Left) SEM (Right) AFM images on cleaved (Ba,K)Fe_2As_2 surface. 96
5.5 G(V) curves for different Au/$(Ba_{0.6}K_{0.4})Fe_2As_2$ point-contact junctions at low temperatures T∼2 K. 97
5.6 Temperature dependence of the conductance curves G(V) for a Au/(Ba,K)Fe_2As_2 point-contact junction on a freshly-cleaved surface. 98
5.7 (a) A typical G(V) curve for the Au/(Ba,K)Fe_2As_2 point-contact junction and the extrapolated background baseline; (b) The normalized conductance data and best BTK fitting curve. 99
5.8 (a) Fermi surface topology from the band structure calculation. (b) Gap values for different bands from ARPES measurements. 100
5.9 The differential G(V) curves without double-peak structure for the Au/(Ba,K)Fe_2As_2 point-contact junctions and the magnetic field dependence. 101
5.10 Temperature-dependent electrical resistance and magnetic moment measurements for the $Ba(Fe_{0.9}Co_{0.1})_2As_2$ crystals. . . . 103
5.11 Different normalized G(V) curves for Au-$Ba(Fe,Co)_2As_2$ point-contact junctions at low temperatures. 104
5.12 The temperature-dependent normalized G(V) curves with ZBCP for a Au-$Ba(Fe,Co)_2As_2$ point-contact junction. 105
5.13 G(V) curves, for a Au-$(Fe,Co)_2As_2$ point-contact junction, as a function of magnetic field applied in the c-axis direction at T∼2 K. 106
5.14 Double-peak features rarely observed for Au-$(Fe,Co)_2As_2$ point-contact junctions. 107
5.15 X-ray photoelectron spectra (XPS) of (a) Fe 2p-orbit and (b) Se 3d-orbit for the freshly cleaved $Ba(Fe,Co)_2As_2$ crystal and uncleaved crystal exposed in the air for a whole day. 108
5.16 Temperature-dependent electrical resistance measurements for the $(Sr_{0.6}Na_{0.4})Fe_2As_2$ and $Sr(Fe_{0.9}Co_{0.1})_2As_2$ crystals. 110

5.17 V-shape conductance valley (VCV) and the universal power law fit for the point-contact junctions on different crystals: (a) $(Ba_{0.6}K_{0.4})Fe_2As_2$; (b) $(Sr_{0.6}Na_{0.4})Fe_2As_2$; (c) $Sr(Fe_{0.9}Co_{0.1})_2As_2$; (d) $BaFe_2As_2$. 111
5.18 The VCV feature for a Au/$Sr(Fe_{0.9}Co_{0.1})_2As_2$ point-contact junction as a function of magnetic field applied perpendicular to the ab plane at T$\sim$2 K. 113
5.19 Two examples of the temperature dependence of the normalized conductance curves taken on two locations (a) and (b) on a non-superconducting parent compound $BaFe_2As_2$ crystal. . . 114
5.20 Schematic diagram of Andreev reflection across the N/S interface for the $s\pm$ iron-pnictide. 115
5.21 Calculated conductance curves of a point-contact junction on an s$\pm$ superconductor with different band ratios, α, in (a) the perfect transparency, and (b) the tunneling limit. 117

Chapter 1

Introduction

1.1 History & Background

In 1911, Heike Kamerlingh-Onnes observed an abrupt drop in the resistance of mercury below a critical temperature, T_c, leading to the discovery of superconductivity [1]. Later in 1933, Meissner and Ochsenfeld discovered the second fundamental characteristic of superconductor, i.e., its perfect diamagnetism, which excludes the applied external magnetic field below some critical value, H_c, and later known as Meissner effect [2]. It is modeled by Fritz and Heinz London in 1935 with the London equations based on classical electrodynamicsd [3]:

$$\nabla^2 \mathbf{H} = \frac{1}{\lambda^2}\mathbf{H}$$

This gives an exponential decay of the external magnetic field penetrating into the superconductor, and the characteristic length scale is called the London penetration depth, $\lambda = \sqrt{\frac{mc^2}{4\pi ne^2}}$.

In 1950, Ginzburg and Landau proposed a phenomenological theory to describe superconductivity combining the concept of 2^{nd} order phase transitions with a Schrödinger-like wave function [4]. In 1952, Abrikosov predicted that magnetic flux can penetrate through some superconductors (Type-II) above a critical field, H_{c_1} [5] . In this case, the flux, Φ_m, is quantized so that we have $\Phi_m = n\phi_0$, where $\phi_0 = \frac{hc}{2e} \sim 2 \times 10^{-7} Gcm^2$, and the flux lines are arranged into the "Abrikosov vortex lattice".

In 1956, Leon Cooper disovered that two electrons can bind into a pair

("Cooper pair") in the presence of an attractive potential, no matter how weak it is [6]. Then, in 1957, Bardeen, Cooper and Schrieffer proposed a microscopic theory for superconductivity which was highly successful in explaining different properties of superconductors. This is known as the BCS theory [7]. The BCS theory reproduces the isotope effect discovered independently by E. Maxwell [8]and C. A. Reynolds [9] in 1950, where T_c of superconductors changes accordingly with the change of ion mass, M, in the crystal lattice and satisfies the relation: $T_c \propto \frac{1}{\sqrt{M}} \propto \omega_D$ (ω_D is the Debye frequency, ie., the largest phonon frequency). Bardeen *et al.* proposed that the electron-phonon(e-p) interaction in the lattice plays an essential role in the pairing mechanism of conventional superconductivity. Near the Fermi surface, the e-p interaction gives rise to a weak pairing potential for two electrons and dominates the Coulomb repulsion to produce a net attraction between two electrons. BCS theory also predicts the existence of a superconducting gap, Δ, symmetric about the Fermi surface, within which there are no electronic states. This gap energy is nominally the binding energy of the Cooper pairs. The gap is also explaining different characteristics such as a perfect reflection of photons for $\omega < 2\Delta/\hbar$ at the surface [10], exponential decrease of specific heat [11] and change of London penetration depth with decreasing temperature well below T_c. Ivar Giaever's tunneling experiment into a superconductor in 1960 directly proved the existence of an energy gap, and the corresponding Density of state (DOS) [12]. In 1962, Josephson predicted a new tunneling phenomenon: Instead of the single-particle Giaver tunneling, he predicted Cooper-pair tunneling across a thin insulating barrier weakly coupling two superconductors [13].

In 1986, Alex K. Müller and George Bednorz at IBM Zürich discovered a new system of superconductors, LaBaCuO, with unprecedented $T_c \sim 35$ K,

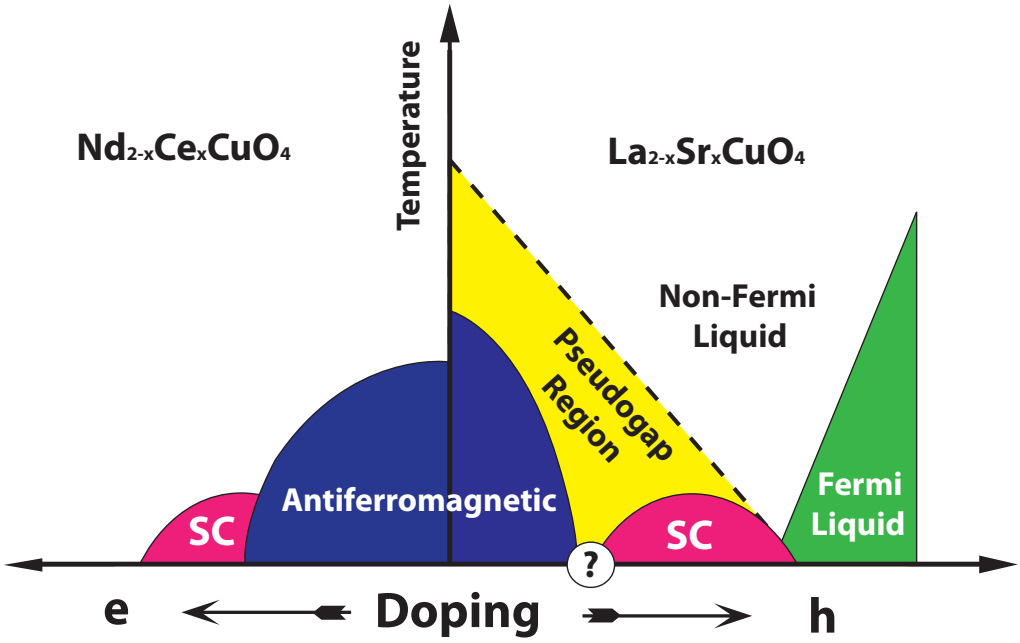

Figure 1.1: Phase diagram of electron-doped and hole-doped cuprate superconductors with antiferromagnetism in the parent compounds. Regions of superconductivity have a dome structure with the maximum T_c at the optimal doping level. Cooper pairs are believed to form without phase coherence inside the pseudogap region.

exceeding the long-believed highest allowed T_c from phonon-mediated BCS theory [14] . Soon after, Wu *et al.* succeeded to boost the T_c well above the liquid nitrogen boiling temperature, to 90 K, in doped $YBa_2Cu_3O_7$(YBCO), which spurred a great enthusiasm in the field due to its promising potential for applications [15]. Up to now, the superconductor $Hg_{12}Tl_3Ba_{30}Ca_{30}Cu_{45}O_{125}$ is discovered to have the highest T_c ~138 K at ambient pressure [16], while its T_c possibly goes up to 164 K under high pressure [17]. All these superconductors constitute a new family known as cuprates because they share a common feature: copper oxide (CuO_2) layers weakly coupled to each other providing a quasi-two-dimensional physical and electronic structure. The parent compounds are surprisingly antiferromagnetic(AFM) Mott insulators and become superconducting only when they are either hole or electron doped. Figure 1.1 shows a generally agreed-upon phase diagram of the cuprate supercon-

ductors as a function of doping. For the hole-doped cuprates, inside the superconducting dome, the order parameter(OP) is a d-wave [18, 19, 20], as shown in Fig.1.2(b). In contrast to the conventional s-wave superconductors (Fig.1.2(a)), the OP phase in a d-wave superconductor has sign changes every $\pi/2$ and there are line nodes where Δ_k=0. In the underdoped regime above the superconducting dome, a pseudogap is observed. The origin of the pseudogap is still under debate, but competing orders clearly play a role [21] and electron pairing without long range phase coherence exists in a region above T_c [22, 23, 24, 25].

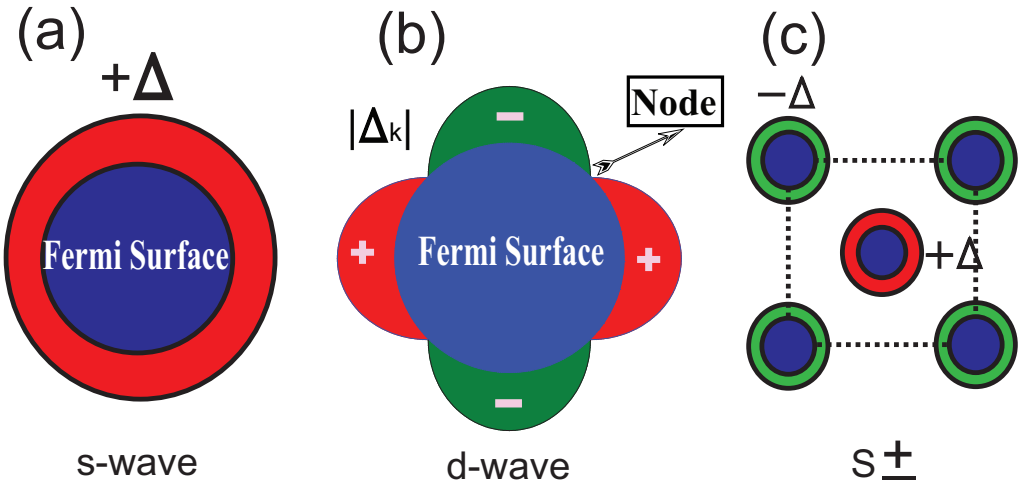

Figure 1.2: The order parameters for (a) s-wave (b) d-wave and (c) extended $s\pm$ superconductors. The $s_\pm$ pairing symmetry will be discussed in chapter 5 for iron-based superconductors.

Heavy-fermion superconductors, such as $CeCu_2Si_2$ [26], UPt_3 [27], $CeCoIn_5$ [28] and UPd_2Al_3 [29], mark another family of unconventional superconductors, first discovered in 1979 by Steglish et al. in $CeCu_2Si_2$. In some of the materials, magnetic order is tuned with chemical doping or applied pressure to zero at a quantum critical point (QCP), where the phase transition is driven by the quantum fluctuations, due to the uncertainty principle, rather than the conventional thermal fluctuations [30, 31]. Around this QCP, super-

conductivity emerges and non-Fermi liquid behavior is observed. This behavior is remarkably similar to the case of cuprates, although the T_c is typically 2 orders of magnitude lower. A surviving mechanism is that Cooper pairs are glued by spin-fluctuations around QCP, causing a d-wave gap symmetry.

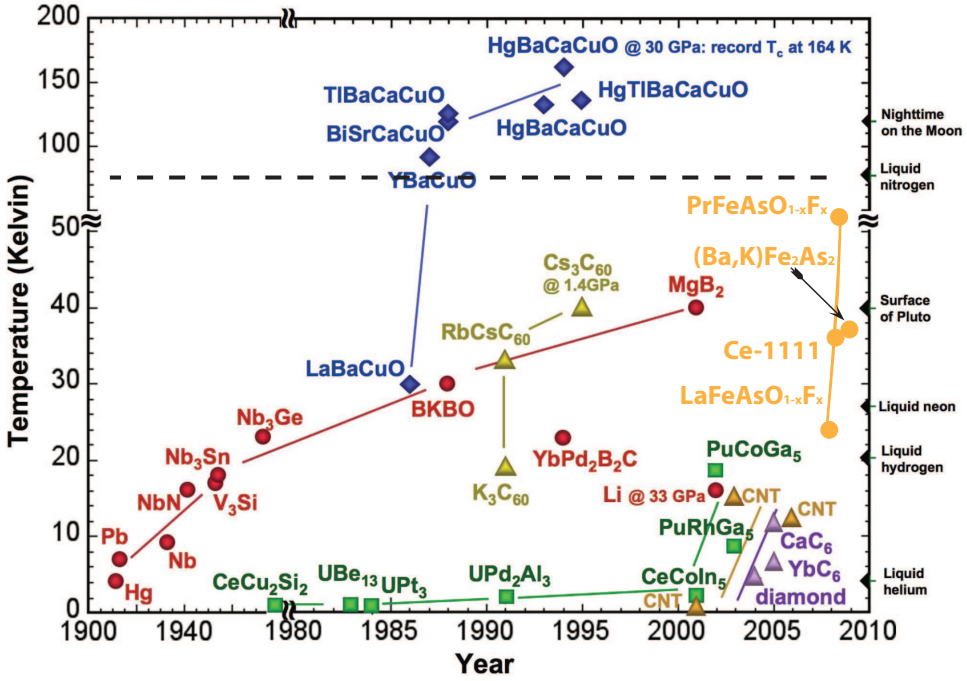

Figure 1.3: Superconducting critical temperatures (T_c) as a function of time in various classes of superconductors. (Adapted from Department of Energy The "Basic Research Needs" Workshop Series: Superconductivity. http://www.er.doe.gov/bes/reports/abstracts.html#SC)

In 2001, MgB_2 was discovered with $T_c \sim 39$ K [32], the first superconductor clearly demonstrating multi-gap features [33, 34, 35, 36]. In 2008, a new family of superconductors based on iron has also made an explosion in the community. Fig. 1.3 shows the superconducting transition temperatures evolving over the past 100 years for various superconductors. Even after extensive investigations, the underlying mechanism of superconductivity in the cuprates and iron-based superconductors remain an open question. Thus, superconductivity is an old but evergreen branch of physics that continues

to bring surprises and joys to people who are exploring this field.

1.2 Microscopic Theory of Superconductivity

This section follows closely the approaches in [37] and [38]. According to the BCS theory, the Hamiltonian of the electron system is described by:

$$H = \sum_{k,\sigma} \varepsilon_k a^+_{k\sigma} a_{k\sigma} + \sum_{k,k'} V_{k'k} a^+_{k'\uparrow} a^+_{-k'\downarrow} a_{-k\downarrow} a_{k\uparrow},$$

where ε_k is the kinetic energy, $V_{kk'}$ the interaction potential, and a^+_k and a_k are the creation and annihilation operator, respectively. The ground state for the system is a macroscopic quantum state of Cooper pairs' condensation, where electrons with equal but opposite momentum are correlated. As shown in Fig. 1.4 (a), for the quasiparticle excitation, its excitation energy E_k, and wave function satisfies:

$$E_k = \sqrt{\varepsilon_k^2 + |\Delta_k|^2}; \qquad \gamma^+_k = u^*_k a^+_{k,\uparrow} + v_k a_{-k,\downarrow} = \begin{pmatrix} u_k \\ \\ v_k \end{pmatrix}$$

where $u_k = \sqrt{\frac{E_k+\varepsilon_k}{2E_k}}; v_k = \sqrt{\frac{E_k-\varepsilon_k}{2E_k}}$. Here, $\Delta_k = -\sum_{k'} V_{kk'} u^*_{k'} v_{k'}$ is the gap equation at T=0 and the minimum excitation energy required at the Fermi surface is the gap energy Δ_k. At finite temperature, the gap equation is:

$$\Delta_k = -\sum_{k'} V_{kk'} \langle u^*_{k'} v_{k'} \rangle = -\sum_{k'} V_{kk'} \tanh\left[\frac{E_{k'}}{2k_B T}\right] \frac{\Delta_{k'}}{2E_{k'}}$$

For an isotropic interaction potential $V_{kk'}$=V_0, the BCS gap is simplified

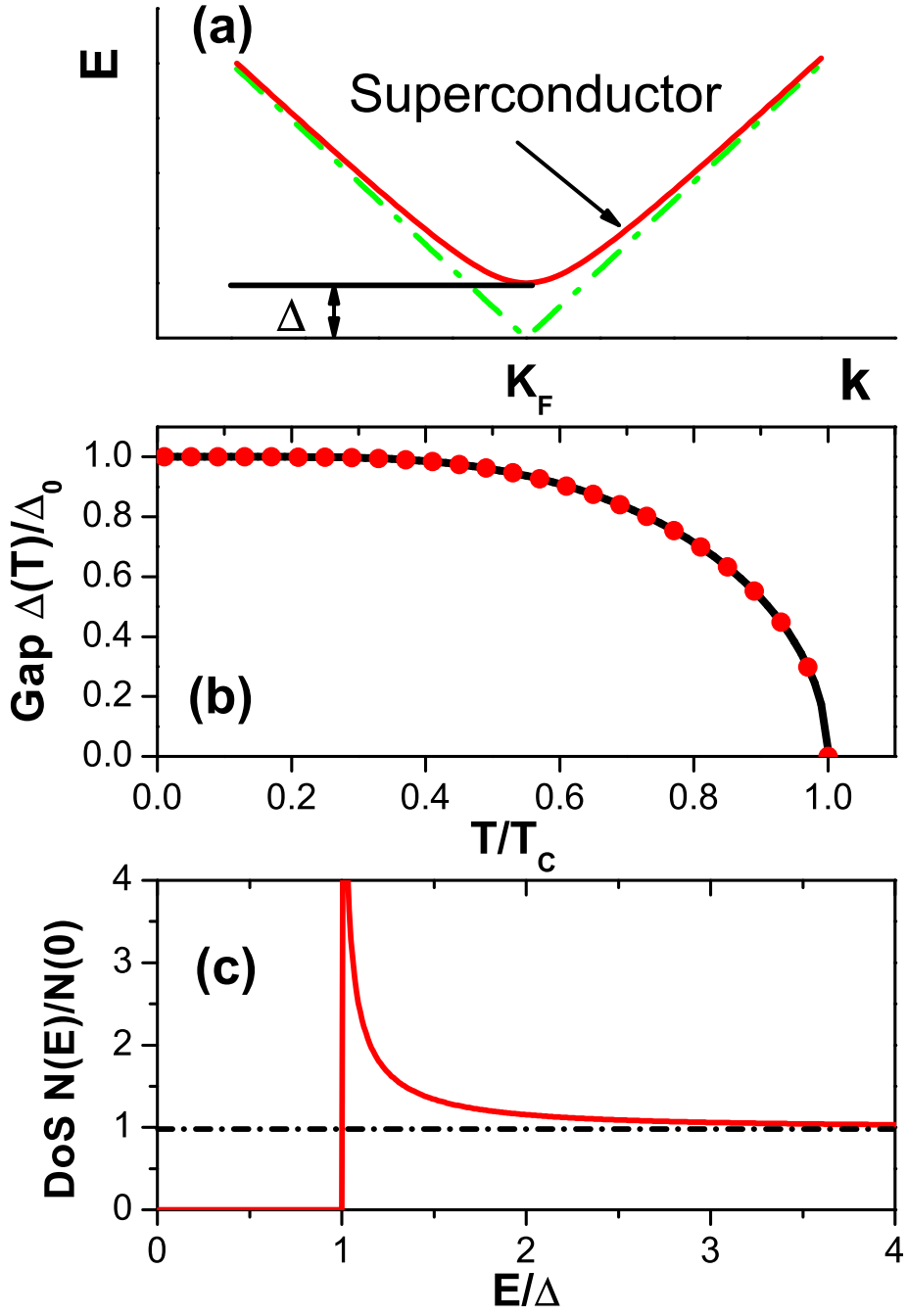

Figure 1.4: (a) Calculated dispersion relations for quasiparticle excitations in the superconducting state; (b) BCS gap as a function of temperatures; (c) Quasiparticle density of states dependent on the energy.

to an isotropic gap, Δ, which satisfies:

$$N(0)V_0 \int_{-\hbar\omega_D}^{\hbar\omega_D} \frac{\tanh\beta\sqrt{\epsilon^2+\Delta^2}}{2\sqrt{\epsilon^2+\Delta^2}} d\epsilon = 1$$

The temperature dependence of the superconducting gap is shown in Fig.1.4 (b). Typically, $N(0)V_0 \ll 1$. In this limit, the gap at T=0, Δ_0, and the critical temperature for the superconductor, T_c, can be approximated:

$$\begin{aligned} \Delta_0 &\simeq 2\hbar\omega_D exp(-\frac{1}{N(0)V_0}) \\ k_B T_c &\simeq 1.14\hbar\omega_D exp(-\frac{1}{N(0)V_0}) \end{aligned}$$

Thus, the crucial ratio in BCS weak coupling theory can be obtained:

$$\frac{2\Delta_0}{k_B T_c} = 3.52$$

This result holds for "weakly-coupled" superconductors within a few percent. Superconductors which exhibit a larger ratio (ex. lead and mercury), are known as strongly-coupled superconductors as discussed later.

Due to the existence of an energy gap, the quasiparticle density of states (DOS) in a superconducting state is modified from the normal state as shown in Fig. 1.4(c):

$$N(E) = \sum_k \delta(E - \sqrt{\varepsilon^2+\Delta^2}) = \begin{cases} 0 & (E < \Delta) \\ N(0)\frac{E}{\sqrt{E^2-\Delta^2}} & (E > \Delta) \end{cases}$$

Thus, quasiparticle excitations inside the gap are prohibited and there is a singular point in the DOS at the gap energy. This modified DOS plays an important role in understanding different thermodynamic property of super-

conductors.

1.3 Transport across the Interface

Several different techniques have been developed to study properties of superconductors through transport measurements across the surface. First, inspired by Esaki's work of electron tunneling in semiconductors [39], Ivar Giaever succeeded to grow a normal metal-insulator-superconductor (NIS) sandwich structure to create planar tunnel junctions. He demonstrated the existence of a superconducting energy gap and directly mapped out the modified DOS [12]. However, it is often difficult to deposit a uniform thin insulating barrier: For example, pinholes leak current and any transport across the junction not arising from single-step elastic tunneling reduces the ability for measurements of spectroscopic properties, and can readily cause junction failure (ie. no measurable tunneling). In 1972, Bogatina and Yanson from the Ukraine called attention to pronounced nonlinearities in the second derivatives of the I-V characteristic in tunnel junctions with pinholes. Yanson then showed that energy resolved spectroscopy could be obtained from metallic contacts with a point-like constriction [40]. From then on, point-contact spectroscopy has emerged as a simple but powerful way to study the electronic structure of superconductors. Meanwhile, with the development of fine mechanical control from circuits, Gerd Binnig and Heinrich Rohrer (IBM Zürich) invented scanning tunneling microscopy (STM) in 1981 [41], where a vacuum gap between the sharp tip and sample is employed as a potential barrier for tunneling. STM has the ability to scan the surface with atomic scale resolutions, which is particularly important in the study of of hight-T_c cuprates, since the gaps are found to be inhomogeneous over a nm lateral

scale. Although an important and powerful technique, STM remains limited in materials (must be in-situ cleavable and bakeable) and magnetic field and temperature dependence measurements remain challenging.

1.3.1 Tunneling

Tunneling, as an example of quantum mechanical phenomena, has proven to be a powerful technique to investigate superconductors. Planar tunnel junctions consist of a sandwich structure, where a nanometer-scale thick insulating layer separates two electrodes. Tunneling current (I), or differential conductance (G) is measured as a function of bias voltage, V, across the junction to obtain I-V, or G-V curves, respectively.

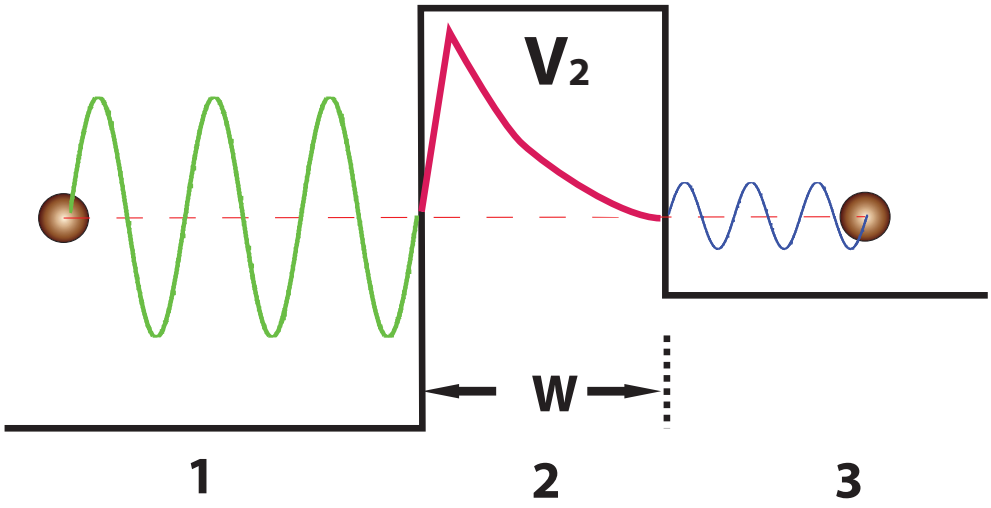

Figure 1.5: A typical quantum tunneling problem: two normal metal electrodes separated by a barrier with insulating potential V_2 and thickness ω.

Considering the simplest case where both electrodes are normal metals and the potential barrier of square shape has a height V_2 as shown in Fig. 1.5, the electron wave function in each region has a general form determined

by the Schrödinger equation:

$$\psi(x) = ae^{ikx} + be^{-ikx}; \quad \hbar^2 k^2/2m = E - V,$$

where V is the potential for the given region. When $E - V > 0$, $\psi(x)$ is a plane wave; while when $E - V < 0$ (classically forbidden region), it is an exponentially-decaying wave and $\psi(x) = ae^{-\kappa x} + be^{\kappa x}$ with $k = i\kappa$. By matching the boundary conditions of the wave functions, the transmission probability, $T = \frac{|\Psi|^2_{Transmission}}{|\Psi|^2_{Incident}}$, can be approximated as follows:

$$|T|^2 = \frac{\hbar k_3 |a_3|^2/m}{\hbar k_1 |a_1|^2/m} = \frac{16 k_1 k_3 \kappa_2^2}{(k_1^2 + \kappa_2^2)(k_3^2 + \kappa_2^2)} e^{-2\kappa_2 W}$$

The probability falls exponentially with the insulating barrier thickness, W, explaining why, experimentally, the insulating layer in the sandwich structure of the junction must be controlled to be a few nm. Employing Fermi's golden rule, the tunneling current from the left electrode to the right one in Fig. 1.6 (a) is:

$$I(V)_{L\to R} = C \int_{-\infty}^{\infty} |T|^2 N_L(E + eV) N_R(E) f(E)[1 - f(E + eV)] dE$$

where N_L, and N_R, is the quasiparticle DOS in the left and right electrode, respectively, and $f(E)$ is the Fermi-Dirac distribution function. Noticing the symmetry for the transmission probability from the right electrode to the left one, similarly, we can get:

$$I(V)_{R\to L} = C \int_{-\infty}^{\infty} |T|^2 N_L(E + eV) N_R(E) f(E + eV)[1 - f(E)] dE$$

Thus, the net current, I(V), across the tunneling junction is:

$$I(V) = C \int_{-\infty}^{\infty} |T|^2 N_L(E + eV) N_R(E)[f(E) - f(E + eV)]dE$$

If $eV \ll E_f$, $N(E) \sim N(E_f)$ and then $I(V) = C|T|^2 N_L(0)N_R(0)V = G_{nn}V$, $G(V) = dI/dV = G_{nn}$, which is simply the Ohm's law. We note that,for normal metals, the density of states $N_N(E) = \frac{1}{\partial E/\partial k} = \frac{m}{\hbar^2 k}$ and this cancels out the term, k, in the transmission probability. Thus, in simple normal metals, the current is not proportional to the quasiparticle DOS and this is known as Harrison's Theorem [42].

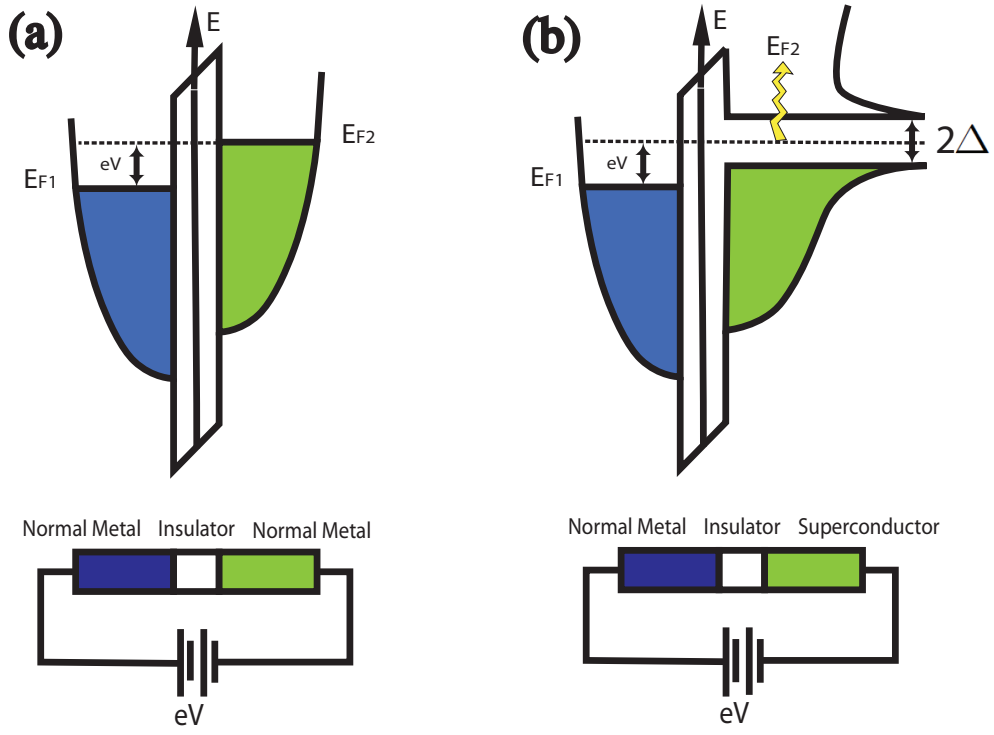

Figure 1.6: Electron band illustration of fabricated junctions biased with voltage V for (a) a NIN sandwich structure; (b) a NIS structure.

This theorem does not hold in the case where at least one electrode of the junctions is superconducting, as shown in Fig. 1.6 (b). For a superconductor,

simple normal-metal quasiparticle DOS relation, $N_N(E) = \frac{1}{\partial E/\partial k}$ is no longer valid because of highly correlated nature of electrons in superconductors. If an energy-independent transmission probability is assumed, the tunneling current for a normal metal/insulating barrier/superconductor (NIS) junction would be:

$$\begin{aligned} I(V) &= C|T|^2 \int_{-\infty}^{\infty} N_L(E+eV) N_R(E)[f(E) - f(E+eV)]dE \\ &= G_{nn} \int_{-\infty}^{\infty} \frac{N_R^S(E)}{N_R^N(0)}[f(E) - f(E+eV)]dE \\ G_{ns}(V) &= G_{nn} \int_{-\infty}^{\infty} \frac{N_R^S(E)}{N_R^N(0)}[-\frac{\partial f(E+eV,T)}{\partial(eV)}]dE \end{aligned}$$

When T=0, $-\frac{\partial f(E+eV,T)}{\partial(eV)} = \delta(E+eV)$, thus $G_{ns}(V) = G_{nn} N_R^S(-eV)/N_R^N \propto N_R^S(-eV)$, which is directly proportional to the quasiparticle DoS. No current will flow across the interface for $|eV| < \Delta$ since there is no DoS available in the superconductor. At the gap edge, there are two pronounced peaks positioned at $\pm\Delta/e$ known as "coherence peaks" arising from the singularity at the energy gap in the DoS. With increasing temperature, the coherence curves are smeared due to fermi function population effects; and the gap energy decrease. So at T_c, the normal-state DoS is recovered.

1.3.2 Andreev Reflection

For the NIS sandwich structure, there would be no current flowing through the junction inside the superconducting gap at low temperatures since quasiparticle excitations below the superconducting gap are forbidden. Thus, if an electron with energy, $E < \Delta$, in the normal metal moves towards the interface and is incident on the insulating barrier, it will be specularly reflected, where the velocity perpendicular to the interface is reversed and other velocity

components parallel to the interface do not change; ie., the interface behaves like a mirror. However, if the normal metal is in direct and clean contact with the superconductor without any scattering at the interface, another scattering process called Andreev reflection will occur for electrons incident at the NS interface with $E < \Delta$. It was proposed by Andeev to explain the anomalous phenomenon of excessive thermal resistance in the intermediate state compared with the Meissner state in 1964 [43].

This section follows closely the steps introduced in [48, 49, 38]. In a superconductor, the quasiparticle wave function for the excitation is a two-column vector, $\psi(x,t) = \begin{pmatrix} f(x,t) \\ g(x,t) \end{pmatrix}$, where f and g is the electron and hole component of the quasiparticle, respectively. They satisfy two coupled differential equations known as Bogoliubov-de Gennes equations:

$$\begin{aligned} i\hbar\frac{\partial f}{\partial t} &= [-\frac{\hbar^2}{2m}\nabla^2 - E_F]f + \Delta(r)g \\ i\hbar\frac{\partial g}{\partial t} &= -[-\frac{\hbar^2}{2m}\nabla^2 - E_F]g + \Delta^*(r)f\,. \end{aligned}$$

Here, we only consider the one-dimensional case with spatially varying $f(x)$ and $g(x)$ and the solution has the form $f = e^{ikx - iE_k t/\hbar}\mu_k, g = e^{ikx - iE_k t/\hbar}\nu_k$, where k is the momentum vector, E_k is energy relative to the Fermi Energy and μ_k and ν_k are functions for the electron and hole components, respectively, and if we set $\varepsilon_k = \frac{\hbar^2 k^2}{2m} - E_F$, the differential equations turn into a matrix equation:

$$\begin{pmatrix} \varepsilon_k & \Delta \\ \Delta^* & -\varepsilon_k \end{pmatrix}\begin{pmatrix} \mu_k \\ \nu_k \end{pmatrix} = E_k \begin{pmatrix} \mu_k \\ \nu_k \end{pmatrix}$$

For a given energy, $E_k > \Delta$, $\varepsilon_k = \pm\sqrt{E_k^2 - \Delta^2}$ and $\hbar|k|^{\pm} = \sqrt{2m(E_F \pm |\varepsilon_k|)}$, where the '+'('-') represents the electron-like (hole-like) quasiparticle excita-

tions with wave function $\psi_e(x) = \begin{pmatrix}\mu_k \\ \nu_k\end{pmatrix} e^{\pm ik^+x}$ and $\psi_h(x) = \begin{pmatrix}\nu_k \\ \mu_k\end{pmatrix} e^{\pm ik^-x}$. μ_k and ν_k are defined as $\mu_k^2 = \frac{1}{2}(1 + \frac{\sqrt{E_k^2 - \Delta^2}}{E_k})$ and $\nu_k^2 = \frac{1}{2}(1 - \frac{\sqrt{E_k^2 - \Delta^2}}{E_k})$.

In the normal metal, there is no pairing potential, $\Delta(r) = 0$, thus, the electron and hole wave functions are decoupled to each other and given by:

$$\psi_e(x) = \begin{pmatrix}1 \\ 0\end{pmatrix} e^{\pm ik^+x}; \qquad \psi_h(x) = \begin{pmatrix}0 \\ 1\end{pmatrix} e^{\pm ik^-x}$$

where $\hbar k^{\pm} = \sqrt{2m(E_F \pm E)}$.

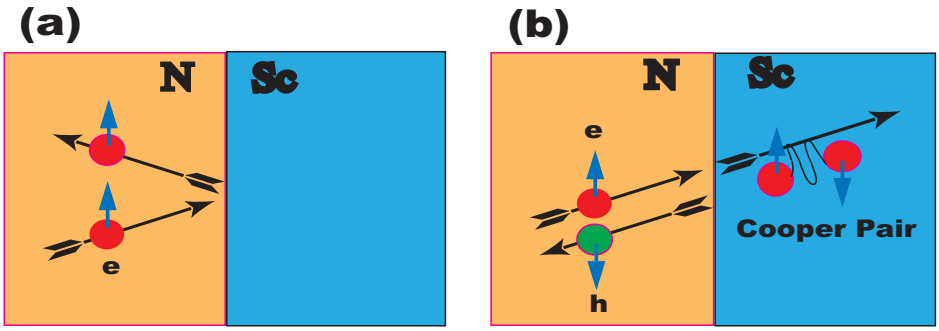

Figure 1.7: For an electron incident at the normal metal and superconductor interface, two types of reflection can occurs: (a) Normal specular reflection; (b) Andreev reflection.

If we consider the charge transportation across a perfect N-S interface in the clean, metallic contact case, an electron incident on the interface from the normal metal with energy E, would be either normally reflected or Andreev-reflected as a hole, as shown in Fig. 1.7 (a) and (b), respectively. It could also go across the interface as an electron-like transmission or hole-like branch-crossing quasiparticle. By matching the group velocity, the wave functions on each side of the interface are:

$$\text{Normal metal: } \Psi_{inc} = \begin{bmatrix}1 \\ 0\end{bmatrix} e^{iq^+x} \; ; \; \Psi_{ref} = a\begin{bmatrix}0 \\ 1\end{bmatrix} e^{iq^-x} + b\begin{bmatrix}1 \\ 0\end{bmatrix} e^{-iq^+x};$$

$$\text{Superconductor: } \Psi_{trans} = c\begin{bmatrix} u_0 \\ v_0 \end{bmatrix} e^{ik^+x} + d\begin{bmatrix} v_0 \\ u_0 \end{bmatrix} e^{-ik^-x},$$

where $A = |a|^2, B = |b|^2, C = |c|^2$ *and* $D = |d|^2$ specify the probability for each corresponding process. If there is no elastic or inelastic scattering across the interface, the wave function on each side will be correlated by the constraint of the continuity condition at the interface:

$$\begin{aligned} \Psi(r)|_{x=0_-} &= \Psi(r)|_{x=0_+}; \\ \frac{d\Psi(r)}{dx}|_{x=0_-} &= \frac{d\Psi(r)}{dx}|_{x=0_+}. \end{aligned}$$

One finds:

$$a = \frac{\nu_k}{\mu_k}; \;\; b = 0; \;\; c = \frac{1}{\mu_k}; \;\; d = 0.$$

For an incident electron with energy, $E < \Delta$, μ_k and ν_k are complex numbers and $\mu_k = \nu_k^*$, and the probabilities are:

$$A = a^*a = 1; \;\; B = 0; \;\; C = \frac{\Delta}{2E_k}; \;\; D = 0.$$

Thus, the incident electron is totally reflected as a hole, with all three group velocity components, spins, charge, and effective mass reversed. The effective charge current for the incident electron and retro-reflected hole in the normal metal is that of two electron charges transmitted across the interface. In the superconductor, the electron-like quasiparticle has a momentum vector $k^+ = \sqrt{k_{Fx}^2 + \frac{2m\sqrt{\Delta^2 - E_k^2}}{\hbar^2}i} \sim k_{Fx} + k_0 i$ and the excitation wave function, $\psi(x) = e^{-k_0 x} e^{ik_{Fx}x} \begin{pmatrix} \mu_k \\ \nu_k \end{pmatrix}$ is an evanescent wave which decays exponentially at the interface. Thus, within the bulk of superconductor (the characteristic length scale is the superconductor coherence length $\xi = \frac{\hbar w_F}{\pi\Delta}$), there is no

quasiparticle current, since $C = D = 0$. The only solution which conserves charge and energy is that in which the two electron charges are bounded as a Cooper pair with a total energy of $2E_F$, and transported as supercurrent. Thus, Andreev reflection is a two-electron process arising from the electron-hole correlations within the superconductor: one incident electron with energy and momentum, $(E_F + E,\ k_F + \delta k)$, bounds with another electron, $(E_F - E,\ -k_F + \delta k)$, in the normal metal to form a single Cooper pair in the superconductor. Effectively, a hole with an opposite spin is retroreflected in the normal metal along the opposite direction of the initial electron trajectory. The wavevector mismatch between the hole and electron, $2\delta k = 2E/\hbar v_F$, cause the electron and hole to lose phase coherence beyond a certain distance.

In the normal metals, the retroreflected holes carry phase information of the macroscopic quantum state in the superconductor. In the calculation above, we assume the pairing potential (order parameter) is fixed, as Δ. If we expand to a more general case, where the order parameter contains a phase factor, $\Delta(r) = \Delta_0 e^{i\Psi}$, the quasiparticle excitation wavefunction becomes $\begin{pmatrix} u_0 \\ v_0 e^{-i\Psi} \end{pmatrix} e^{ik^+x}$ and the retroreflected wave function, $\psi(x) = a = \nu_k e^{-i\Psi}/\mu_k = e^{-i(\Psi+\phi)}$, where $\phi = arccos(E/\Delta)$ is dependent on the incident electron energy. Thus, the phase shift for an incident electron (hole) would be $-\phi - \Psi$ $(-\phi + \Psi)$. It should be noted that the superconducting phase associated with Andreev reflection is the order parameter phase in that particular incident direction (momentum), which has a profound effect in the case of a d-wave superconductor as will be discussed in "Andreev Bound States". Andreev reflection is the microscopic mechanism of the superconductivity proximity effect which gives rise to many interesting phenomena

such as the Josephson effect in SNS structures [44], geometrical bound states in SN structures [45], and Andreev-bound sates at some interfaces of unconventional superconductors [46].

Proximity effect This is the occurrence of superconducting-like behaviors in the normal metal even in the absence of pairing potential, when it is in good electrical contact with a superconductor. A tunnel junction on a N-S bilayers exhibits an effective "gap". This has been well studied as proximity electron tunneling spectroscopy (PETS) in chapter 5 of Ref. [38] and we describe the microscopic origin here.

In order to understand PETS from Andreev reflection, we place the x origin at the N/S interface and consider the boundary condition at the end surface of the metal, $\Psi_N(-d) = 0$, the wave function within N is then:

$$\Psi_N(x) = a\begin{pmatrix}1\\0\end{pmatrix}[e^{-iq^+x} - e^{iq^+(x+2d_N)}] + b\begin{pmatrix}0\\1\end{pmatrix}[e^{-iq^-x} - e^{iq^-(x+2d_N)}]$$

where $q^{\pm} = \sqrt{k_{Fx}^2 \pm \frac{2mE}{\hbar^2}}$ and $\pm$ are for the electron and hole, respectively.

The continuity of Ψ and Ψ' at $x = 0$ leads to the equations for the allowed excitation energies, E_n:

$$\frac{2d_N\Delta}{\hbar\nu_F cos\theta}cos\phi = n\pi + \phi \Rightarrow \frac{2d_N}{\pi\xi_S cos\theta}cos\phi = n\pi + \phi$$

where n=0,1,2..., $cos\phi = E_n/\Delta$, and $\xi_S = \frac{\hbar v_F}{\pi\Delta}$, is the coherence length in the superconductor as discussed earlier.

This equation can be understood in a quasiclassial argument. As shown in Fig. 1.8 (a), an incident electron (1) is retroreflected as a hole(2), which is specularly reflected (3) then Andreev reflected again (4) into an electron.

With each Andreev reflection, thre is a small shift in phase (as discussed before). The phase slip due to each Andreev reflection, and transmission within the normal metal for the hole and electron is: (1) $-\phi(\theta) - \Psi(\theta)$ for the first Andreev reflection along the direction θ; (2) $-2k^{-}d_N$ for the hole to have a around trip in the normal metal; (3) $-\phi(-\theta) + \Psi(-\theta)$ for the second Andreev reflection along the direction $-\theta$; (4) $+2k^{+}d_N$ for the round trip of the electron. In the case of an isotropic superconductor, $\phi(\theta) = \phi(-\theta) = \phi$ and $\Psi(\theta) = \Psi(-\theta) = \Psi$, so the total accumulated phase change for a closed cycle would be: $[2(k^{+} - k^{-})d_N - 2\phi] \sim [\frac{4E}{\hbar v_F cos\theta} d_N - 2\phi] = \frac{4d_N}{\pi\xi_s} cos\phi - 2\phi$. According to the Bohr-Sommerfeld quantization condition of a closed trajectory, the same equation for this surface bound state in the normal metal of a N/S bilayer structure is obtained: $\frac{2d_N}{\pi\xi_S cos\theta} cos\phi = n\pi + \phi$.

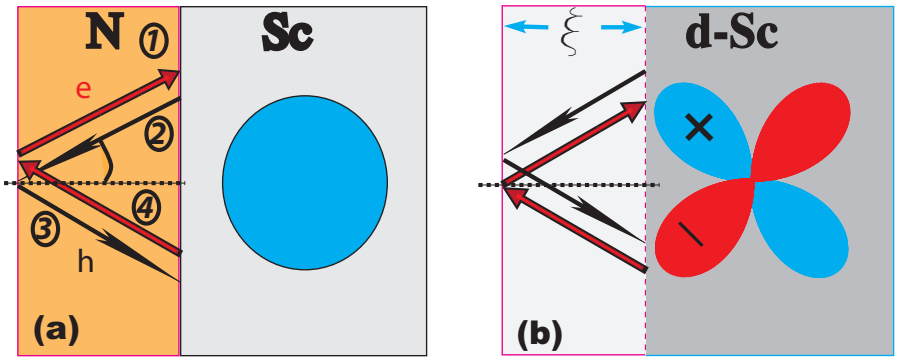

Figure 1.8: Multiple Andreev reflections induce (a) proximity effect with a thin normal metal layer coating on the superconductor; (b) Andreev bound stats at the interface of nodal gap direction for a d-wave superconductor.

For any finite thickness of a normal metal layer on an isotropically-gapped superconductor, there are no zero-energy bound states and an energy gap is induced in the normal metal in proximity to the superconductor. One can also explain this as a superposition of the electron and hole trajectories within the normal metal forming geometrical bound states [45]. When the normal

metal thickness is small compared to the superconductor coherence length, $d_N \ll \xi_S$, the only solution is $\phi \to 0$, and thus $E \to \Delta$. The quasiparticle DoS in the normal metal is therefore the same as in the superconductor. As mentioned above, this is the basis of PETS. This technique which utilizes an N/I/N/S structure instead of a simple N/I/S structure when it is difficult to grow a reliable insulating layer directly on the superconductor surface [47].

When the thickness of the normal metal increases, we have to take the realistic 3-dimensionality into consideration. For a quasiparticle trajectory making an angle, θ, with the normal direction of the interface, the eigen energies of the geometrical bound states will be reduced and finite DoS inside the supercondcuting gap, Δ, would be induced.

Andreev Bound State This occurs when the order parameter of the superconductor exhibits sign chnage around the Fermi surface, for example, a $d_{x^2-y^2}$ symmetry with a form of $\Delta(\theta) = \Delta_0 cos2\theta$, where θ is defined as the angle with a principal axis, x or y. The absolute value of the gap is a maximum along a principal axis but the phase changes sign every $\pi/2$. Then $\theta = \pi/4$ is the nodal direction, where $\Delta = 0$. When the interface is perpendicular to a nodal direction as shown in Fig. 1.8(b), the phase slips for the two Andreev reflection processes are different since $\Psi(\theta) = \pi$ and $\Psi(-\theta) = 0$. The equation for the bound states changes to:

$$\frac{2d_N}{\pi\xi_S \cos\theta} cos\phi = -\pi/2 + n\pi + \phi.$$

For an arbitrary θ and thickness d_N, $\phi = \pi/2$ is always the solution and an eigenstate with $E = 0$ still exists for the limit of $d_N \to 0$ where there is only a d-wave superconductor layer, ie., no normal metal is needed and

these ABS are an intrinsic property on surfaces with nodal direction. This zero-energy surface state is called "Andreev bound state" as a special result of sign reversal in the pairing potential of d-wave superconductors.

1.3.3 BTK Model and Its Extension

If there is a tunneling barrier between the normal metal and superconductor, Andreev reflection is totally reduced and only quasiparticle tunneling process can occur at the interface. For a more general case, Blonder, Tinkham and Klapwijk formulate a model with a δ-function barrier $V = H\delta(x)$ and quantitatively describe the situation for the barrier strength evolving from perfect transparency to a complete opacity at the interface. This is the Blonder-Tinkham-Klapwijk (BTK) model.

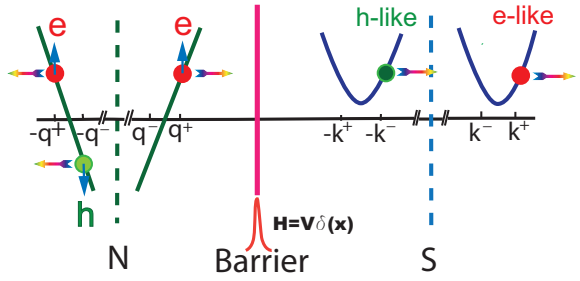

Figure 1.9: Schematic diagram of transport processes across the N/S interface. The closed circles denote electrons, the open circles holes, and the arrows indicate the direction of group velocity.

Figure 1.9 illustrates all the possible processes for an electron incident from the normal metal to a superconductor, either in reflection or transmission, when there is a finite barrier V=H$\delta(x)$ at the interface. As shown in the introduction of Andreev reflection, the wave functions on both sides are assumed. However, the boundary conditions have changed to:

$$\begin{aligned} \Psi(r)|_{x=0_+} &= \Psi(r)|_{x=0_-}; \\ \frac{d\Psi(r)}{dx}|_{x=0_+} - \frac{d\Psi(r)}{dx}|_{x=0_-} &= \frac{2mH}{\hbar^2}\Psi(r)|_{x=0}. \end{aligned}$$

One finds:

$$a = \frac{u_0 v_0}{\gamma}; \;\; b = -\frac{(u_0^2 - v_0^2)(Z^2 + iZ)}{\gamma}; \;\; c = \frac{u_0(1 - iZ)}{\gamma}; \;\; d = \frac{iv_0 Z}{\gamma},$$

where $Z = \frac{mH}{\hbar^2 k_F} = H/\hbar v_F$ and $\gamma = u_0^2 + (u_0^2 - v_0^2)Z^2$.

When a voltage, V, is applied, a non-equilibrium quasiparticle population will be generated. If ballistic acceleration of electrons without scattering is assumed and the distribution functions are assumed to be given by equilibrium Fermi functions with an energy shift only due to the applied voltage potential, the solution is greatly simplified. Consider the current on the N side:

$$\begin{aligned} I &= AJ = 2N(0)ev_F A \int_{-\infty}^{\infty} [f_{\rightarrow}(E) - f_{\leftarrow}(E)]dE; \\ f_{\rightarrow}(E) &= f_0(E - eV); \\ f_{\leftarrow}(E) &= A(E)[1 - f_{\rightarrow}(-E)] + B(E)f_{\rightarrow}(E) + [C(E) + D(E)]f_0(E). \end{aligned}$$

This can be further simplified since $A + B + C + D = 1, A(E) = A(-E)$ and $f_0(-E) = 1 - f_0(E)$:

$$I_{NS} \propto \int_{-\infty}^{\infty} [f_0(E - eV) - f_0(E)][1 + A(E) - B(E)]dE$$

In experiments, inelastic scattering will shorten the quasiparticle lifetime near the N/S interface, which leads to the smearing of conductance coherence peaks. An inelastic scattering term thus should be included in the Bogoliubov equations [50]:

$$i\hbar \frac{\partial F(x,t)}{\partial t} = i\hbar \frac{\partial F(x,t)}{\partial t}|_{field} + i\hbar \frac{\partial F(x,t)}{\partial t}|_{inel}.$$

In the linear approximation, $i\hbar\frac{\partial F(x,t)}{\partial t}|_{inel} = -\frac{i\hbar}{\tau}F(x,t) = -i\Gamma F(x,t)$ and the Bogoliubov coherence factors, μ_0 and ν_0, now satisfy $u_0^2 = \frac{1}{2}\left[1+\sqrt{\frac{(E+i\Gamma)^2-\Delta^2}{(E+i\Gamma)^2}}\right] = 1-v_0^2$. If we define $u_0^2 = \alpha+i\eta$; while $v_0^2 = \beta-i\eta$. Similarly as in the standard BTK model, A(E) and B(E) can be written as:

$$\begin{aligned} A(E) &= \frac{\sqrt{(\alpha^2+\eta^2)(\beta^2+\eta^2)}}{\gamma^2}; \\ B(E) &= Z^2\frac{[(\alpha-\beta)Z-2\eta]^2+[2\eta Z+(\alpha-\beta)]^2}{\gamma^2}; \\ \gamma^2 &= [\alpha+Z^2(\alpha-\beta)]^2+[\eta(2Z^2+1)]^2. \end{aligned}$$

There are three parameters in this BTK model: the superconducting gap, Δ; the interface barrier strength, Z; and the Dynes broadening parameter, Γ (nominally the quasiparticle scattering rate). A good fit to the experimental data is often achieved.

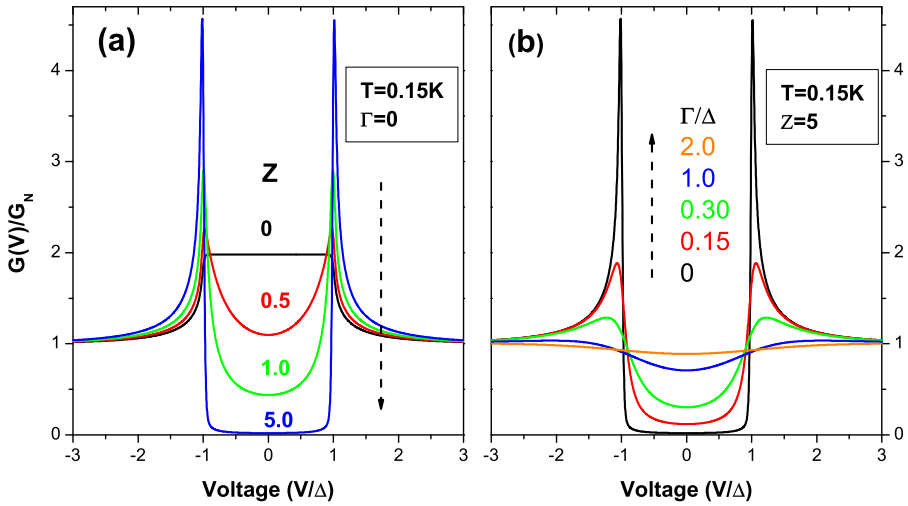

Figure 1.10: Calculated G(V) conductance curves after normalization for a N-S contact as a function of (a) barrier strength parameter Z; (b) quasiparticle smearing parameter Γ

Figure 1.10(a) shows the calculated normalized conductance, G(V), at low temperature with different barrier strengths at the interface. G(V) evolves

into the tunnelling regime discussed in the section 1.3.1 when the parameter Z for the barrier strength increases to about 5. Meanwhile, as the Dynes broadening parameter, Γ, increases, the coherent peaks at the superconducting gap are dramatically smeared as shown in Fig. 1.10(b), where the peak height is reduced while the width is broadened.

The standard BTK model is based on electron transport in one-dimension. In the real situation of 3-dimensional transport across an interface, it is still a good model as long as the superconducting gap is isotropic. However, for the case of d-wave superconductors, the sign change of the OP along different directions exhibits interesting results for the transport across the N/S interface.

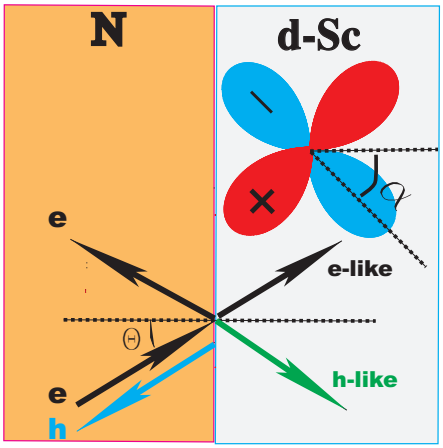

Figure 1.11: Schematic Illustration of reflection and transmission process across the Normal metal and d-wave Superconductor interface. θ and α are the angle of the incident electron and antinodal gap direction with the interface normal, respectively.

If we consider a $d_{x^2-y^2}$ symmetry for the superconductor, let us suppose an electron from the normal metal is incident at the interface with an angle θ. The possible reflection and transmission processes are shown in Fig. 1.11. In the normal metal, it can be either a mirror-reflected electron or a retroreflected hole. For the transmitted quasiparticle, the momentum parallel to the interface and group velocity must be conserved. Thus the electron-like and hole-like quasiparticles will travel in different directions experiencing

different pairing potentials $\Delta(\theta_+)$ and $\Delta(\theta_-)$ in k space, where $\theta_+ = \theta$ and $\theta_- = \pi - \theta$. Applying the boundary conditions as we did for the standard BTK model, the tunneling conductance for the incident electron with angle θ in the superconducting and normal state would be:

$$\begin{aligned} \sigma_S(\theta, E) &= \frac{16(1+|\Gamma_+|^2)cos^4\theta + 4Z^2(1-|\Gamma_+\Gamma_-|^2)cos^2\theta}{|4cos^2\theta + Z^2\{1-\Gamma_+\Gamma_- exp[i(\phi_- - \phi_+)]\}|^2} \\ \sigma_N(\theta, E) &= \frac{4cos^2\theta}{4cos^2\theta + Z^2} \end{aligned}$$

where $\Gamma_\pm = \frac{E}{|\Delta(\theta_\pm)|} - \sqrt{(\frac{E}{|\Delta(\theta_\pm)|})^2 - 1}$ and $exp(i\phi_\pm) = \Delta(\theta_\pm)/|\Delta(\theta_\pm)|$.

The tunneling conductance at energy E then is just the integral of $\sigma_i(\theta, E)$ for all the directions: $\sigma_i(E) = \frac{1}{\pi}\int_{-\pi/2}^{\pi/2} \sigma_i(\theta, E)d\theta \quad (i = S, N)$ and the normalized conductance $\sigma(E) = \sigma_S(E)/\sigma_N(E)$.

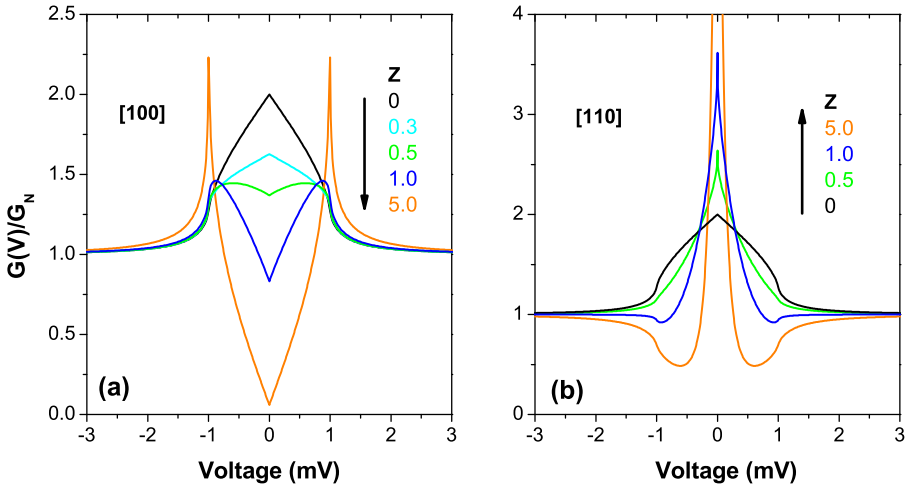

Figure 1.12: Calculated G(V) curves for a contact junction between a normal metal and a d-wave superconductor as a function of the barrier strength Z, with the interface in the (a) gap antinodal direction [100]; (b) gap nodal direction [110].

In the case of a d-wave superconductor, $\Delta(\theta) = \Delta_0 cos[2(\theta - \alpha))]$, where α is the antinodal gap direction. Figure 1.12 (a) and (b) display the calculated differential conductance G(V) as a function of the barrier strength

parameter Z, when the interface normal is along the gap antinodal or nodal direction, respectively. When the interface is perfectly transparent, ie, Z=0, the conductance for these two conditions are the same. However, when the barrier strength Z increases, G(V) in Fig. 1.12(a) develops coherent peaks at $\pm\Delta_0$ and a V-shape conductance dip inside Δ_0, while a strong conductance peak emerges at zero-bias in Fig. 1.12(b) generally referred as zero-bias conductance peak (ZBCP). The underlying physics is the formation of Andreev bound state at the surface of a d-wave superconductor as discussed in subsection 1.3.2.

Chapter 2

Planar Tunneling and Point-contact Andreev Reflection Spectroscopy

Planar tunnelling and point-contact Andreev reflection spectroscopy both play an important role to investigate the gap structure and density of states in superconductors. In practice, each has its own advantages and disadvantages and is complimentary to each other.

2.1 Planar Tunneling

Planar tunneling junctions of NIS (SIS) structure was first applied by Giaever in 1960 [12], where the tunneling barrier was formed by the exposure of evaporated films such as Al and Pb to the atmosphere, which left an insulating oxide layer with typical thickness of 20 Å. The measured I-V curve, or differential conductance curve, $G(V) = dI/dV$, is proved to be directly related to the density of states of quasiparticle excitations in the superconductor, as predicted by the BCS theory. Josephson proposed a different tunneling mechanism where Cooper pair tunneling is present [13]. Giaever and Josephson shared the 1973 Nobel prize for their discoveries. It was later discovered that anomalous behaviors in some superconductors such as Pb and Hg could not been explained by the BCS theory. McMillan and Rowell incorporated the strong-coupling theory of superconductivity into the experiment and applied these phonon-related structures to extract the effective phonon spectrum $\alpha^2F(\omega)$ [51].

2.1.1 Junction Preparation and Measurement

Thin Film Deposition

The preparation of tunnel junctions usually involves thin-film deposition for both electrodes and the insulating barrier. Physical vapor deposition (PVD) and chemical vapor deposition (CVD) are the most widely applied methods to grow thin films. In the PVD system, the bulk or surface of the targeted materials is vaporized and the particles travel a distance to the substrate. A vacuum system is required to allow the vaporized particles to travel as freely as possible. There is no chemical reaction in PVD, while, in CVD, gas-phase precursors react in the chamber and a solid-phase outcome is deposited on the substrate. Different PVD methods are applied in our lab and I would list the most used ones.

Thermal Evaporation A thermal evaporator runs high currents (∼30 A) through a filament to melt ingots and vaporize the desired materials in a high vacuum as shown in Fig. 2.1(a). Good-quality Ag, Au, Pb and other films can be grown in a thermal evaporator.

E-beam Evaporation A high-energy electron beam is directed at a target ingot from an electron gun with a high voltage bias between the electron gun and target. The beam is focused on a single spot on the ingot which causes local heating, resulting in a high local vapor pressure as shown in Fig. 2.1(b). The beam power can be manually controlled to set the evaporation rate in the rage of 1 to 100 Å/s. A low frequency electric field is applied to sweep the beam around a centered position on the ingot to avoid over-heating on one spot with possible melt-through of the ingot and crucible.

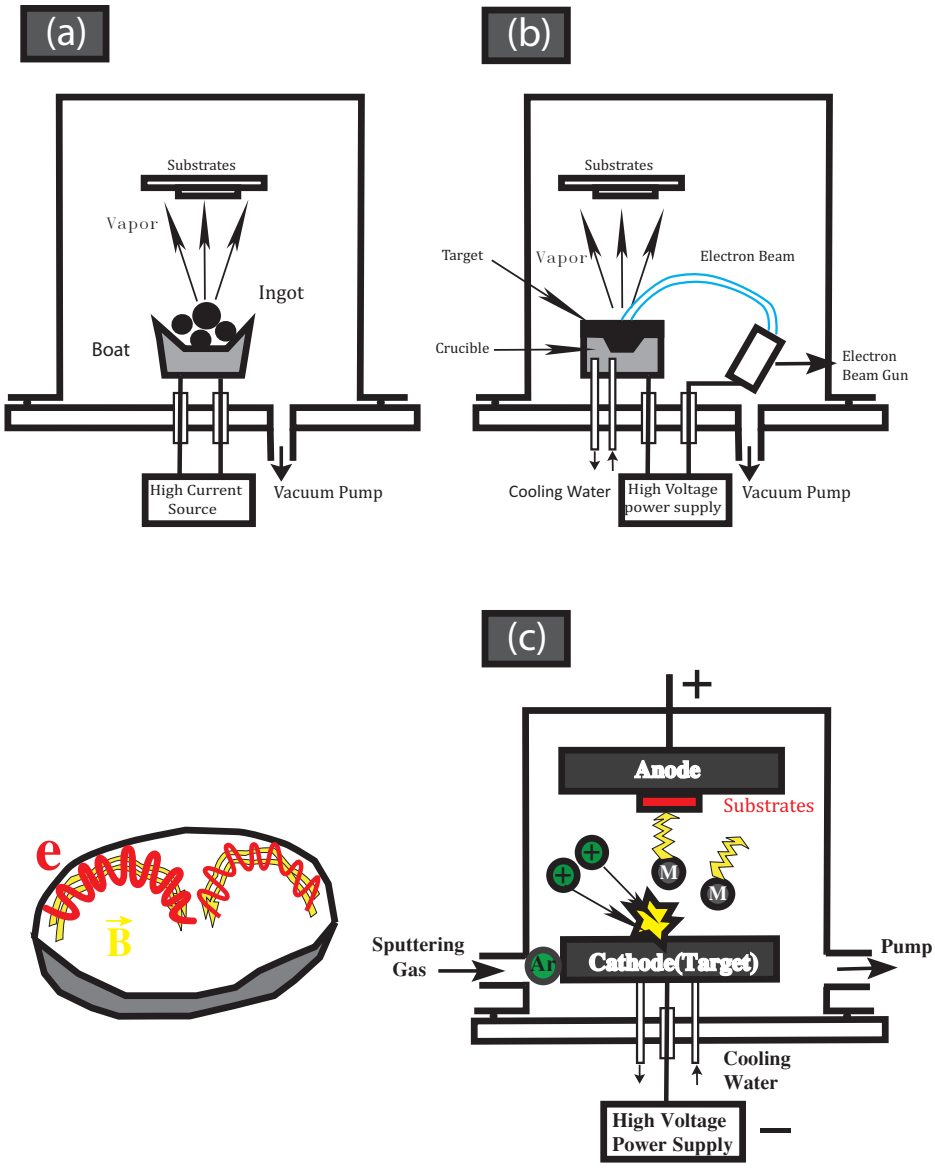

Figure 2.1: Illustration of different PVD thin film growth techniques: (a) Thermal evaporator; (b) Electron-beam evaporator; (c) Magnetron sputtering, the figure on the left shows the electrons confined on the surface of the magnetron due to its magnetic field.

Magnetron sputtering Sputtering is widely used in the semiconductor industry for thin film deposition in the integrated circuit process. The magnetron sputtering systems in our lab (usually referred as System I and II) have been functioning reliably over many years. In both systems, a UHV-compatible stainless steel chamber is pumped to a high vacuum (10^{-8} Torr

- 10^{-7} Torr), and the pressure can be further lowered to 10^{-9} Torr by use of a liquid-Nitrogen cooled Meissner trap inside the vacuum system surrounding the substrates through trapping the water vapor, oxygen and nitrogen molecules on the metal surface. After pump down, inert gas such as Ar is introduced and is constantly flowing through the chamber. A high negative-biased voltage is applied to the target to ionize the Ar atoms and accelerate the ions to the target so that they collide with the target and knock off atomic species from the surface. The sputtered species can fly ballistically or diffusively from the target and impact energetically on the substrate as shown in Fig. 2.1(c). The magnetic field from the magnetron at the back of the target can trap the electrons around the target to undergo more collisions with the neutral Ar atoms and increase the sputtering rate for a given applied voltage.

Insulating Barriers

From the experimental point of view, the tunneling barrier between the electrodes is the most critical step for junction success. It is required to be a good insulator quite thin with a thickness of 15 to 70 Å and pinhole free, and thus difficult to grow and characterize. The best diagnosis for a tunnel barrier is, in fact, a tunneling experiment where the counter electrode is a known and well-characterized superconductor. Thus there is no universal method to guarantee success of tunnel barriers for various conditions. A high dielectric strength is required to be in the tunneling regime and defects such as pinholes in the barriers usually cause current leakage through these weak points. Surface characterization methods are somewhat helpful to analyze the quality of surface barriers and diagnose the potential problems. Some common methods on the formation of insulating layers are introduced here.

Thermal Oxide Barriers The simplest approach to form an insulating barrier was established during the early work of Giaever and others by thermal oxidation of deposited films in the normal atmosphere, even though the oxides have different growing rates for different materials. Giaever reported that Al, Cr, Ni, Mg, Nb, Ta, Sn, and Pb can be relatively easily oxidized with an insulating barrier suitable for the tunneling measurements at the listed order, while Cu, La, Co are "difficult" and Ag, Au and In are rated as "impossible" [52].

An oxide layer with optimal thickness may be achieved by a self-limiting oxidation process, where the growth rate decreases with increasing thickness. This property often results in the desired uniformity of the oxide thickness and eliminates the weak points by faster oxidation. Other factors also affect the rate of thermal oxidation such as humidity, temperature and chemical environment. A remarkable increase of Pb oxidation was reported with increasing humidity of oxygen [53]. Acetic acid vapor was also reported to have a beneficial effect on the air oxidation of In.

Oxidized Metal Overlayers Since not all the metals can be easily oxidized to form a suitable tunneling barrier, an alternative way is to sputter a thin layer of Al (20-70 Å) on the superconducting film, eg. Nb, with subsequent oxidation of the Al overlayer [47]. It has been demonstrated by tunneling measurement that Al can uniformly coat the surface of Nb base film without pinholes in the oxide layer. In the case of a thicker Al film, metallic Al may be left by incomplete oxidation, but this may not cause a problem in conventional superconductors with large coherence lengthes as discussed earlier in the proximity effect and related tunneling methods. This technique has been widely applied to the fabrication of Josephson junction

array and SQUID [54, 55].

Directly Deposited Artificial Barriers Artificial barriers can also be directly deposited to behave as the insulating layer due to their band gap. Amorphous silicon [57], Ge [58], AlN [59] and Al_2O_3 [60] have been applied for the junction fabrication. However, it is crucial to control the insulating barrier thickness $\sim$ 20 Å .

Tunnel Junction Preparation

After the base electrode thin film and tunnel barrier is formed on the substrate, a thin layer of an insulating polymer (Duco cement thinned with acetone) is painted on a portion of the top surface to define a narrow exposed region as shown in Fig. 2.2.The counterelectrodes are then deposited through a stainless steel mask with patterned shapes and fixed dimensions. The junction area, A, is defined by the contact region between the two electrodes through the tunnel barrier($A = l \times d$).The relationship between the junction conductance G, and junction area A, $R_J \times A$ =constant, is a good criterion to check the junction uniformity.

Junction Measurement

The junctions are connected to the measurement setup in a standard four-probe configuration. Since the differential conductance is more accurate to characterize the junction quality and study the superconducting properties, an ac modulation method is applied to measure derivatives of the I-V characteristic. The basic principle is to add a small ac voltage δv (current δi) with frequency ω at a finite dc voltage V_0 (current I_0). The current, I, can

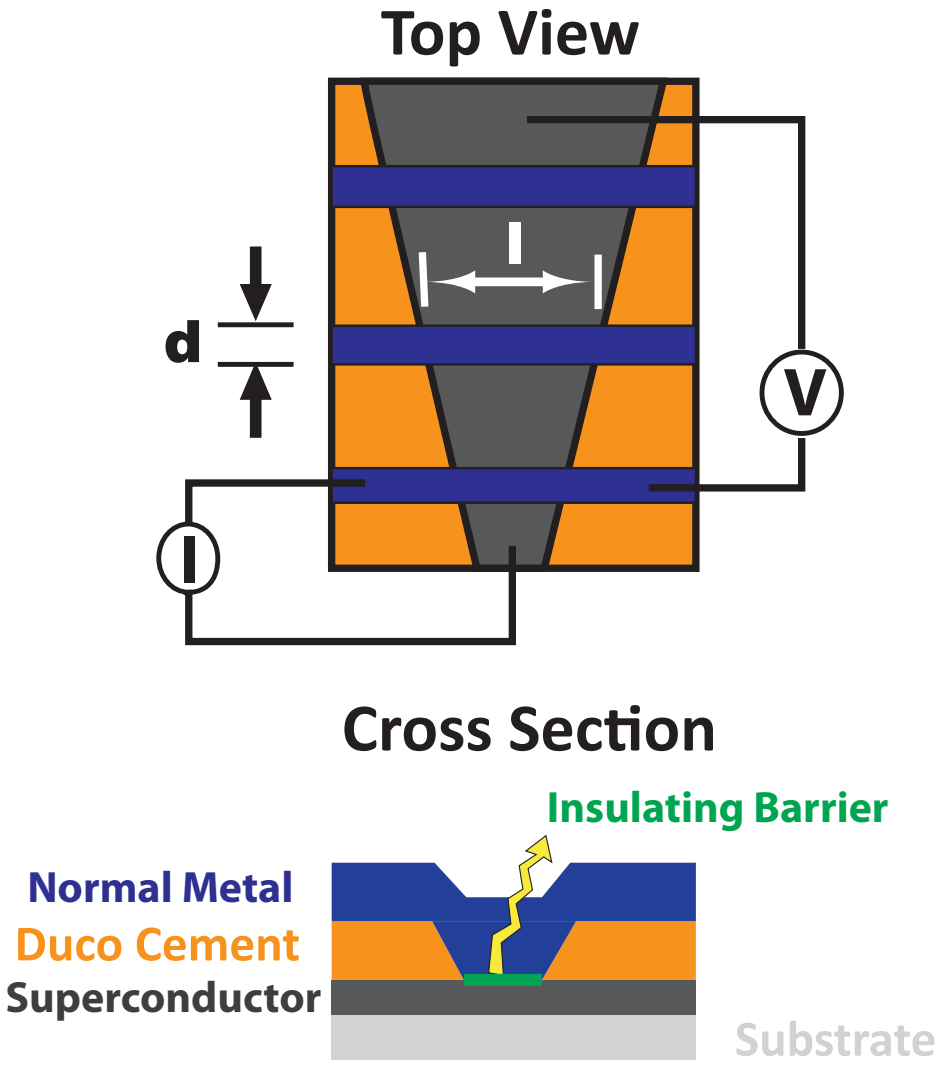

Figure 2.2: Illustration of the tunnel junction fabrication viewed from the top and cross-section, respectively. In this case, the black thin film is the superconducting electrode and the blue strips are the normal metal counter-electrode, while the orange strips are the painted duco-cement.

be expansed as Taylor expansion:

$$\begin{aligned} I(V_0 + \delta v cos\omega t) &= I(V_0) + \frac{dI}{dV}|_{V_0}\delta v cos\omega t + \frac{d^2I}{2dV^2}|_{V_0} i^2 cos^2(\omega t) \\ &= I(V_0) + \frac{dI}{dV}|_{V_0}\delta v cos\omega t + \frac{d^2I}{4dV^2}|_{V_0} i^2[1 + cos(2\omega t)] \end{aligned}$$

To the first order approximation, an ac current signal measured at the frequency ω is proportional to the first derivative of dI/dV, whereas a signal with frequency 2ω is proportional to the second derivative d^2I/dV^2. Detection of the ac signal at a particular frequency is achieved by phase sensitive lock-in amplifiers. The fundamental frequency, ω, chosen here is usually fixed at 633 Hz. The diagram of the electronic circuit used in our lab is shown in Fig. 2.3.

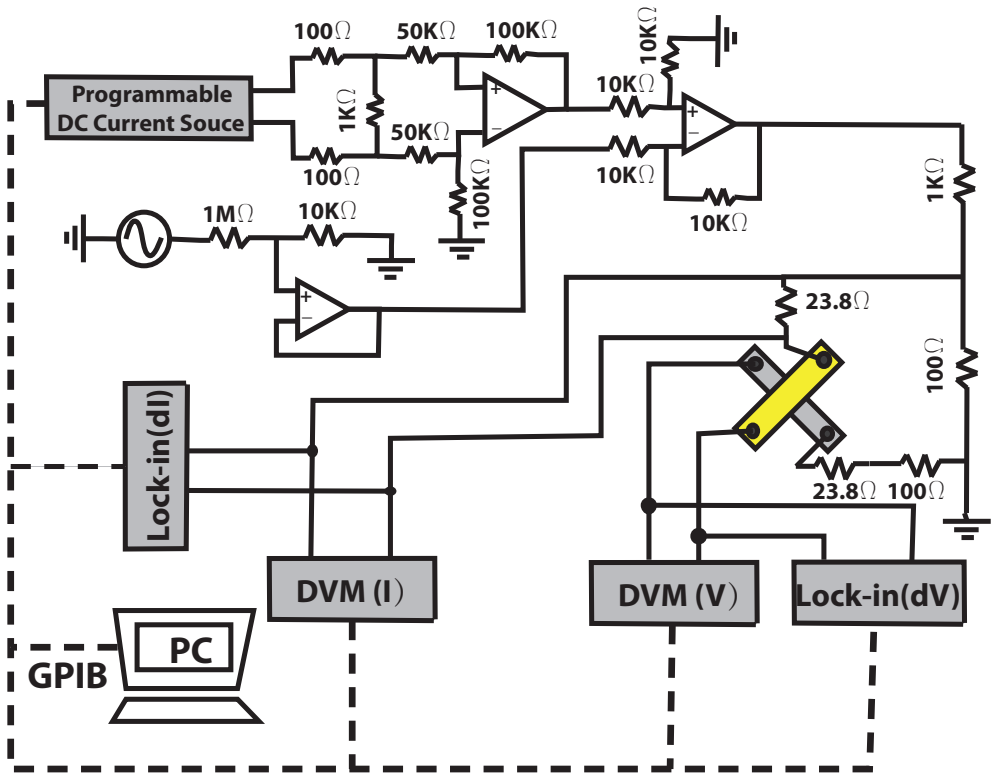

Figure 2.3: Schematic electronic circuit for the differential conductance measurement. The ac voltage signal is provided by a function generator in the lock-in amplifier. All resistors and operational amplifiers are assembled in a box. This work is done by R. Murphy [61].

It should be noted that the ac voltage magnitude applied to the circuit is also important since it affects the energy resolution of the measurement. It has been proven that the ac voltage behaves as an activation of quasiparticles

in the superconductor, which has the same effect as the temperature, T, causing thermal population effects and broadening narrow spectral features. The resulting resolution for tunneling spectroscopy is given by Duif [62]:

$$\delta = [(3.53k_BT/e)^2 + (1.73\sqrt{2}V_1)]^{1/2}$$

Thus it is important to keep the ac modulating voltage small enough as not to cause significant smearing of the spectra at finite temperatures. However, it must also be large enough to provide a reasonable signal-noise ratio.

2.1.2 NIS and SIS Junction

NIS junction: Al-AlO$_x$-Pb A 1000 Å thick Al thin film is deposited on a clean sapphire substrate with the E-beam evaporator in the microfabrication lab. After exposure in the air for ∼10 minutes, it is painted with the duco cement mixture to define the junction areas. It is then placed in the thermal evaporator to grow ∼ 1000 Å Pb as the superconducting counterelectrodes through a stainless steel patterned mask. These junctions are then connected to the measurement circuit through a general-purpose probe and cooled to 4.2 K in the liquid helium dewar. 1.5 K can be achieved by pumping the dewar when there is not too much but sufficient liquid helium (∼ 2 Liter) inside the dewar. We usually control the ac modulation voltage $\delta V \sim 100$ uV $\ll \frac{3.53k_BT/e}{1.73\sqrt{2}} \sim 525$ uV so that the effective temperature for the junction is almost the same as the environmental temperature.

Figure 2.4(a) and (b) show the current, I(V), and differential conductance, G(V), for the Al-AlO$_x$-Pb tunneling junction at T=1.4 K. The data are analyzed by the tunneling model where $DoS(E) \propto Re[\frac{E+i\Gamma}{\sqrt{(E+i\Gamma)^2-\Delta^2}}]$. At T= 1.4 K, the simulated gap value, Δ=1.4 meV, and $\frac{2\Delta_0}{k_BT_c}$ ∼4.5, deviates from

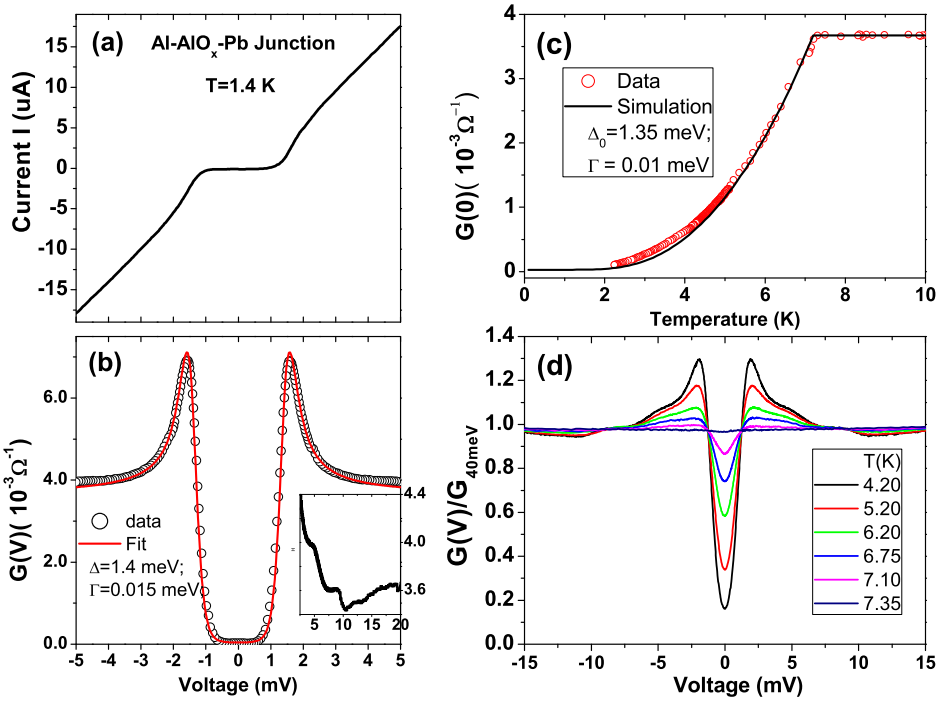

Figure 2.4: Al-AlO$_x$-Pb tunnel junction measurement: (a) the tunneling current, I, and (b) differential conductance, G, as a function of the bias voltage, V, at T$\sim$ 1.4 K. In (b), the experimental data(black dot) and the tunneling simulation (red line) fit well. The inset of (b) show the fine structure of G(V) due to phonons in Pb; (c) Zero-bias conductance G(0)(red dot) and the fit(black line) as a function of temperature; (d) the normalized temperature dependent G(V) curves from 4.2 K to 7.35 K.

the BCS weak-coupling limit ratio of 3.52. In the strong-coupling limit, fine structures in the DoS and thus the tunneling G(V) curves due to electron-phonon coupling may be observed as shown in the inset of Fig. 2.4(b). This will be discussed later in detail.

NIS Junction: Nb(Al)-AlO$_x$-Ag Nb is known to be easily oxidized into several oxides in air, however, some of them are conducting, so do not make a good insulating tunnel barriers. It has been proven that 20-100 Å Al thin layer can coat the Nb film uniformly and form a good tunneling insulating barrier in the air [56]. After 1500 Å Nb film has been deposited in System

I at 450 ^{o}C, the substrate is cooled down to room temperature and a 70 Å Al layer is deposited onto the Nb film. The bilayer film is left in air for 20 minutes or more and painted with the duco cement mixture to define the junction areas. The film is placed back in the thermal evaporator and a $\sim$ 1000 Å thick silver counterelectrode is deposited through a patterned mask.

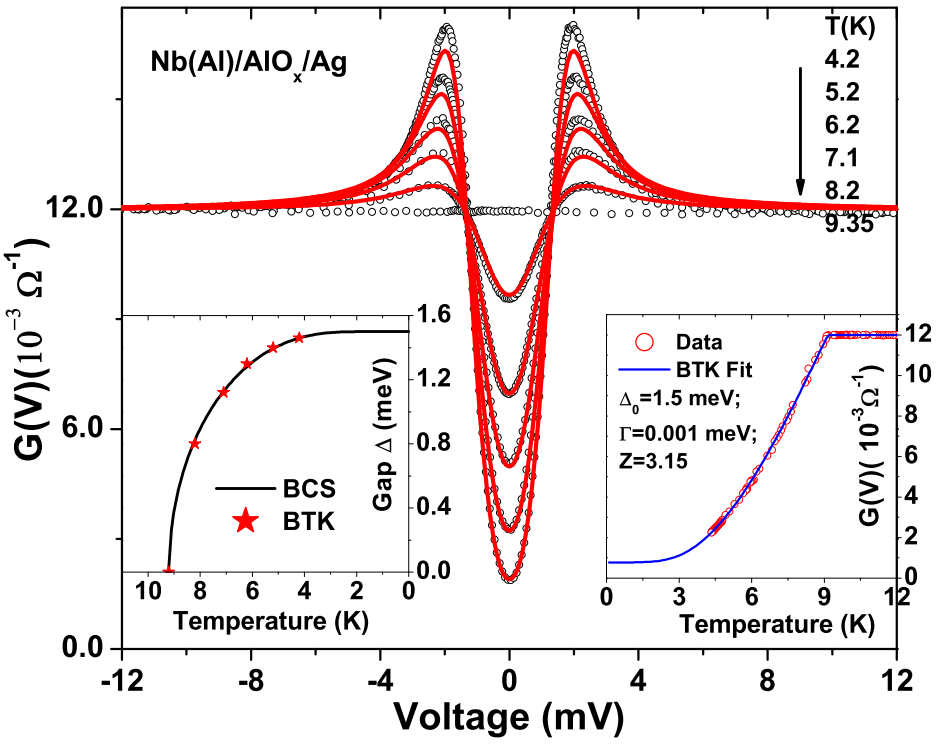

Figure 2.5: Temperature dependent G(v) curves for the experimental data of a Nb(Al)-AlO$_x$-Ag tunnel junction (black dots) and BTK simulations (red line). The left inset shows the temperature dependence of the simulated superconducting gap (red star) in comparison with the BCS-like gap curve(black lines). The right inset shows the temperature dependence of zero-bias conductance, G(0), for the junction (red dots), which shows a kink point at the Nb superconducting critical temperature 9.2 K. The simulating curve based on the BTK model (blue lines) fits the experimental data quite well with a Z=3.15.

The temperature dependent differential conductance curves, G(V), are shown in Fig. 2.5 and G(V) curve is flat above T_c $\sim$9.2 K. It is found the tunneling model would usually overestimate the dip inside the gap and a

general BTK fit gives Z∼3.2, indicating a large barrier strength but not yet in the tunneling limit, which is probably due to the incomplete oxidation of Al, ie., AlO_x, as the insulating barrier of the junction. Meanwhile, the coherent peaks of the BTK fits around the gap energy are not as high as the the experimental data in amplitude, even though the smearing parameter, Γ, is set close to zero. The origin of this discrepancy is not known. The simulated superconducting gap size follows the general BCS-like temperature curve with Δ_0 ∼1.5 meV as shown in the left inset. The right inset is the zero-bias conductance curve as a function of temperature, which confirms T_c ∼9.2 K from the kink in the curve and can be fit quite well with the BTK model.

SIS' junction: Nb(Al)-AlO_x-Pb If Ag is replaced by a 1500 Å thick superconducting Pb, a SIS' tunneling junction can be grown. Fig. 2.6 (a) and (b) show the tunneling current, I, and differential conductance, G, as a function of the bias voltage at 3.75 K. The temperature dependent G(V) curves for T< 7.3 K and 7.3 K <T≤ 9.4 K are shown in Fig. 2.6 (c) and (d), respectively.

Compared with the NIS junction, SIS' junction here has a much sharper feature for both I(V) and G(V) curves as shown in fig. 2.6: The I(V) curves obtained with the tunneling circuit and directly biased by a current source show no tunneling current flowing through the junction below $|V| \lesssim 2.8$ meV $(\Delta^{Nb}+\Delta^{Pb})$. There is a small discrepancy between them and the origin is not known. The G(V) curve at T=3.75 K has very sharp peaks around 2.8 meV with the maximum amplitude of 8 times of the normal state conductance. Only one small peak appears at V=0 for G(V) as shown in fig. 2.6(b) because the gap sizes in Pb and Nb are comparable at 3.75 K. However, due to the

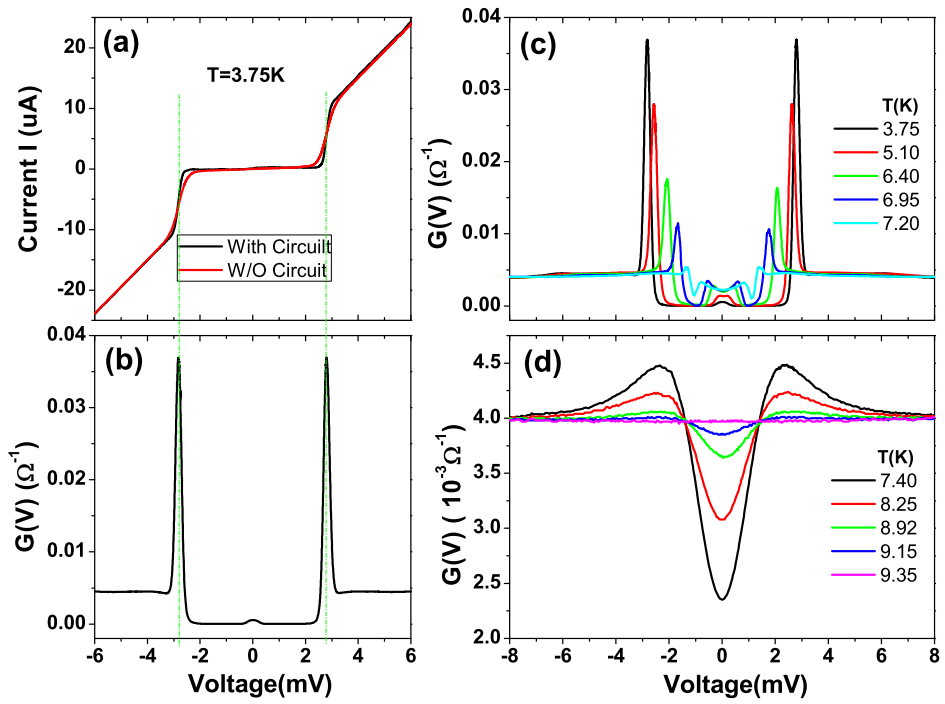

Figure 2.6: Nb(Al)-AlO_x-Pb tunneling junction: (a) tunneling current vs bias voltage curves for the setup of current bias (red) and voltage bias (Black) at T=3.75 K; (b) G(V) curve at T=3.75 K; (c) Temperature dependent G(V) curves below Pb superconducting critical temperature 7.4 K; (d) Temperature dependent G(V) curves above 7.4 K.

different temperature evolutions of the superconducting gaps in Nb and Pb, the peak splits into two at $\pm(\Delta^{Nb} - \Delta^{Pb})$ in Fig.2.6(c). For Fig.2.6(d), Pb is not superconducting anymore above T_c ~7.2 K and the SIS' junction behaves the same as NIS junction of Nb(Al)-AlO_x-Ag.

2.1.3 2^{nd} Harmonics and Phonon Structure

As mentioned in the section of Al-AlO_x-Pb junction, there is some subtle structure in the G(V) curve and experimental data deviate from the BCS prediction of DoS in the weak coupling limit. The analyzed gap size $\Delta_0 \sim 1.4$ meV, $2\Delta/k_BT_C \sim 4.5$, is much larger than the BCS ratio 3.52. Thus Pb is

a simple model of strong-coupling superconductor. Tunneling as a powerful tool to quantitatively investigate the strong-coupling superconductivity of Pb is first demonstrated by McMillan and Rowell to study the phonon spectra as a glue of "Cooper pair" [51]. The structure below in this section follows that of chapter 4 in Ref. [38].

In contrast to the instantaneous response in the BCS interaction, a more realistic theory will involve the local and retarded features of this pairing interaction. The electron-electron coupling mediated by phonons is given by Eliashberg [63]:

$$V_{k,k+q} \propto \frac{E_{k+q} + \hbar\omega_q}{(E_{k+q} + \hbar\omega_q)^2 - E_k^2}$$

The superconducting pairing potential, Δ, would then generally be dependent on the electron momentum and energy, ie. $\Delta = \Delta(\vec{k}, \omega)$. If the weak k dependence of Δ is neglected, Scalapino, Shrieffer, and Wilkins proposed the gap equations for phonon-mediated superconductors [64].

$$\begin{aligned}
[1 - Z(\omega)]\omega &= \int_0^\infty d\omega' Re\left[\frac{|\omega'|}{[\omega'^2 - \Delta^2(\omega)]^{1/2}}\right] \\
&\quad \times \int_0^\infty d\Omega \alpha^2(\Omega) F(\Omega)[D_\Omega(\omega' + \omega) - D_\Omega(\omega' - \omega)] \\
\Delta(\omega) &= \frac{1}{Z(\omega)} \int_0^{\omega_c} d\omega' Re\left[\frac{\Delta(\omega')}{[\omega'^2 - \Delta^2(\omega)]^{1/2}}\right] \\
&\quad \times \int_0^\infty d\Omega \alpha^2(\Omega) F(\Omega) \left[D_\Omega(\omega' + \omega) + D_\Omega(\omega' - \omega) - \mu^*\right],
\end{aligned}$$

where $D_\Omega(\omega) = \frac{1}{\omega + \Omega + i\delta}$, $F(\omega)$ is the phonon density of states and $\alpha^2(\omega)$ is an effective electron-phonon coupling function for a phonon at frequency ω. $\alpha^2(\omega)F(\omega)$ satisfies:

$$\alpha^2(\omega)F(\omega) = \frac{\int \frac{dS_{k'}}{|\vec{v}_{k'}|} \int \frac{dS_k}{|\vec{v}_k|} \frac{1}{(2\pi)^3\hbar} \sum_\lambda |g_{k',k,\lambda}|^2 \delta[\omega - \omega_{k'-k,\lambda}]}{\int \frac{dS_k}{\vec{v}_k}}$$

The renormalization function $Z(\omega)$, and pairing potential $\Delta(\omega)$, are determined by the $\alpha^2F(\omega)$ function in superconductors, but not linearly, which can be solved from first-principle calculations.

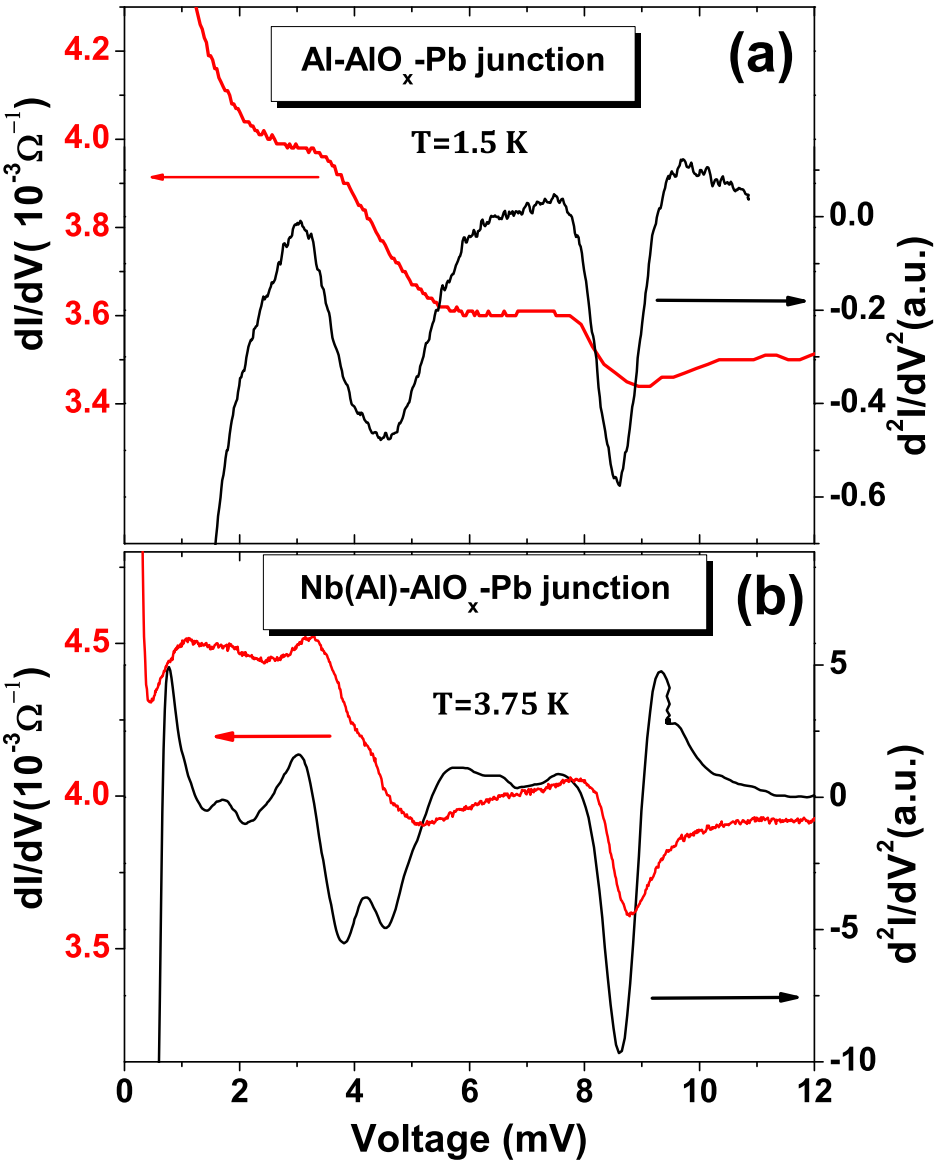

Figure 2.7: The first (red) and second (black) derivatives of the tunneling current I, respectively, to indicate the phonon spectra in Pb. The voltage in (a) is shifted by V-Δ_0^{Pb} (1.3 meV) for the Al-AlO$_x$-Pb junction at T=1.5 K; and (b) V-$\Delta_0^{Pb} - \Delta_0^{Nb}$ (1.5 meV) for the Nb(Al)-AlO$_x$-Pb junction at T=3.5 K.

A practical way to check the validity of Eliashberg theory is demonstrated

by McMillan and Rowell through planar tunnel experiment on Pb-I-Pb junctions, since tunneling is a direct measurement of quasiparticle DoS $N(\omega)$, where $N(\omega)$ is given by:

$$N(\omega) = Re\left[\frac{|\omega|}{[\omega^2 - \Delta^2(\omega)]^{1/2}}\right].$$

This is similar to the case of weak coupling superconductor, but with Δ being energy dependent. The Eliashberg function, $\alpha^2F(\omega)$, is determined by inversion back through a iterative loop until it converges. A direct method to find out phonon features can be made using a 2nd harmonic measurement of the tunneling current d^2I/dV^2: As a function of bias voltage V, the peak position of $\alpha^2F(\omega)$ corresponds to the point where the slope in the conductance is most negative, thus, a negative peak in dI^2/dV^2 data and the phonon energy is located around $V - \Delta_0$ (NIS junction) or $V - \Delta_0 - \Delta_0'$ (SIS' junction).

As stated before, the 2nd harmonic signal of the primary modulation frequency, ω, corresponds to the second derivative of current, where $\frac{d^2I}{dV^2} \propto \frac{\delta I_2}{(\delta V)^2}$. In our circuit, we measure the 2nd harmonic of the ac voltage signal δV_2 and first harmonic of ac current δI. The measured $\frac{d^2V}{dI^2} \propto \frac{\delta V_2}{(\delta I)^2}$ can be converted to $\frac{d^2I}{dV^2}$ through the relationship $\frac{d^2I}{dV^2} = -\frac{1}{(R_d)^3}\frac{d^2V}{dI^2}$. If the differential resistance R_d does not change too much in the interested range, we can take $\frac{d^2I}{dV^2} = -\frac{d^2V}{dI^2}$ for approximation and address the basic features of the Eliashberg function.

Figure 2.7 (a) shows the first derivative $\frac{dI}{dV}$ (red), and second derivative $\frac{d^2I}{dV^2}$ (black) as a function of V-Δ_0, respectively, of the tunneling current in the Al-AlO_x-Pb junction at T=1.5 K. The data for the Nb(Al)-AlO_x-Pb junction at T=3.75 K are shown in Fig. 2.7 (b) as a function of $V - \Delta_0^{Nb} - \Delta_0^{Pb}$. Although the temperature for SIS' junction is higher than that for NIS

junction, the second harmonic spectra for SIS' has more detailed structure, especially two peaks in the voltage range 3-5 meV are clearly present. This is due to the sharper feature of coherent peaks in SIS' junction, while in the NIS junction, the coherent peaks are quite broad to dim the fine structure near that region. The phonon peaks at 3-5 meV and 9 meV region are consistent with the work in [51].

2.2 Point-contact Andreev Reflection Spectroscopy (PCARS)

As an alternative technique we use to probe the gap structure is point-contact Andreev reflection spectroscopy (PCARS), which has been a major focus of my graduate work due to its advantages over planar tunneling particularly in the study of bulk materials. Single crystal or polycrystalline bulk samples are not good candidate for planar tunneling. Even for superconducting thin films, it is sometimes difficult to grow the artificial sandwich structure, especially the thin tunneling barrier. In contrast, it is easy in PCARS to form point-contact junctions on almost anything by engaging a sharp nanoscale Au tip on the surface.

2.2.1 Configurations for PCARS

Different methods of point-contacts have been developed and proved to work over the years: Thin film or lithographic techniques, which are quite similar to the planar tunneling structures but with appearance of "pinholes" to leak the current as metallic shorts was the first PCARS junction [40]. These defects or weak spots in the dielectric layer can be formed by mechanically

damaging the oxide film or the electric shorts may form from the oxide not wetting the underlying film. A single hole can also be patterned quite precisely using nanolithography and reactive ion etching to form a nanobridge. Despite the advantage of this technique with its high tolerance to thermocycling and mechanical vibrations, such nanobridges are difficult to make and can not be formed on all interfaces(materials limitations). Needle-anvil method and its variants, such as shear method or break junctions, is another PCARS method. One can form a small contact constriction between electrodes as shown in Fig. 2.8(a) and control the contact size and resistance through a precision mechanical mechanism. This method is widely applied to investigate superconducting bulk samples due to its simplicity. However, a drawback compared to the lithographic method just described is its reduced stability to vibrations and temperature variations.

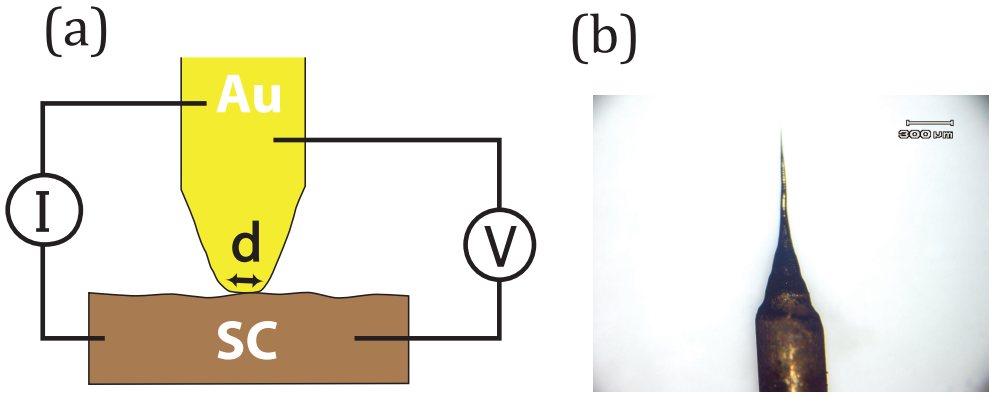

Figure 2.8: (a) Schematic illustration of the needle-anvil type point-contact setup; (b) the optical microscopic image of a Au tip prepared by the electrochemical etching method in courtesy of J. A. Garmilla.

Tip Preparation

Figure 2.8(b) shows the sharp tip specially prepared by electrochemical etch. Compared with simple mechanical cutting with razor blade, this method is

proved to be far more controllable and reproducible.

The procedures for electrochemically etching sharp Au tips have been well established for PCS or STM purposes [65, 66]. A gold tip of $500\,um$ diameter and $\sim 9\,mm$ length is immersed into undiluted hydrochloric acid with a platinum counter-electrode. Etching is achieved by applying 10 V pulses to the gold wire with a frequency of $\sim 10.30\,kHz$ and a sweep time of $5\,\mu s$, at a bath temperature of $50°C$. Thin, uniform, and clean gold tips are reproducibly obtained.

PCARS Probe

Two PCS probes available in our lab are both the "Needle-anvil" type: (1) The Cantilever-Andreev-Tunneling (CAT) rig [67]; (2) and the point-contact probe driven by a differential micrometer, which was designed and built primarily by me. The micrometer probe is easier to use, and eanbles us to change the tip position and replace new tips without removing the whole probe from the cryostat.

The differential micrometer has two knobs for coarse and fine motion respectively. The coarse motion has a total travel of 13 mm and a resolution of 10 um, while the fine one has 200 um travel distance and 0.5 um accuracy with 70 nm sensitivity. The longitudinal motion of differential micrometer is rigidly transmitted to a long tube with a sharp tip fixed at the other end. Rotational movement of the long tube is avoided and can be withdrawn back by a compressive spring. A tight coupling of the tube to the motion guide of the probe frame avoids lateral instabilities, or "wiggling". An O-ring embedded in the brass base of the spring holder keeps tight contact with the long tube to hold vacuum. The parts above the probe frame (Upper Parts) are fixed to the frame with a clamp and can be detached for tip position

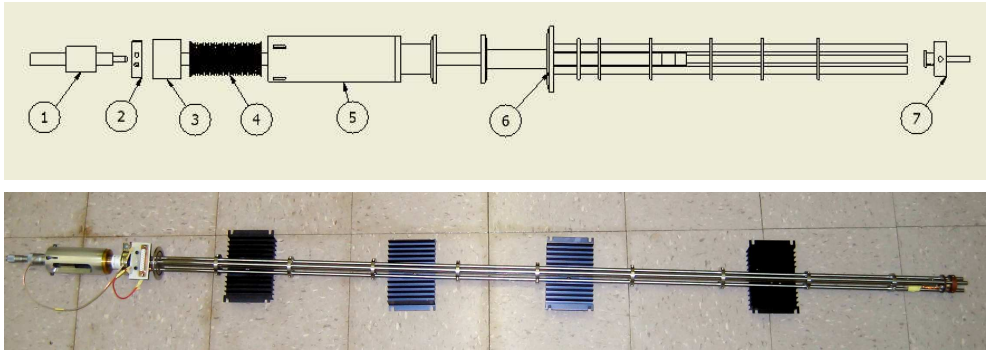

Figure 2.9: Differential micrometer PCARS probe: (Top) the illustration of probe design. Part(1) Differential micrometer; (2) Clamp collar; (3) Long tube with sub; (4) Compressive spring; (5) Spring Cavity; (6) Probe frame; (7) Sample stage. For clarity, it is not the real scale ratio for different parts. (Bottom) the picture of built probe.

change or replacement. The tip holder is electrically insulated from the long tube by a G-10 adapter. A hole with ~ 0.5 mm diameter hosting the tip is off center of the tip holder by about 0.7 mm so that the tip can engage on different points on sample when Upper Parts are rotated.

The sample holder made of oxygen-free high-conductivity (OFHC) copper is fixed to the probe frame by set-screws and can be detached easily for sample preparation. A cernox temperature sensor is embedded in the upper copper block of the sample holder with good thermal contact through Apezone N grease in between. The N grease is applied to fix the samples at room temperatures and it becomes solid at low temperatures even when pressed by tips because the N grease will get solid. All the electric wires are assembled and connected to a female pin connector, which can be easily plugged to the measurement circuit through a male connector.

The PCARS measurement circuit is exactly the same as described in the section 2.1.1 for a planar tunneling junction. Before inserting the probe into the cryostat, we record the position of the differential micrometer for the tip

where it almost touches the sample surface. We then move the micrometer back to ~ 10 mm to avoid possible tip deformation during moving and cooling of the probe. After the probe and sample are both fully cooled to ~ 2 K, we move the tip back to the previously recorded position and then gradually adjust the fine differential micrometer knob while carefully monitoring the contact resistance until tens of ohms of resistance is reached. This procedure is requiring patience to achieve stable contacts, which are needed to acquire G(V) curves.

As stated before, the Achilles' heel for PCARS is its vulnerability to the internal or environmental vibrations and disturbance since the contriction is formed through mechanical contact. We damp the environmental vibrations by placing the cryostat on top of a thick rubber sheet. For a better performance, air suspension legs or sand may be applied to isolate the cryostat from the ground and environment and damp the acoustic noise. It is found that thermal contraction from the helium vapor can also cause internal vibrations of the point-contact junctions.

2.2.2 Different Contact Regimes

Our introduction to Andreev reflection and the BTK model in the high transparency limit assumes that electrons in the normal metal keep phase coherence over a long range. In practice, electrons undergo scattering with other electrons or excitation quanta in a crystal lattice such as phonons, where l_{el} characterizes the elastic mean free path and l_{in} is the inelastic mean free path. As the junction contact area increases, as characterized by the contact diameter d, the junction can be in different regimes, as shown in Fig. 2.10, and display different behaviors (For more details, refer to [68]):

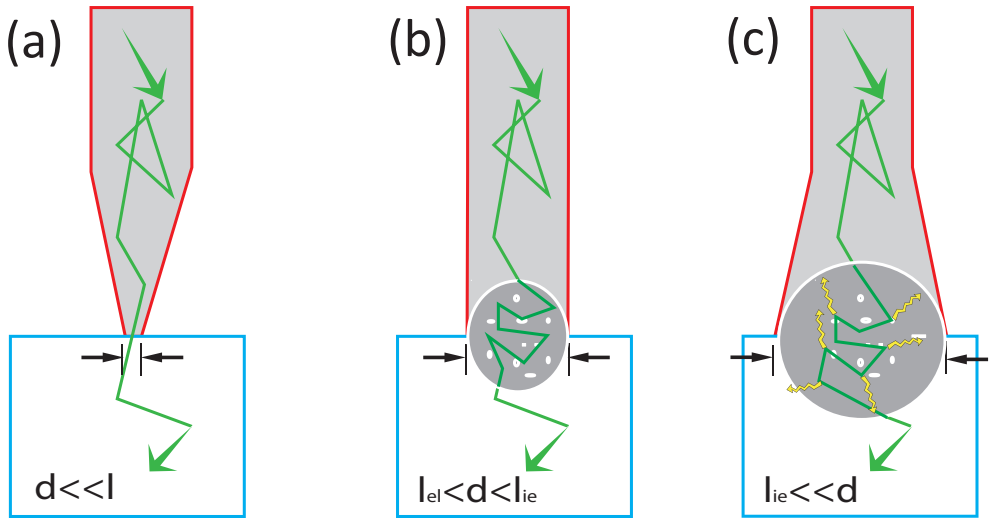

Figure 2.10: Schematic illustration of the contact junction in different regimes: (a) ballistic (Sharvin) limit when $d \ll l_{el}$; (b) diffusive regime where $l_{el} < d < l_{ie}$; (c) thermal regime when $l_{el} \gg d$

Sharvin limit In the limit of $l_{el} \gg d$, the contact resistance contributes the dominant part of the resistance in the circuit so almost all the voltage drop is between the electrodes. In this narrow channel of electron transport, electrons are accelerated by the bias voltage V without scattering and gain a kinetic energy of eV. The resistance in this case has been calculated by Sharvin with a formula (generally referred as Sharvin formula)[69]:

$$R_{sh} = \frac{16\rho l}{3\pi d^2} = \frac{16R_q}{(k_F d)^2}$$

where $\rho l = p_F/ne^2$, and $R_q = h/2e^2 \simeq 12.9k\Omega$. This Sharvin formula can be used for a simple estimation of the contact diameter from the measured contact resistance.

When the accelerated electrons pass through the constrictions of a Sharvin contact, they can be scattered by the quasiparticle excitations in the other electrode and relax the excessive energy of eV gained from the biased voltage, as shown in Fig. 2.11. Some of the scattered electrons will be reflected back to the initial electrode creating a current backflow. If the scattering is from a

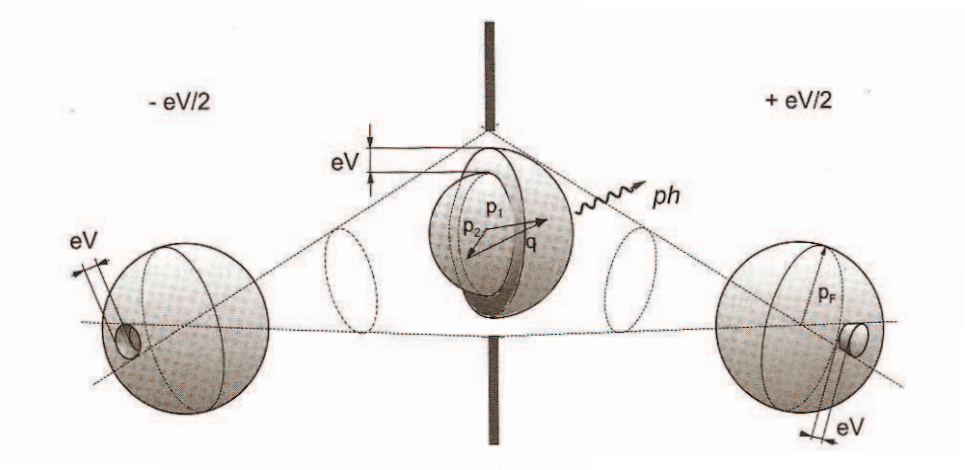

Figure 2.11: Electron distribution function with a voltage bias, V, for the ballistic point-contact in both electrodes and the constriction. p_1 and p_2 are the initial and final momentum, respectively. q is the excited phonon momentum and p_F the Fermi momentum. Adapted from [68].

phonon or lattice vibration, the energy-dependent scattering is proportional to the electron-phonon coupling coefficient and the phonon densities at that energy. It is mathematically proved that [70]:

$$\frac{1}{R^2}\frac{d^2V}{dI^2} = \frac{1}{R}\frac{dR(V)}{dV} = \frac{8ed}{3\hbar v_F} g(\omega)|_{\hbar\omega=eV} \propto \alpha^2 F(\omega)$$

Thus, 2nd harmonic measurements of point-contact spectra in the Sharvin limit is also a method to get the quasiparticle excitation spectra, similar to the case of tunneling, although the physical origins are different.

Diffusive regime It is not always easy to make the contact in the Sharvin ballistic limit, however, after elastic scattering at the interface, electrons can still retain some spectroscopic information in the diffusive regime ($l_{el} < d < \sqrt{l_{el} l_{in}}$). In this regime, the contact resistance can be derived from a formula by Wexler (1966) generally referred as Wexler formula [71], including

parameters d and l_{el}:

$$R_W(T) = \frac{16\rho l}{3\pi d^2} + \beta\frac{\rho(T)}{d} = R_S + \Gamma(K)R_M = R_S[1 + \frac{3\pi}{8}\Gamma(K)\frac{d}{l}]$$

where K=l/d is the Knudsen number and $\Gamma(K)$ is a slowly varying function of order unity. The second term, $\frac{\rho}{d}$, is called the Maxwell term in the diffusive limit. As we can see, in the ballistic limit, $\frac{d}{l} \ll 1$, The Wexler resistance recovers to the Sharvin resistance.

Thermal regime In the case $d \gg l_{in}$, the contact area is so large that electrons crossing the interface undergo many inelastic scatterings and lose spectroscopic information. The dominant contribution of resistance comes from the Maxwell term, and temperature at the contact area is much higher than the environment due to its local Joule heating. There is a relation between the local temperature T_{PC} and the bias voltage V: $T_{PC} = \sqrt{T_{bath}^2 + \frac{V^2}{4L}} \sim \frac{1}{3.63}eV$, where T_{bath} is the bath temperature and L is the Lorentz number $L = L_0 = 2.45 \times 10^{-8}V^2/K^2$.

2.2.3 PCARS Diagnostics

Several careful diagnostics must be applied to PCARS spectra obtained to assure intrinsic, spectroscopic data. Reproducibility is the most important diagnostic.

Sample Preparation

Materials with a large electronic mfp allow reaching the Sharvin limit more easily. Also smooth surfaces reduce the chance of impurity scattering at

the junction interface. The current density, J, at the contact area can be quite high since $J = I/S = [(e^2/4\hbar)(k_F d)^2 V]/[\pi d^2/4] = 2e^2 k_F^2 V/h$. At the superconductor coherence length, ξ, the current density is reduced to $J' = J(a/\xi)^2$. The larger the coherence length, the lower the probability that the current density reaches the superconductor critical current density and destroys superconductivity locally. PCARS is therefore better suited to probe samples with a longer mean free path and a longer coherence length.

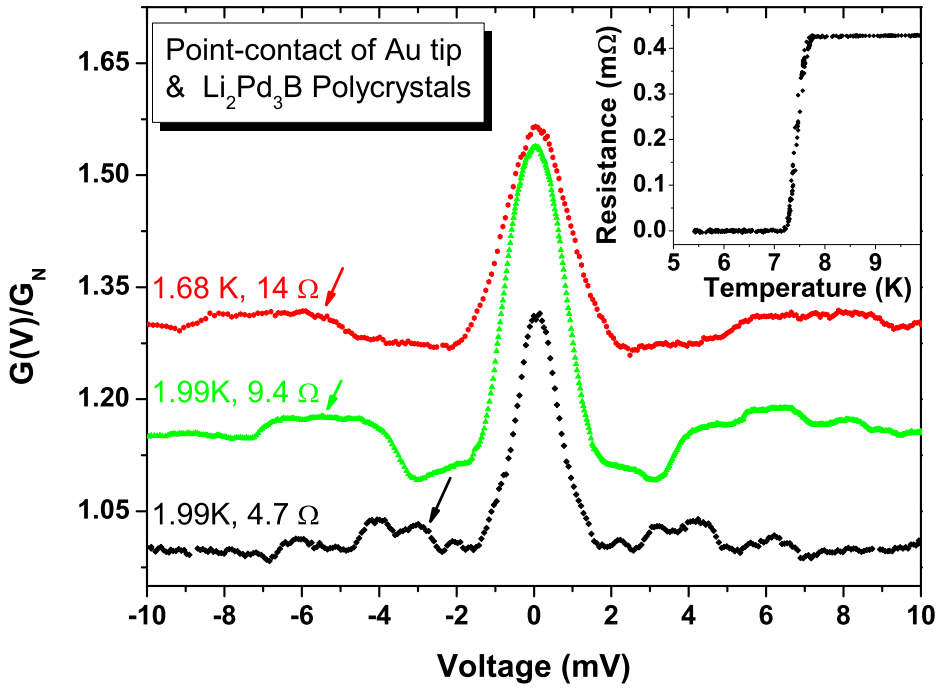

Figure 2.12: Normalized G(V) curves of Au/Li_2Pd_3B(polycrystal) point-contact junctions. There are side fine structures indicated by arrows probably due to thnce dependent on temperature with $T_c \sim 7.3$ K.
e intergrain Josephson coupling. The curves are shifted for clarity. The inset shows one Li_2Pd_3B sample resista

In the initial stage of a discovered superconductor, the samples available are usually polycrystalline, which imposes some potential problems to PCARS. Generally, the polycrystalline samples are packed with many small single grains with intergrain Josephson coupling between them. Two issues

are involved: (1) multiple point-contacts may be formed at the contact area with some grains having poorer superconducting properties ; (2) The intergrain Josephson coupling can be modeled in series with the actual contact resistance and has a non-linear I-V characteristic, which complicates the spectra measured and corresponding interpretation of the data. Fig. 2.12 shows an example of point-contact conductance curves biased between the Au tip and Li_2Pd_3B polycrystalline samples. The extra fine structures around the zero-bias peak, are possibly due to the intergrain Josephson coupling. Experimental evidence indicates Li_2Pd_3B is likely an s-wave superconductor [72, 73]. The zero-bias peak observed here is also frequently present in other polycrystalline samples, and is not associated with Andreev bound states due to the sign change of the order parameter. Diagnostics, such as the conductance spectra dependences on applied magnetic field and temperature are required to determine if the ZBCP arises from ABS, but the polycrystalline nature makes interpretation difficult. If the grains in the polycrystalline samples are large enough, then a point-contact junction may be achieved on a single grain and PCARS can then probe the intrinsic gap properties. Single crystal samples are of course favored due to their homogeneity across a large area. Also in single crystals, directional PCARS can be performed with current injected along different crystallographic orientations where single crystals with different surface orientations can be prepared.

Surface Treatment Since Andreev reflection is an electron-hole conversion process with phase coherence happening at the normal metal-superconductor interface, it is critical for PCARS to probe a clean superconducting surface. However, in practice, the samples may be susceptible to surface oxidation or degradation, which brings an extra impurity layer between the tip and

superconducting samples. This broadens and reduces the Andreev reflection signal. As an example, Fig.2.13 shows the G(V) evolution of point-contact junctions between the Au tip and a thermally-evaporated Pb film. For the initial gentle contact, a zero-bias peak is observed. As the tip pressure is increased and contact resistance decreased, a double-peak structure emerges as expected from BTK model emerges. This change is probably due to the tip puncturing an oxide layer on the surface and contacting directly with the underlying superconducting Pb.

Sometimes, it is not easy for the sharp tip to get through the natural oxide layer,and the local T_c is reduced or the surface of the material is not superconducting at all. In these cases, no Andreev reflection, or a reduced local T_c is observed for PCARS. Physical or chemical etching, such as ion milling or acid etching, may be used to remove the surface layer and expose a clean surface with full superconductivity as in the bulk. The oxide surface layer may also be removed by polishing, but the processes may also degrade superconductivity at the exposed surface. A preferred method to expose a clean surface easily applied to many quasi 2-D materials($NbSe_2$, iron-pnictide, cuprate superconductors...) is cleaving.

Data Diagnostics

Diagnostics to determine that the contact is in the Sharvin limit are required. Even more important is reproducibility. Many point-contact G(V) curves must be collected and statistical analysis is applied to determine the intrinsic, reproducible features contact to contact. A normal metal tip in point-contact with a superconductor can produce dips outside the normal Andreev reflection. For example, G(V) curves for point-contact between Au tip and Nb films shown in Fig. 2.14 all have dips outside the Andreev reflec-

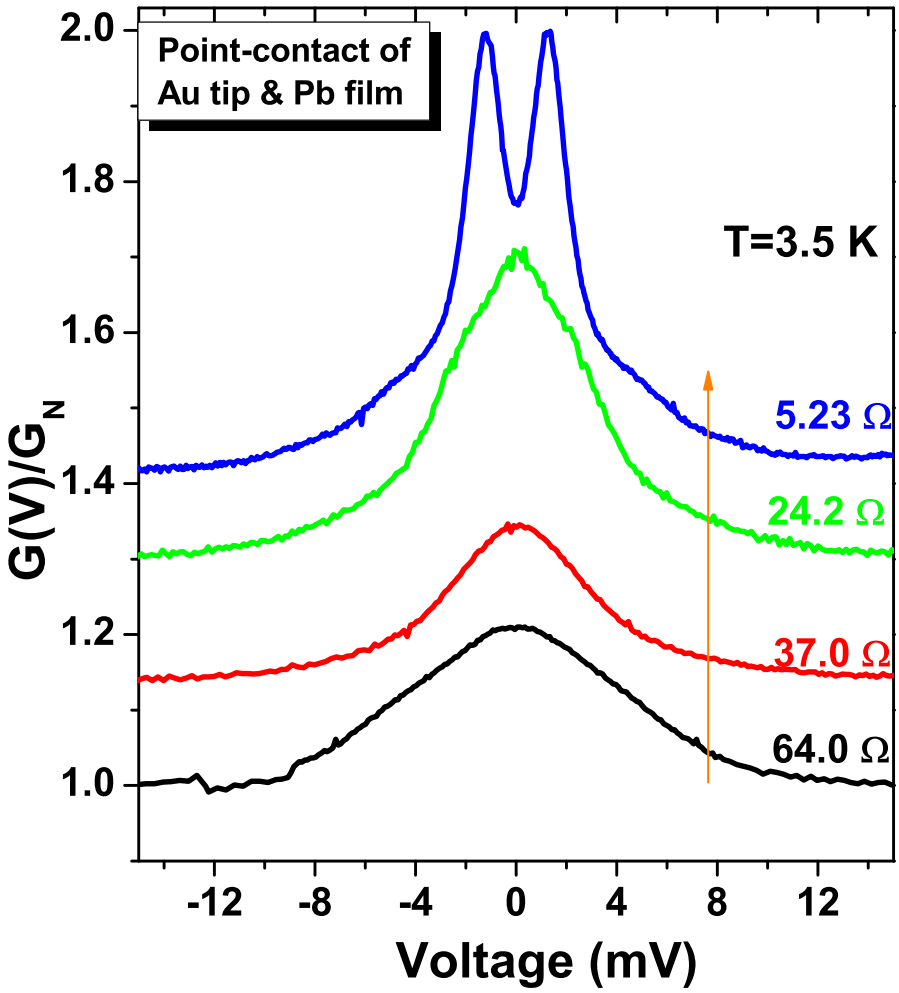

Figure 2.13: G(V) evolution of Au/Pb film point-contact junctions as a function of tip pressure and thus contact resistance. As pressure increases, the Au tip likely penetrates through a surface oxide layer, and a double-peak structure around $\sim \pm 1.4$ meV emerges at a junction resistance of R=5.23Ω, consistent with the BTK model.

tion peaks. While the position of the Andreev reflection peaks is relatively constant around $\pm$ 1.5 meV, the dip position and shape changes from contact to contact, and is dependent on the individual contact geometry. In the case of a zero-bias peak as shown in Fig. 2.14(f), since Nb is an s-wave superconductor, it is definitely not due to Andreev bound states as in cuprates.

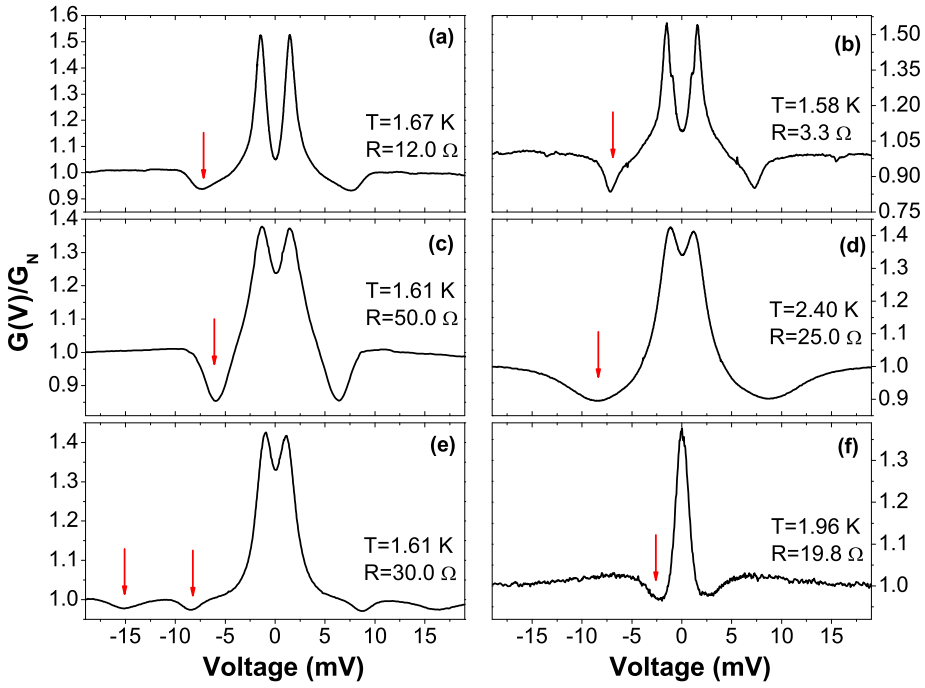

Figure 2.14: Various dip structures observed in the point-contact junctions between the Au tip and Nb film. The dips are indicated by arrows above their positions.

Figure 2.15 shows the temperature dependent G(V) curves of a point-contact junction between a Au tip and Nb film. There are two apparent dips in the conductances referred as Dip 1 and Dip 2. If we simply track the positions of each dip as a function of temperature shown in the inset of Fig. 2.15, they both follow that of the BCS gap. Thus the dips are intimately related to superconductivity, however, they are not generic feature of the superconductor, varying from contact to contact,and we conclude the G(v) curves are not completely spectroscopic.

There are two popular models proposed to explain the origin of the dip structure frequently observed in N-S point-contact junctions [74, 75]. In the local heating model, point-contact junctions are considered which are larger than the ballistic limit. As discussed in the section 2.2.2, the contact resistance in the diffusive regime R, $R = R_S + \Gamma(l/d)R_M$, can be regarded

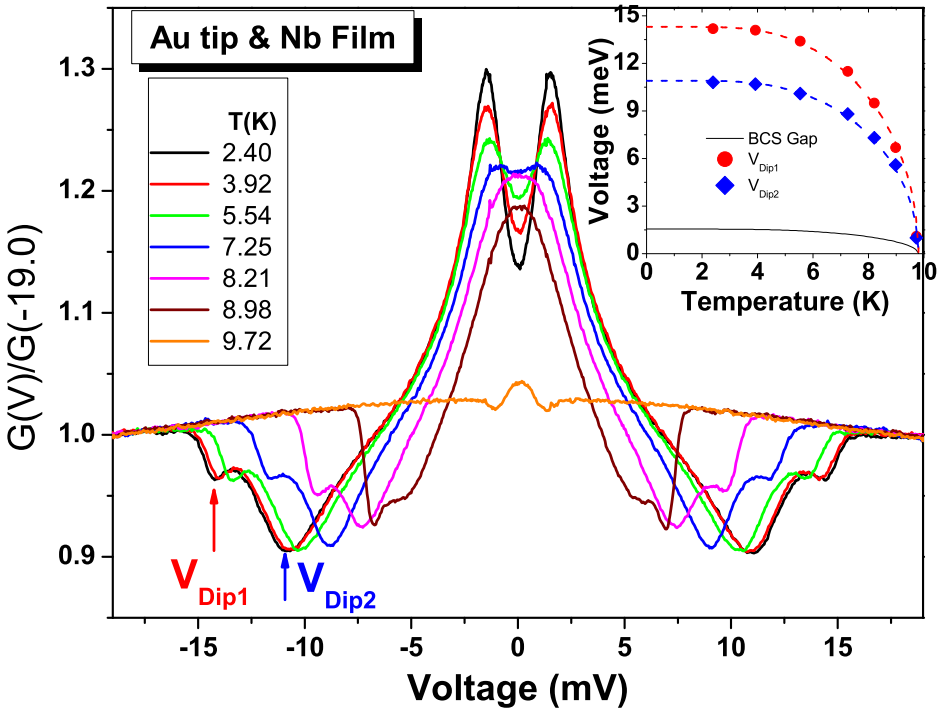

Figure 2.15: Temperature dependent G(V) curves of a Au tip/Nb film Point-contact junction with Dip1 and Dip2 indicated by the red and blue arrows respectively. The inset shows the temperature evolution of each dip position. Measurement is taken before the temperature sensor calibration. The dashed lines are guide lines showing the BCS gap-like trend.

as a series circuit with a Sharvin resistor and a pure Maxwell resistor. In the superconducting state, the superconductor does not contribute to the Maxwell term due to its zero resistance. However, when the junction current reaches the critical current at a finite bias voltage, the resistance in the normal state is recovered. There is a jump of the resistance from this extra Maxwell term and thus a dip in G(V) curves. As the contact diameter increases, the Maxwell resistance contributes more to the total resistance and the dip structure is more pronounced, as shown in Fig. 2.16. These curves are calculated by adding the extra Maxwell term to the standard BTK-like conductance.

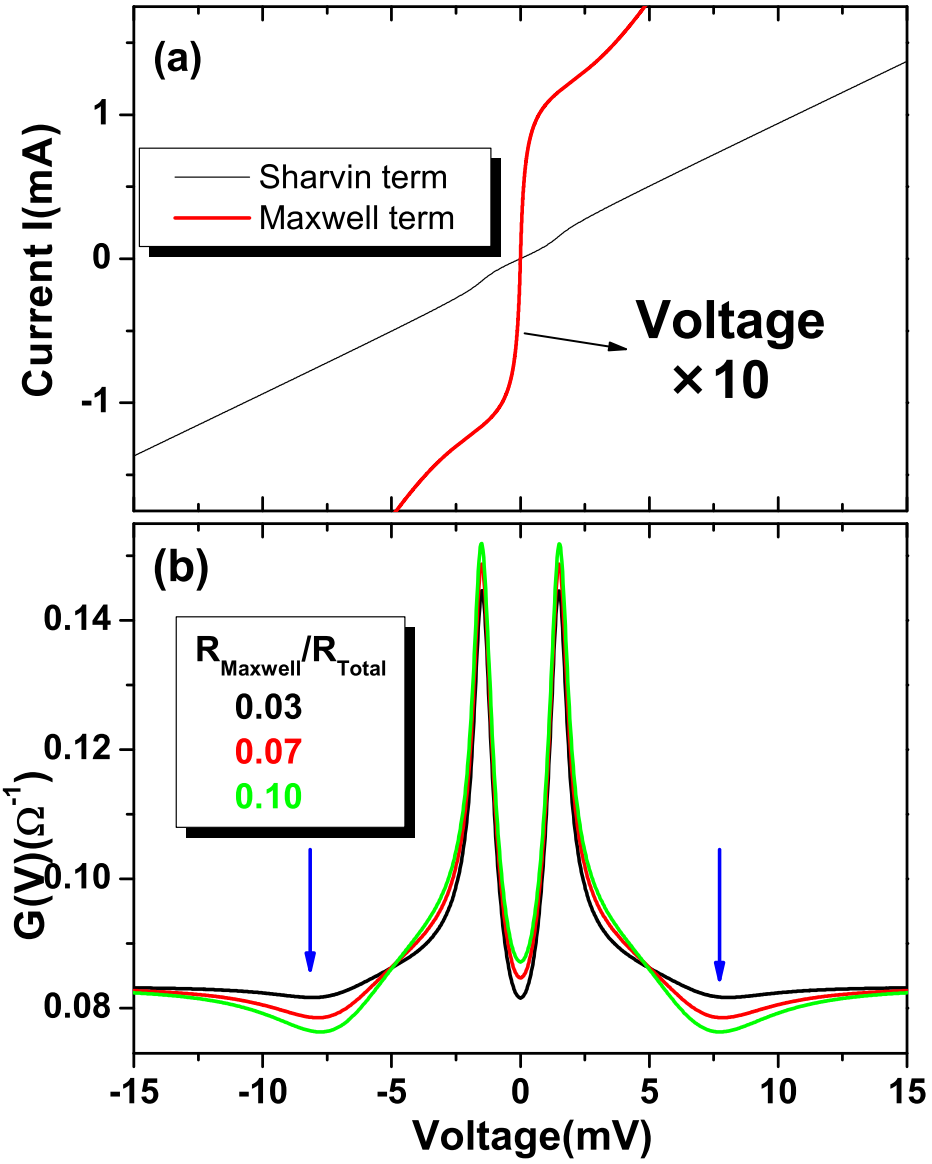

Figure 2.16: The calculated curves for the normal metal and superconductor point-contact junctions with the critical current effect. (a) the current-voltage curves for the calculated Sharvin term (black) calculated from BTK model (Δ=1.55 meV, Z=0.6, Γ=0.1 meV) and assumed Maxwell term (red, the voltage is magnified 10 times). (b) The calculated G(V) curves varying the $R_{Maxwell}/R_{Total}$ ratio from 3% to 10%. The arrows indicate the dip structure due to the critical current. Note how the dip intensifies with increasing Maxwell resistance.

Chapter 3

PCARS on $NbSe_2$

3.1 Introduction

Layered transition-metal dichalcogenides 2H-$NbSe_2$ still attract an attention due to their fascinating properties, despite the fact that extensive research has been done during the past decades. Each crystal unit has one Nb and two Se atomic layers in a hexagonal structure, with Nb sitting at the center of a trigonal Se prism, as shown in Fig. 3.1(a) and (b). For this sandwich-like Se-Nb-Se layer, atoms are bonded by strong covalent interactions, while separate Se-Nb-Se layers are hold together by weak Van-der-Waals forces. This results in a very large electronic anisotropy in resistivity and thus a quasi two-dimensional nature. In experiment, it is also quite easy to achieve an atomically-flat surface from a cleaved sample suitable for STM. According to the band structure calculation, as illustrated in Fig. 3.1(c), a small pancake-like FS (16th band) in the center of the BZ derives from the Se 4p-related orbits, while two cylindrical FSs centered at the ΓA and KH lines (17th and 18th bands) originate from the Nb 4d orbits. All these Fermi sheets have been observed by ARPES and De-Haas-van Alphen (dHvA) experiments [77, 78, 79, 83, 84].

The coexistence of a charge-density-wave (CDW) and superconductivity (SC) phases in 2H-$NbSe_2$ makes it a particularly good material to understand the relationship between CDW and SC orders and their electronic origins.

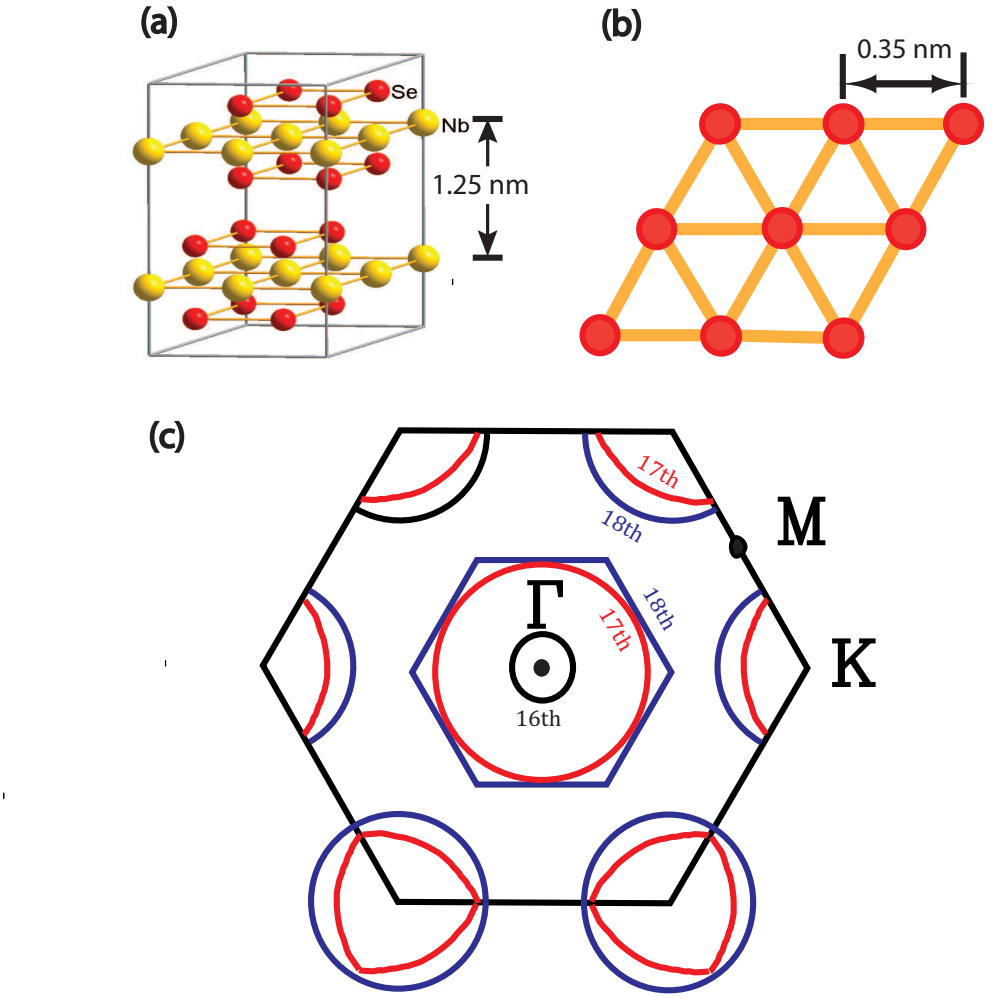

Figure 3.1: (a) The crystal unit cell of $NbSe_2$ with Se-Nb-Se sandwich structure. (Adapted from http://www.phys.psu.edu/~liu/EM_alex.htm) (b) The in-plane hexagonal structure of a Se layer. (c) Fermi surface sheets from the Nb-4d and Se-4p orbits in the 2-dimensional Brillouin zone with generally referred symmetry points.

The incommensurate CDW state occurs below T_{CDW}=33.5 K with a wave vector $\mathbf{Q}_{CDW}$ parallel to the ΓM directions of the hexagonal Brillouin zone (BZ) and $Q_{CDW}=\frac{2}{3}|\Gamma M|(1-\delta)$, where $\delta \sim 0.02$. The mechanism for the CDW instability in $NbSe_2$ is still under heated debate with two different viewpoints [77, 78, 79, 80]: one proposed mechanism considers Fermi Surface

(FS) nesting involving the FS around either the Γ or K points with parallel FS sections connected by wave vectors consistent with the reported $\mathbf{Q}_{CDW}$. In the other mechanism proposed by Rice and Scott, two saddle points separated in **k**-space close to the Fermi level give rise to the CDW vector. $NbSe_2$ is also a type II superconductor, with T_C=7.2 K and H_{C_2} ∼32 KG perpendicular to the plane [81]. With increasing hydrolic pressure, it is found that T_{SC} increases while T_{CDW} decreases, suggesting competition between SC and CDW over the FS [82].

Recent studies of the superconducting state in $NbSe_2$ have uncovered its anomalous properties such as a superconducting gap variation. Multiband or an anisotropic superconducting gap in $NbSe_2$ has been claimed from different experimental measurements such as thermal conductivity [86], STM [85, 90, 91], penetration depth [88] and specific heat [87, 89]. Angle-resolved photoemission (ARPES) measurements have indicated sizable magnitude differences in the superconducting gaps on two sets of FS sheets [83], similar to MgB_2 [34, 35, 36], which probably favors the multiband scenario.

Point-contact Andreev reflection spectroscopy (PCARS) can unveil superconducting gap structure and the order parameter symmetry. However, for $NbSe_2$, we are only aware of one article by P. Martínez-Samper *et al.* which characterizes the transition from tunnelling to contact regime by engaging STM tip gradually on the sample surface [92].We now illustrate the ability for PCARS to achieve spectroscopic information on the gap structure in NbS_2.

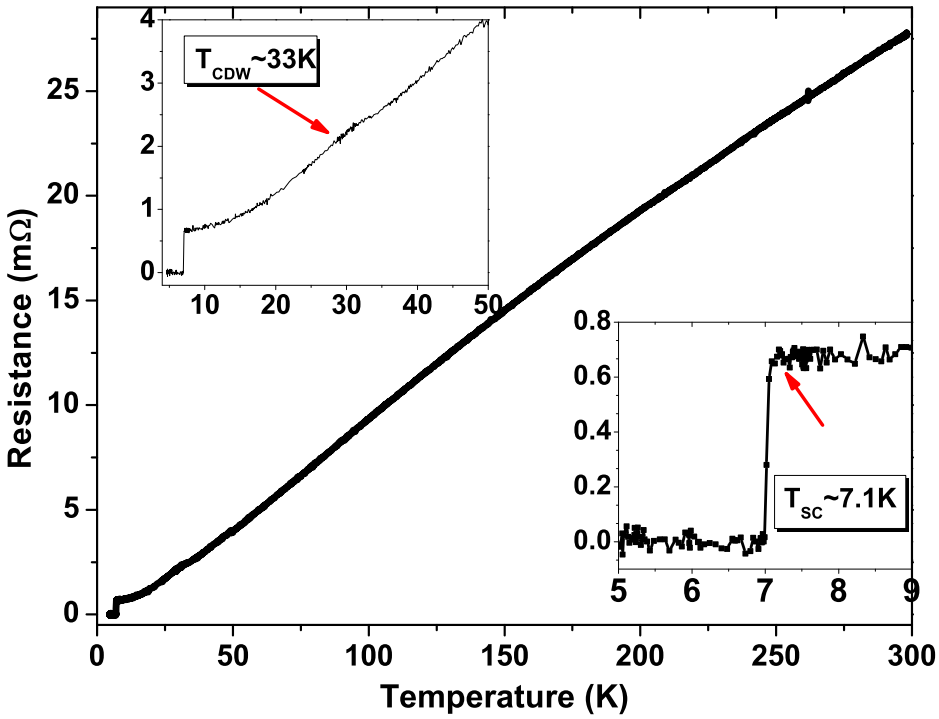

Figure 3.2: (a) Temperature dependent in-plane electrical resistance of the $NbSe_2$ single crystal. the upper inset shows a small resistance kink induced by CDW transition around 33 K while the bottom one the superconducting transition detail around T_c ∼7.1 K.

3.2 Experimental Results and Discussions

High-quality $NbSe_2$ single crystals are available for PCARS with T_c ∼7.1 K and RRR∼42, while the temperature-dependent resistance is shown in Fig. 3.2. They are cleaved in air to expose a fresh and shinny surface before being mounted on the sample holder. Dozens contacts have been made at low temperatures and, while some contacts are lost due to vibration or thermal instability, we manage, in several contacts,to change the temperatures up to the bulk critical temperature.

The resistivity measurement indicates a large anisotropy $\rho_c/\rho_{ab} \sim 100$. The inplane mean free path l_{ab} is estimated to be ∼1830 Å from inplane residual resistivity and carrier concentration measurements [93]. Thus the

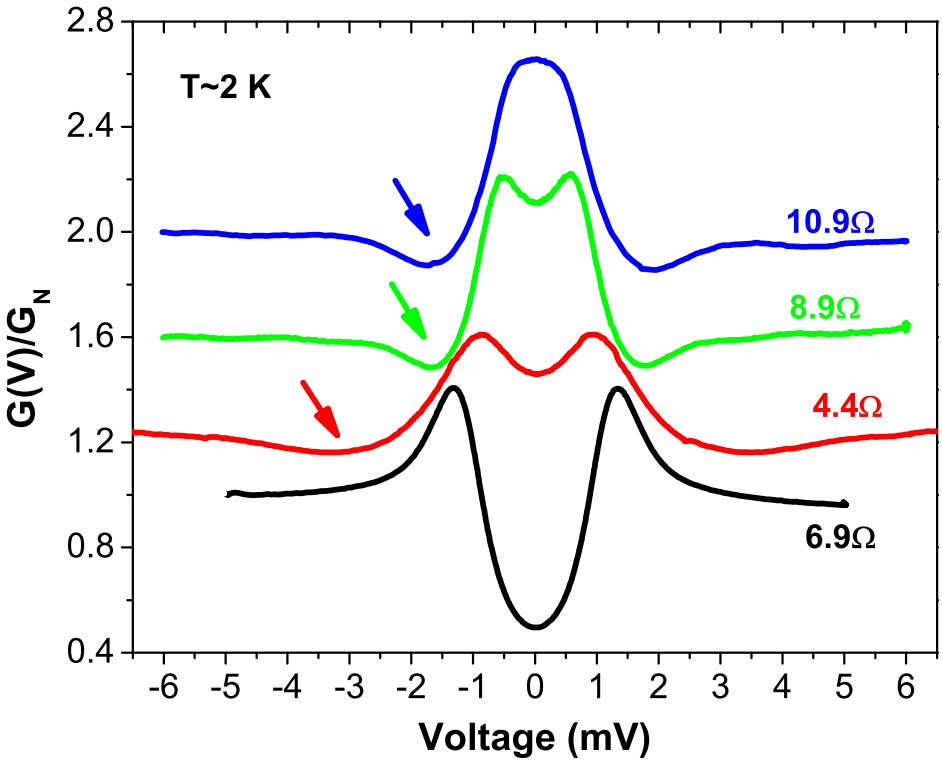

Figure 3.3: Different differential conductance curves for the Au/$NbSe_2$ contact junctions with some contacts in the diffusive regime where dips can be observed shown with arrows.

mean free path in c direction is only ∼20 Å making it difficult to reach the ballistic limit point-contacts for that direction. Furthermore, the $NbSe_2$ crystal surface is soft and the contact pressure tends to deform the surface layer producing a larger contact area in the contact region. For the contact in the diffusive regime, dips appear outside the superconducting gap as shown in the Fig. 3.3 and the Andreev reflection peaks are broadened. There is also no correlated relationship between the contact resistance and the dip structure. In order to access the ballistic limit, a sharp Au tip is required, although the contact is sometimes not stable due to the small contact area.

Figure 3.4 (a) shows the point-contact G(V) curves normalized to the normal conductance at T=7.35 K as a function of temperature. The conduc-

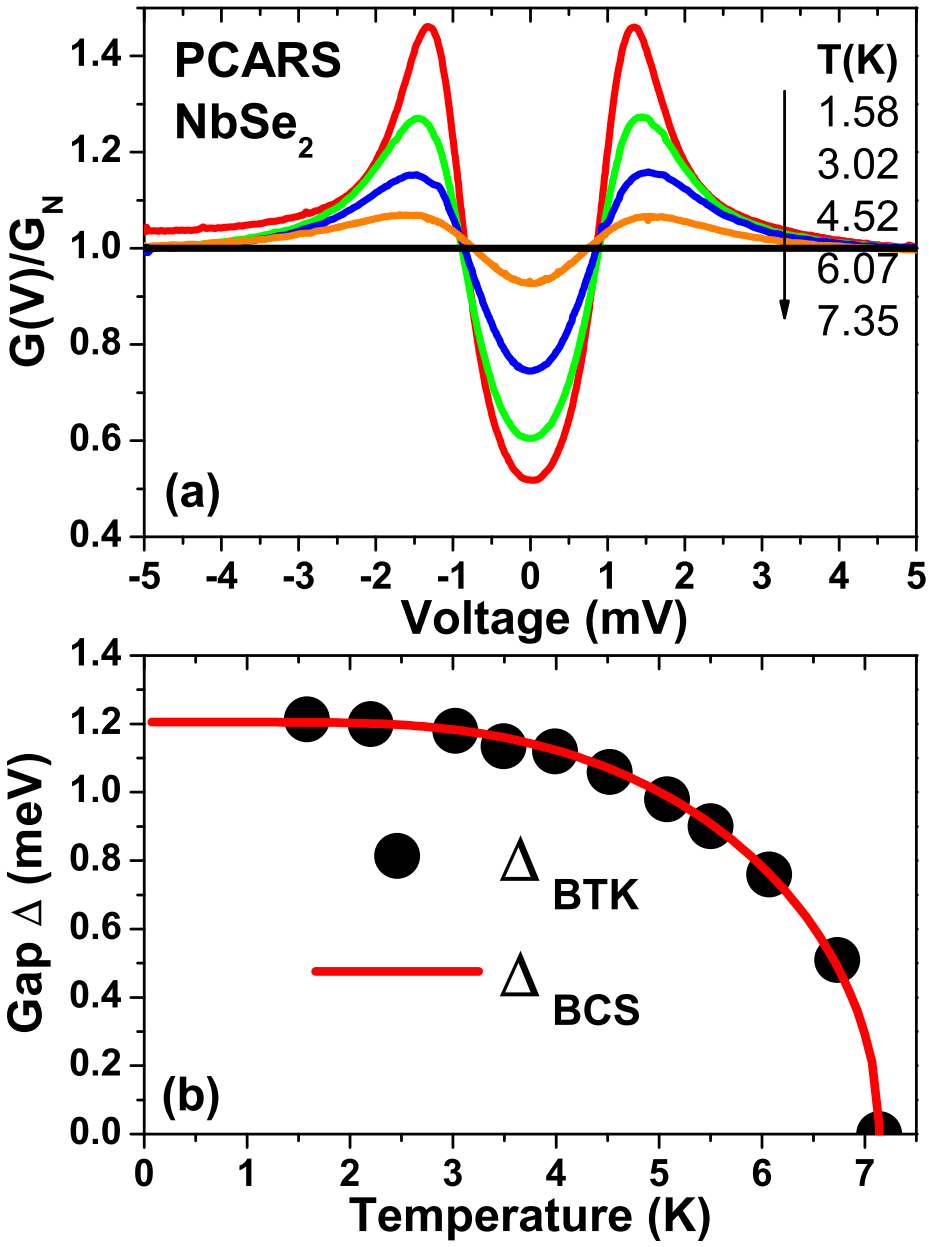

Figure 3.4: (a) The normalized differential conductances G(V) for Au/$NbSe_2$ point-contact junctions evolving with temperatures from 1.58 K to 7.35 K. (b) The temperature-dependent superconducting gap from the best BTK fits for the data in (a) (full circle) in comparison with the BCS-like fit(solid line).

tance curves do not show dip structures and can be fit well with single-band BTK model, indicating the contact is in the ballistic limit. The temperature dependence of the superconducting gap follows the BCS-like curve as shown

in Fig. 3.4 (b). However, the extracted $2\Delta_0/k_BT_c \sim 3.89$ ($\Delta_0 = 1.2$ meV) is somewhat larger than the single-band s-wave BCS ratio 3.52. ARPES measurements report the Nb 4d-derived 17th and 18th bands show T=0 extrapolated superconducting gap sizes 1.22 and 1.13 meV, respectively, while the Se 4p-derived 16th band exhibit a gap at 5.3 K of 0.2 meV or less(resolution limited) [83]. STM studies [85] also reveal a two-band feature, where the larger-gap band follows a BCS-like temperature evolution with $2\Delta_0/k_BT_c \sim 3.9$ and other smaller-gap band has a behavior predicted by Suhl *et al.* for the case of small interband scattering between the two bands [94]. The superconducting gap probed by PCARS here is comparable with the gap size from the Nb 4d-related band reported by ARPES and STM.

In order to see whether this multiband feature of $NbSe_2$ can be observed in PCARS the same as for MgB_2, conductances of dozens of contacts without dip structure are considered. There is no pronounced double-peak feature observed similar to the point-contact spectra of MgB_2, possibly due to the small difference of the gap sizes between the two bands. Moreover, the large voltage spans at a high temperature for each peak will also smear the gap between the peaks, making it impossible to resolve the detailed features, as in the case of Rayleigh criterion in optics. However, depending on the relative weight from each band, the effective gap size can be close to either of the two gap values. Fig. 3.5(a) show a few point-contact conductance curves at T$\sim$2 K and the corresponding simulated curves from the best BTK fit. For the nine stable contacts with BTK-like conductance curves, the simulated gap ranges from 0.9 to 1.5 meV with the distribution shown in Fig. 3.5(b). The minimum gap size is close to the smaller gap 0.85 meV reported in [89] and 0.75 meV in [85, 90] and the maximum gap around 1.3 and 1.4 meV is also consistent with other reports.

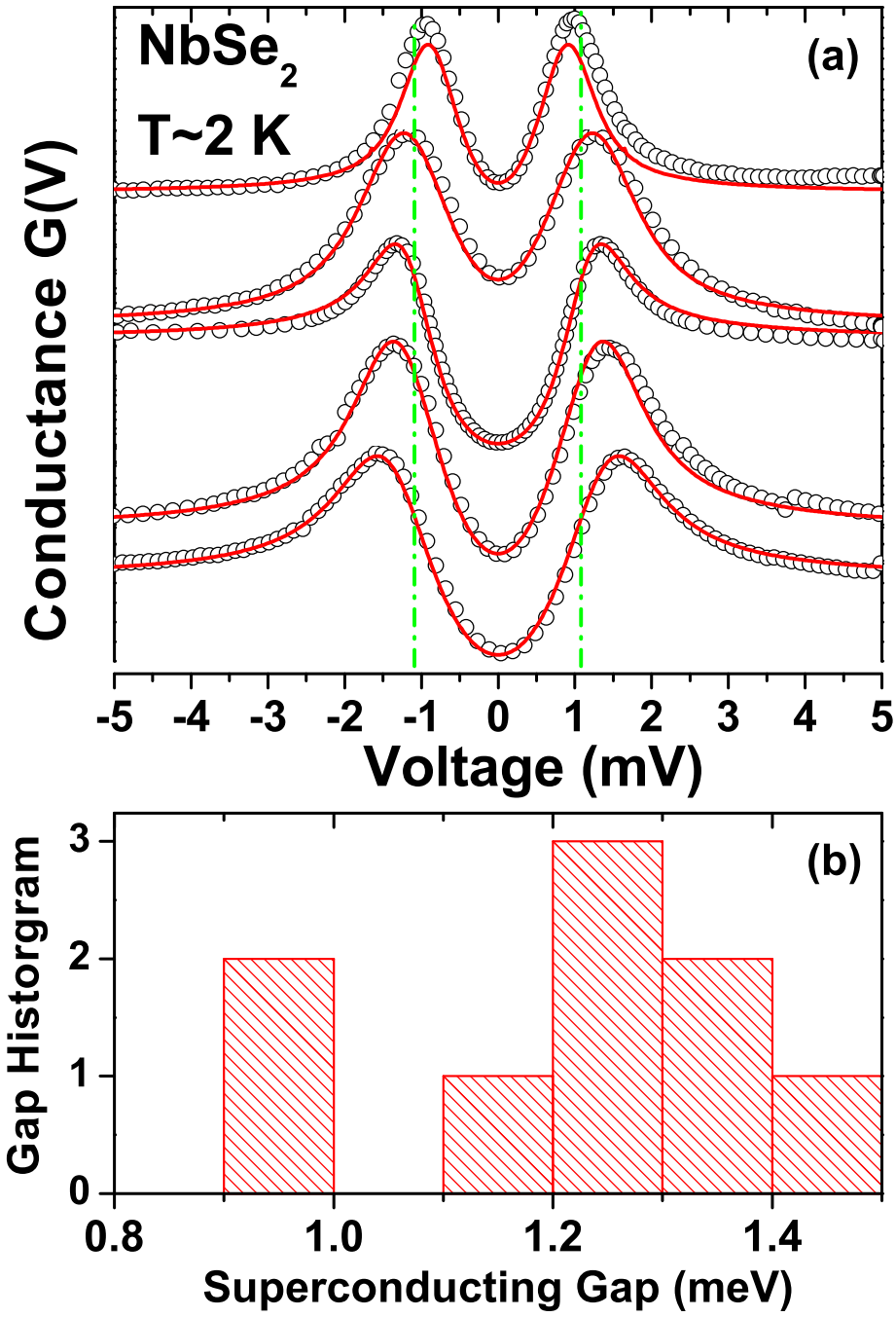

Figure 3.5: (a) The differential conductance curves, G(V), at T ~2 K for different contacts between Au tip and $NbSe_2$. The green dashed line is the gap position, 1.08 meV, predicted by BCS weak-coupling ratio. (b) The gap distribution for nine contacts with BTK-like G(V) curves.

In conclusion, BTK-like G(V) curves are obtained for the point-contact Au/$NbSe_2$ junctions. The single-gap BTK fit to the PCARS data give the gap value from 0.9 to 1.5 meV, consist with the multigap scenario claimed by other experiments. The superconducting gap follows the BCS-like temperature-dependent curve.

Chapter 4

PCARS on Borocarbides

4.1 Introduction

The superconducting borocarbide family RNi_2B_2C (R=Y, Lu, Dy, Ho, Er) has been intensively investigated ever since its discovery due to its exotic superconducting properties and interesting coexistence of magnetism and superconductivity. As shown in Fig. 4.1(a), the crystal unit cell has a body-centered tetragonal structure, consisting R-C planes separated by Ni_2B_2 layers in the c-axis. The non-magnetic borocarbides $LuNi_2B_2C$ and YNi_2B_2C have the highest superconducting transition temperature among this family with T_c ~16.5 K and 15.5 K, respectively. The magnetic borocarbides serve as a fascinating family to study the coexisting and competing effect of superconductivity and magnetism with a systematic evolution of T_c and T_N at a comparative temperature scale, in contrast to the general exclusion of these two orders. The superconducting and magnetic states have different origins in RNi_2B_2C: the magnetic moment comes from the localized R^{3+} 4f electrons while the superconducting condensation originates in the itinerant 3d electrons, mainly from the Ni_2B_2 layers. Fig.4.1(b) shows good scaling behavior of T_N with the de-Gennes factor $dG = (g-1)^2 J(J+1)$ where g is the Landé g factor and J the angular momentum of the R^{3+} ions. This indicates that the interactions between localized 4f electron moments are mediated by the RKKY interactions through the conduction electrons of the Ni_2B_2 layer between the RC planes in the c-axis direction. The inverse scaling of superconducting T_c with the de-Gennes factor proves the competition between SC

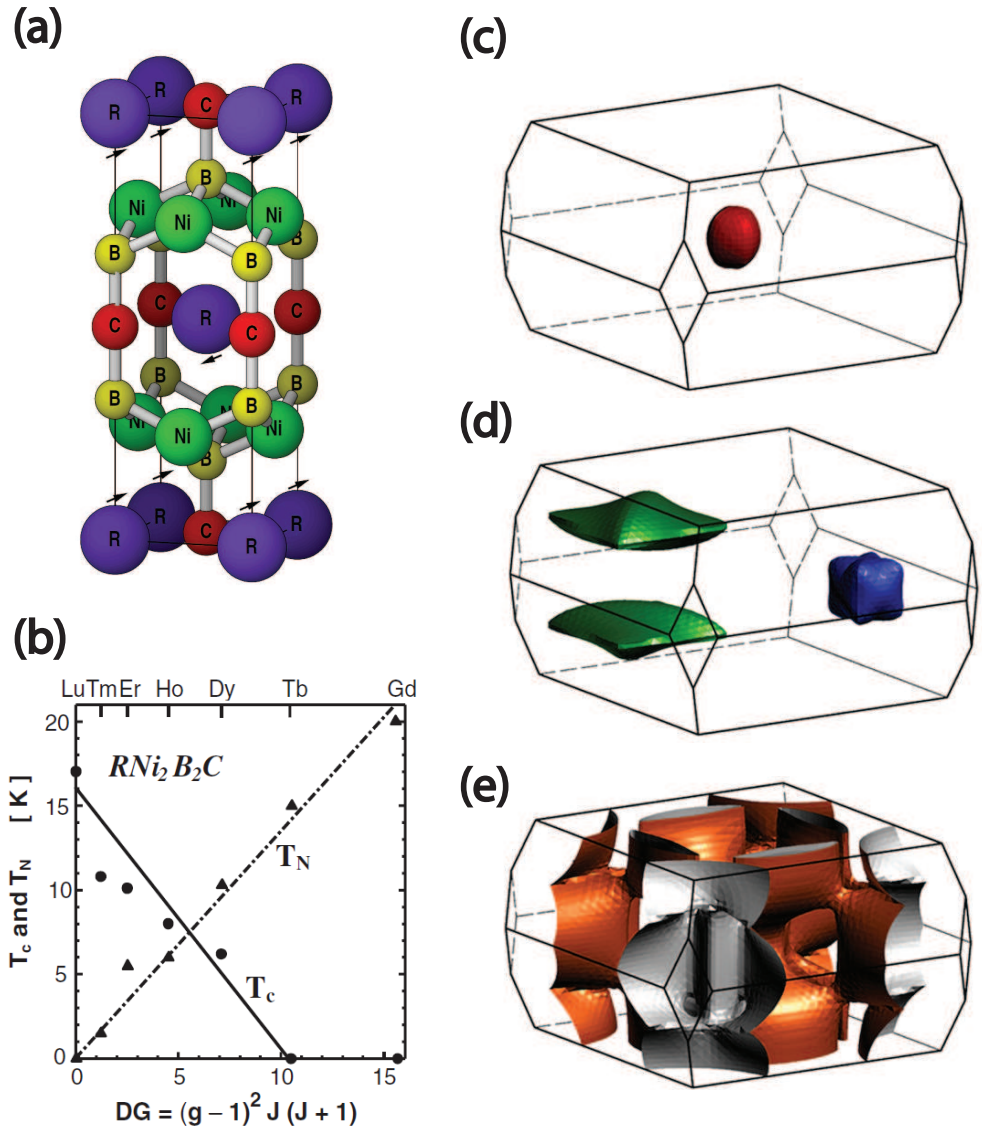

Figure 4.1: (a) Crystal unit cell of RNi_2B_2C with a tetragonal structure. (Adapted from P. Thalmeier and G. Zwicknagl 2003 arXiv:0312540) (b) Superconductivity critical temperature, T_c, and antiferromagnetic Neel temperature, T_N, for RNi_2B_2C family with R=Lu, Th, Er, Ho, Dy, Tb, Gd as a function of the De-Gennes factor,$dG = (g-1)^2 J(J+1)$. (Adapted from K. H. Müller *Rep. Prog. Phys.* **64** 943, 2001). The Fermi surface from band structure calculation is shown in the Brillouin's zone for (c) 19th, (d) 18th, (e) 17th bands. (Adapted from B. Bergk *et al. Phys. Rev. Lett.* **100** 257004, 2008)

and magnetic orders due to the latter's weak perturbation over the Fermi surface.

Non-magnetic borocarbides RNi_2B_2C (R = Y, Lu) have also attracted much interest, and its detailed superconducting gap structures are still controversial despite intensive studies over the past decade. Thermal conductivity [95], Raman Scattering [96], and photoemission spectroscopy [97] data indicated a large anisotropy in the gap function. Experiments on field-angle-dependence of the thermal conductivity [98] and specific heat [99, 100] displayed a four-fold oscillation in amplitude and suggested the possible existence of point nodes along the a and b axes.

S+g pairing symmetry is proposed to match the point-node gap structure [101]. In another scenario, point nodes are proposed to originate from the antiferromagnetic(AFM) fluctuation on some parts of Fermi surface connected by a nesting vector. According to the LDA band structure calculation for the borocarbide family, a nesting feature on the FS is predicted with nesting vector $\mathbf{Q} \approx 2\pi(0.5/a, 0), 2\pi(0, 0.5/a)$ in the basal plane. This has been directly observed using two-dimensional angular correlation of the electron-positron annihilation radiation technique in $LuNi_2B_2C$ [102]. Additionally, the AFM ordering in the corresponding magnetic compounds have a wavevector $\mathbf{Q}_m \approx 2\pi(0.55/a, 0, 0)$ very close to the nesting vector. The nesting feature would generally weaken the electron-phonon (e-p) coupling along $\mathbf{Q}$ and result in a gap anisotropy. An e-p coupling feature is observed and an anisotropic s-wave is claimed based on the tunneling spectroscopy with high resolution STM [103], where the anisotropic gap was interpreted as the result of highly anisotropic e-p coupling due to soft phonons. Moreover, Kontani predicted a simple anisotropic s-wave with point-node-like gap minimum connected by the nesting vector $\mathbf{Q}$ due to the coexistence of strong

e-p coupling and AF fluctuations in (Y,Lu)Ni_2B_2C [104].

The temperature dependence of the upper critical field [105] and directional point-contact Andreev reflection spectroscopy (PCARS) [106, 107, 108] results have been interpreted using a multi-band/multi-gap order parameter scenario considering the complicated Fermi surface (FS) [109, 110]. The reported gap anisotropies are extremely disparate among different groups [106, 107] both in the gap ratio between c and a-axis directions and in the temperature dependence. In this chapter, we describe our systematic PCARS studies aimed at clarification of the gap structure in $LuNi_2B_2C$ and YNi_2B_2C [111].

4.2 PCARS on $LuNi_2B_2C$

4.2.1 Sample Preparation

High-quality $LuNi_2B_2C$ single crystals with $T_c \sim 16.0$ K are grown in a Ni_2B flux as c-axis platelets. Two sets of $LuNi_2B_2C$ samples from different groups are prepared along three major crystallographic orientations([001], [110], and [100]) so that we can inject current along different directions and record the point-contact conductance spectra. In order to expose the [100] and [110] surfaces, crystals are embedded in epoxy fixed in the desired direction and polished with alumina lapping film of decreasing grain sizes in sequence (12, 3, 1, 0.3 μm) and finally with silicon colloid suspension of 0.02 μm size of particles. For the first set, samples in [001], [110] and [100] directions are from three different single crystals and their electrical resistance is shown in Fig. 4.2 (a) with a similar temperature behavior when normalized to R(300K). Note crystals [001] and [110] have a higher Tc_0 ~16.0 K and $T_{c,onset}$ ~16.7 K with RRR=R(300K)/R_{Tc} ~21 while crystal [100] has a lower $T_{c,onset}$ ~15.5

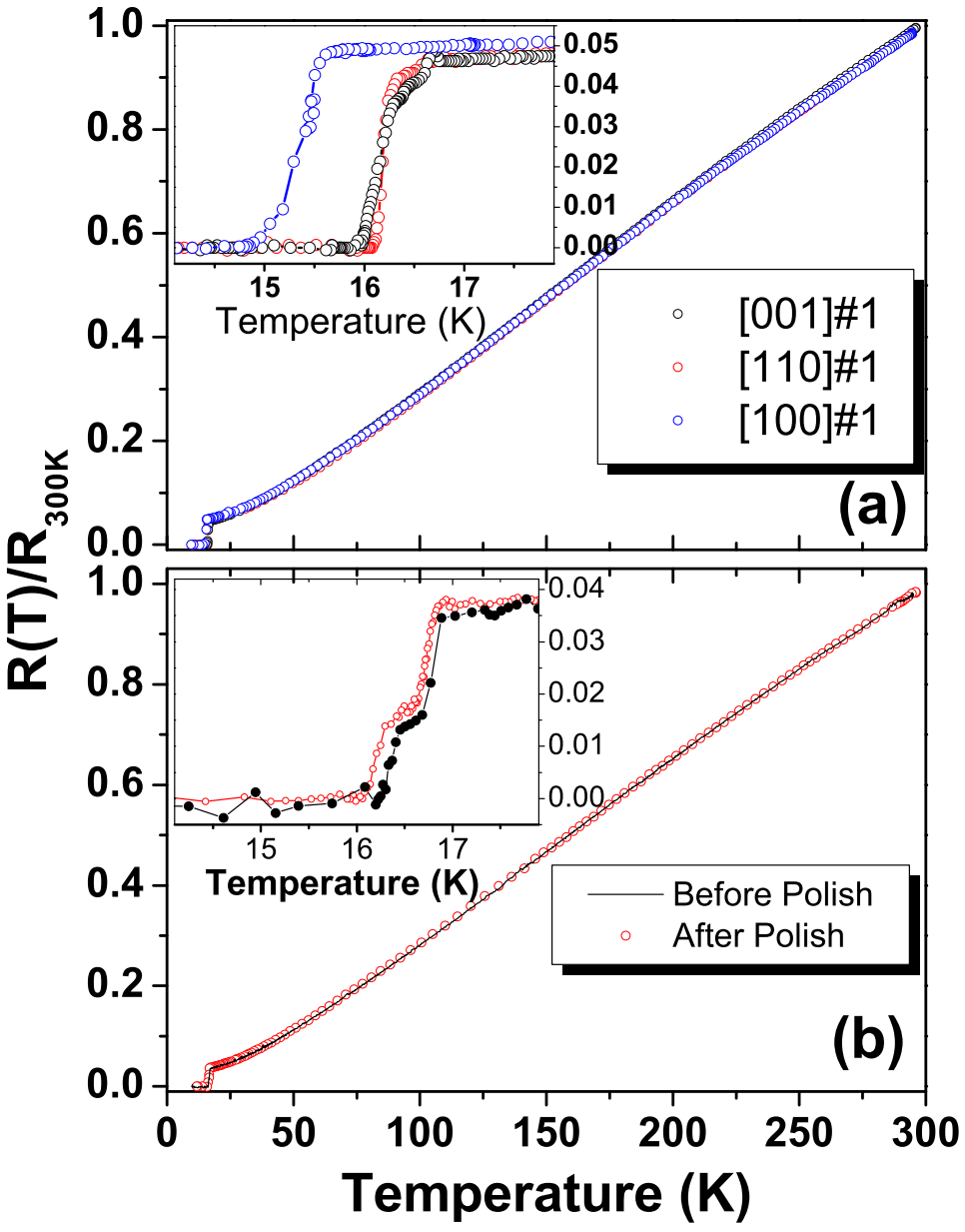

Figure 4.2: Temperature-dependent electrical resistance of $LuNi_2B_2C$ normalized to the value at 300 K for (a) the first set of crystals in the three orientations and (b) the second set coming from the same chunk before and after polishing. Each inset shows the transition details around the superconducting critical tmeperature.

K and Tc_0 ~15.0 K with RRR=20. For the second set, all the samples are prepared from the same big chunk of a larger crystal. Their temperature-dependent resistance is shown in Fig. 4.2(b) with T_{c0}=16.1 K and RRR~26. In order to make sure the polishing does not degrade the crystal quality, the resistances before and after polishing are compared and no measurable change in the temperature behavior and T_c is seen within the resolution.

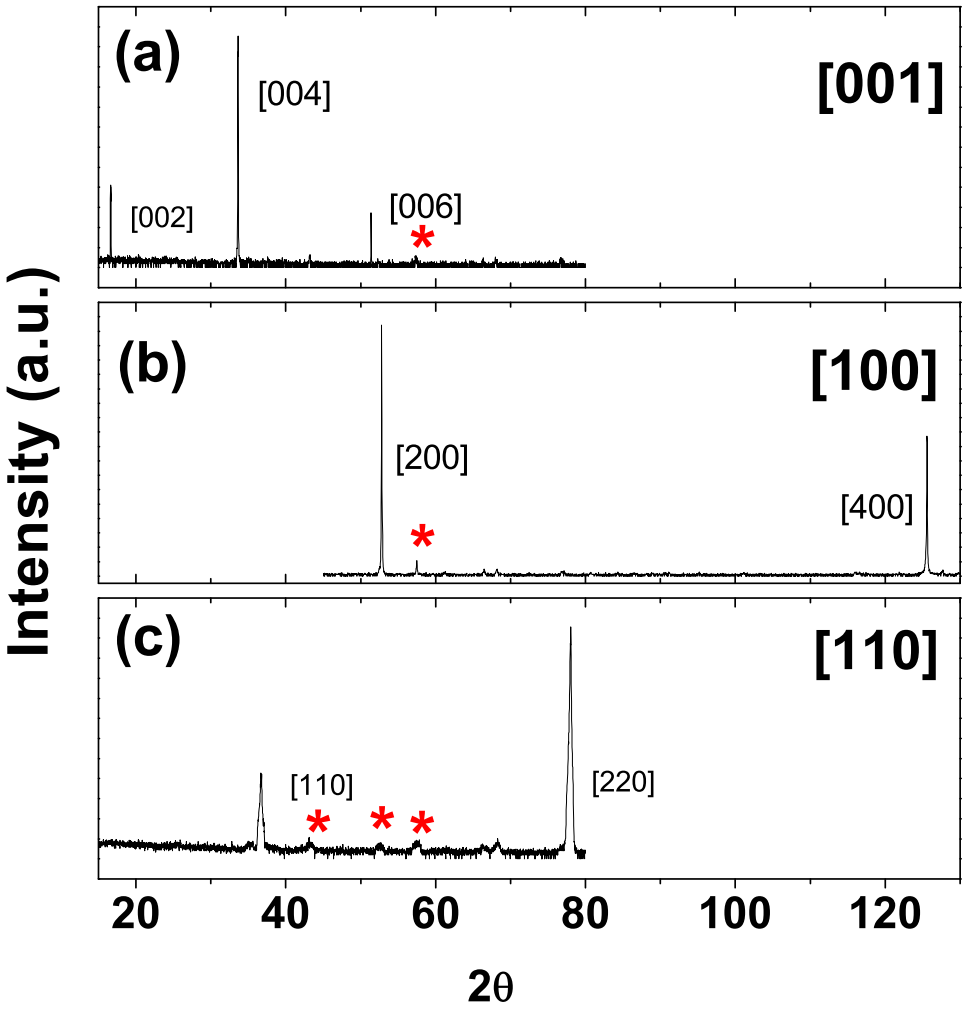

Figure 4.3: X-ray diffraction (XRD) 2θ-ω scans for the prepared crystals with different crystallographic orientations: (a) [001], (b) [100], and (c) [110]. The corresponding angles for the XRD peaks are the same as listed in the reference card, proving the crystals in the desired directions. The small peaks indicated by * are due to stycast.

It is important to confirm that the prepared crystals are in the desired crystallographic orientations for PCARS to probe the gap in the corresponding directions. Their orientations are checked by X-ray diffraction (XRD). XRD spectra are taken on the Phillips X'Pert diffractometer system I or II using a Cu K-α X-ray source with λ=1.54439 Å. The $2\theta - \omega$ scans give the listed Bragg peaks for the assumed directions as shown in Fig. 4.3 due to the constructive interference of reflected X-ray, satisfying $2dsin\theta = n\lambda$ (θ is the angle between the incident x-ray with the surface plane, $\theta = \omega$). The deviation of the surface normal from the major directions is within 5 °.

4.2.2 Surface Treatment and Characterization

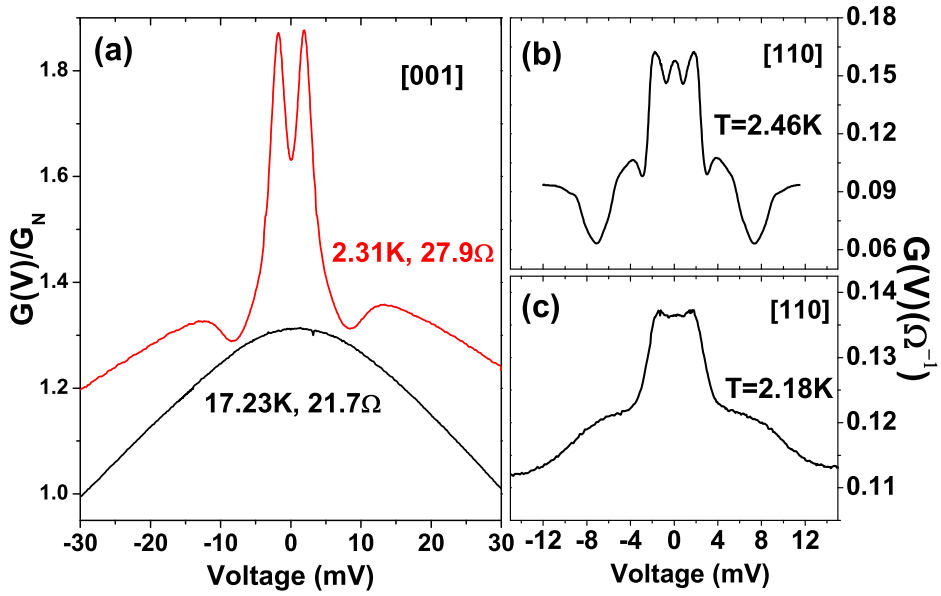

Figure 4.4: Differential conductance curves, G(V) for Au-$LuNi_2B_2C$ point-contact junctions along (a) [001] without surface treatment, (b) and (c) [110] after polishing. In (a), the normalized curves are shifted for clarity.

Without surface treatment, the point-contact data on [001] have a parabolic background with dips outside the gap as shown in Fig. 4.4(a). For the pol-

ished [110] crystals, irregular features are observed as shown in Fig. 4.4 (b) and (c). The samples likely have a degraded surface layer where superconductivity is strongly suppressed due to either a natural oxidation in the air for [001] crystals or mechanical polishing for [110] crystals. We stress again that our technique is quite surface-sensitive. Our reproducibility in observing AR jumped dramatically when we started etching the samples with aqua-regia for about 20 seconds to expose fresh surface before measurement. As shown later, this chemical etching resolves the surface issue in these materials. We note nitric acid etching is not effective at all.

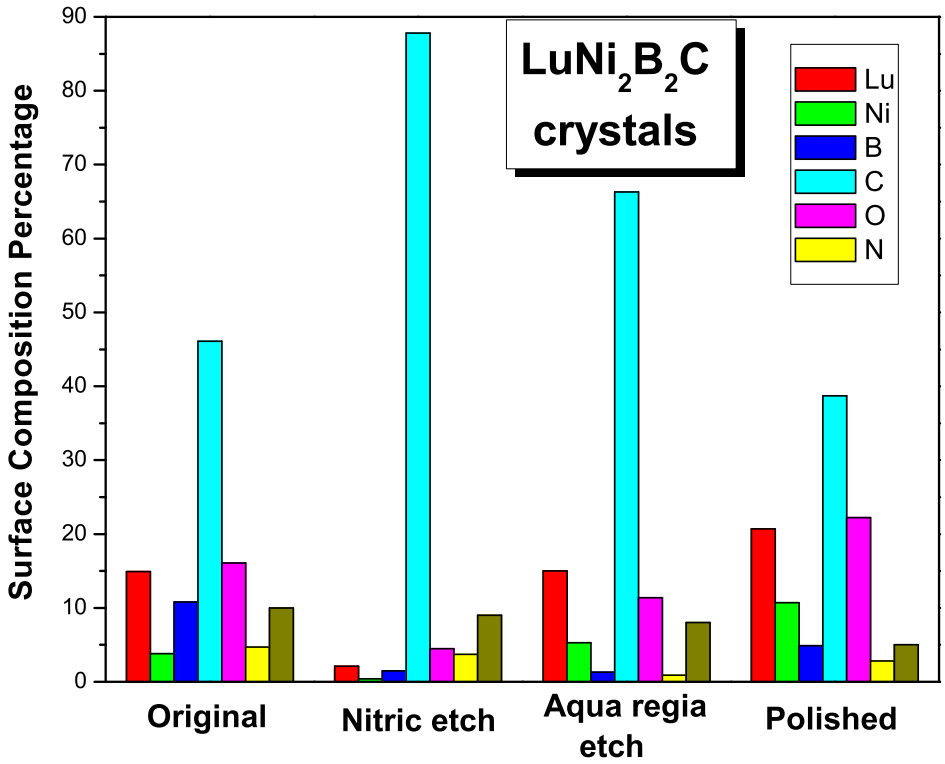

Figure 4.5: Auger electron spectroscopic investigation on the surface element compositions for $LuNi_2B_2C$ cyrstals with different surface preparation methods: pristine(original); nitric acid etch; acqua regia etch; and mechanical polish.

Auger electron spectroscopy, a sensitive technique to study the surface,

is applied to investigate the relationship between the point-contact measurement and sample surface composition either pristine or prepared by different methods, such as nitric acid etching, acqua-regia etching and mechanical polishing. Fig. 4.5 shows the surface composition for $LuNi_2B_2C$ crystals under different conditions: the pristine sample surface show a relative higher percentage of boron, which may come from the nitride boron flux at the surface; the nitric acid only etches away the Lu, Ni and B atoms, leaving Carbon element predominantly on the surface. The samples prepared by acqua-regia etching and mechanical polishing exhibit similar surface compositions from Auger and Andreev reflection signals are probed from PCARS indicating superconducting layer revealed.

4.2.3 Experimental Results and Analysis

After the sample is cooled down to about 2 K in the liquid helium cryostat, a sharp gold tip is moved to engage on the sample surface by a fine differential micrometer with a contact resistance usually around several ohms or tens of ohms, well in the ballistic or Sharvin limit. The differential conductance ($G = dI/dV$) as a function of voltage (V), G(V), is directly recorded by the standard four-probe lock-in technique and we can get a set of conductance curves by changing the temperature from $\sim$ 1.6 K to T_c or the magnetic field usually up to 9 Tesla. The critical temperature at the contact junction, T_c^j, is determined by the temperature dependence of zero-bias conductance, G_0(T), where there is a kink at T_c^j. The measured T_c^j is in good agreement with the bulk T_c determined by four-probe resistance measurement. Therefore, our data really sample the bulk property of $LuNi_2B_2C$, not a degraded surface. For convenience in the future, we simply refer T_c^j as T_c in the following.

Figure 4.6 shows one set of $G(V)$ curves as a function of temperature for

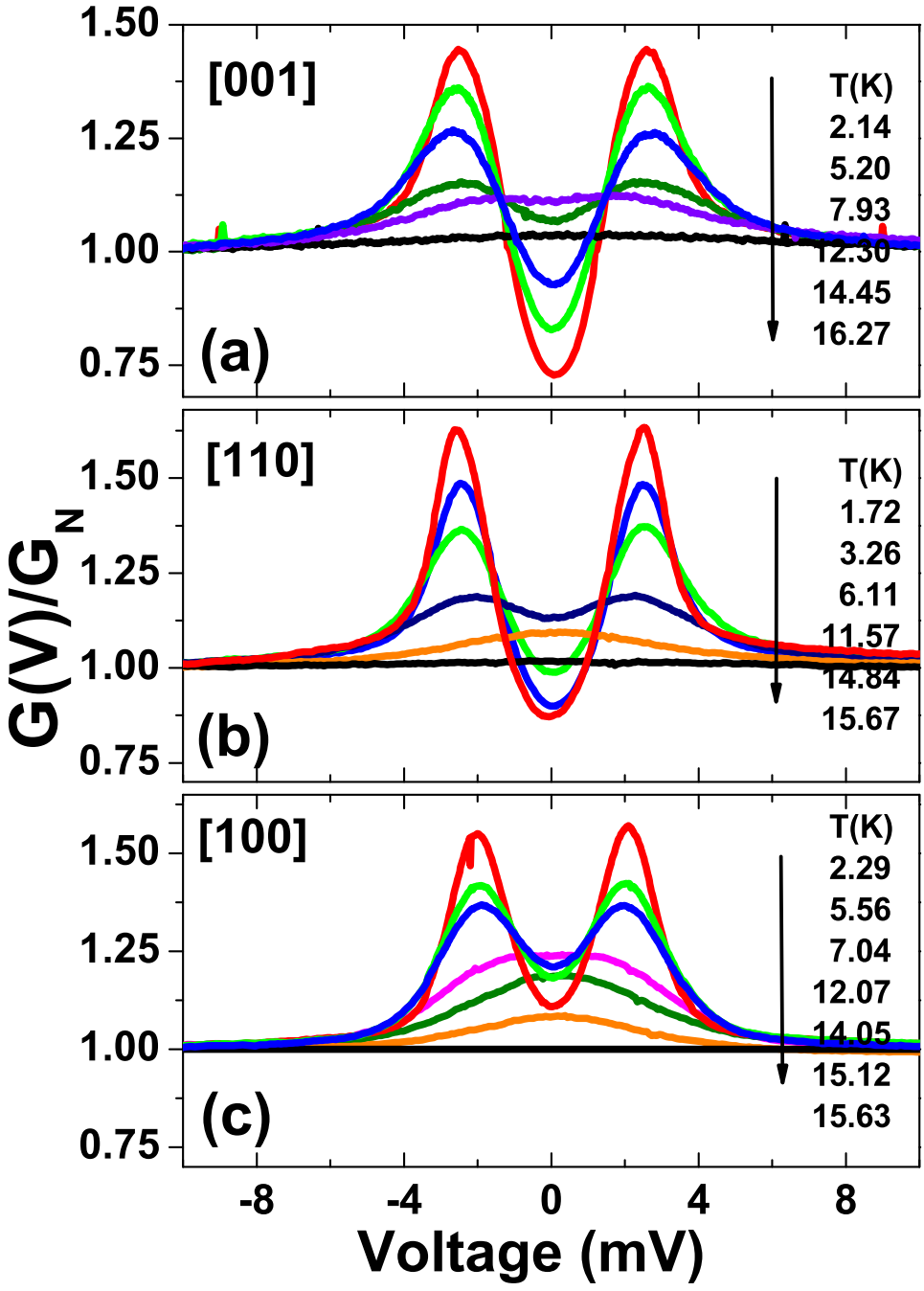

Figure 4.6: Normalized differential conductance spectra of the Au/$LuNi_2B_2C$ point-contact junctions along (a) [001], (b) [110] and (c) [100] directions as a function of temperature. in (c), the data is divided by the conductance curve at the temperature above T_c to get symmetrized.

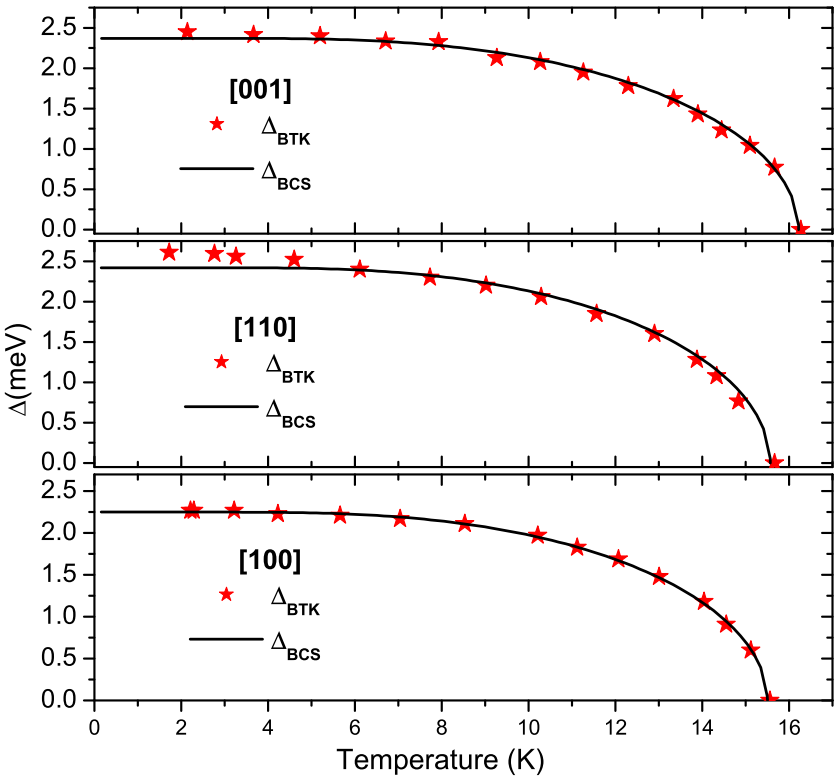

Figure 4.7: Temperature dependence of the superconducting gap extracted from one-gap BTK model in $LuNi_2B_2C$ along (a) [001], (b) [110] and (c) [100] directions in comparison with the standard BCS curve.

[001], [110], and [100] surface orientations. The one-gap Blonder-Tinkham-Klapwijk (BTK) model is used to analyze the data and it gives a good fit to the data.

Figure 4.7 shows the temperature dependence of the superconducting gap, Δ, in the [001], [110], and [100] direction, respectively. As shown, they all follow the standard BCS-like curve, yielding $2\Delta_0/k_BT_c \sim 3.4$, 3.6 and 3.2 in the weak-coupling limit. However, the fits to the gap at low temperatures deviate from the standard BCS model. This behavior has been observed frequently for different runs in all three directions and may be due to the gap anisotropy as discussed later, or a multi-gap nature in $LuNi_2B_2C$ [108]. At our lowest temperatures ($\sim$ 2 K), for the best fit, the data for [001] and [110]

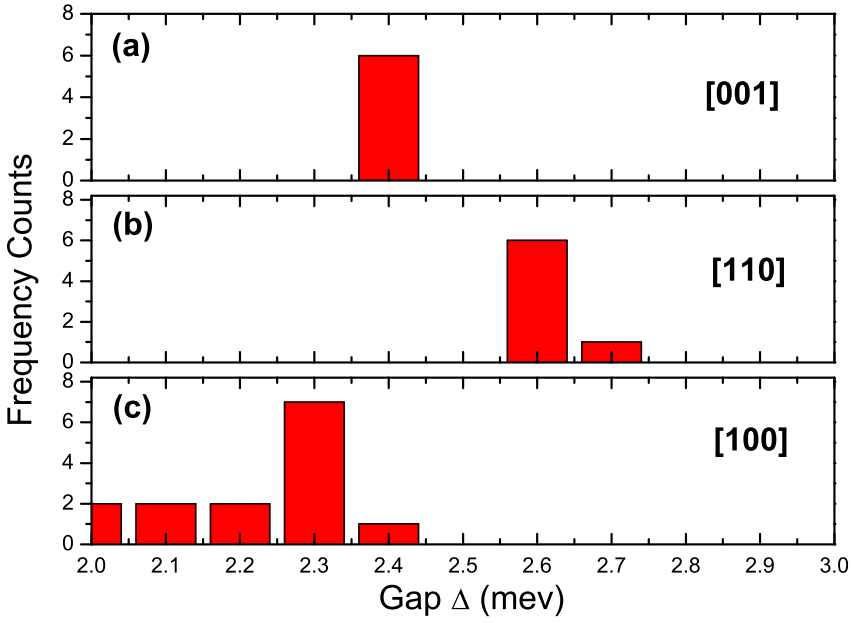

Figure 4.8: Histogram counts for the superconducting gap values extracted from one-gap BTK model measured in (a) [001], (b) [110], and (c) [100] directions.

surfaces show comparable superconducting gaps with $\Delta_{I\|[001]} = 2.4$ meV and $\Delta_{I\|[110]} = 2.6$ meV, consistent with the result by Bobrov *et al.* [108]. The simulated gap size along [100] orientation is ~ 2.3 meV and we see there is not much gap anisotropy. We have tried many contacts with samples in these three orientations and we find our PCARS data are quite reproducible. Fig. 4.8 shows histogram counts for the gap values along these directions at low temperature analyzed by the single-gap BTK model.

Another set of samples from different group are prepared in the same way in order to cross-check the sample dependence. A similar small gap anisotropy is observed, where the gap values along [001], [110], and [100] directions are $\sim$2.5 meV, 2.8 meV, and 2.7 meV, respectively. The temperature dependence of the gap along three directions is shown in Fig. 4.9 and

clearly follow the BCS temperature dependence.

Thus a small gap anisotropy for the three major crystallographic orientations are observed in PCARS for $LuNi_2B_2C$. In order to exclude the possibility that chemical etching during sample preparation yields rough surfaces, which would eliminate the directional effect of injected current and average all the micro-facets in varying directions, we also make PCARS on fresh-polished samples without etching treatment. Similar results are achieved on the freshly polished unetched samples with those after etching.

4.3 PCARS on YNi_2B_2C

YNi_2B_2C is believed to have similar gap structures as $LuNi_2B_2C$. However, we notice that our experimental data on $LuNi_2B_2C$ are quite different from those for YNi_2B_2C in the [100] direction as reported by Mukhopadhyay *et al.* [106], where the G(V) peak position in [100] direction is at a much smaller bias voltage. The [100] gap in $LuNi_2B_2C$ merges with [001] gap at the same bulk Tc rather than disappears at a much lower temperature than T_c. In order to determine if the absence of a small gap in [100] direction for PCARS as observed on $LuNi_2B_2C$ also present on YNi_2B_2C, we prepare another set of YNi_2B_2C single crystals in [001], [110] and [100] orientations, all from a big chunk of crystal. The electrical resistance shows a sharp superconducting transition at $\sim$15.8 K, but with a small tail to 15.5 K, and the RRR is around 25, indicating the good quality of the single crystals.

G(V) curves for the Au-YNi_2B_2C point-contact junctions in the [001], [110] and [100] directions are shown in Fig. 4.11 (a) and (b) and (c), respectively, as a function of temperature. The data are analyzed with the single-gap BTK model and the averaged gap values obtained from dozens of

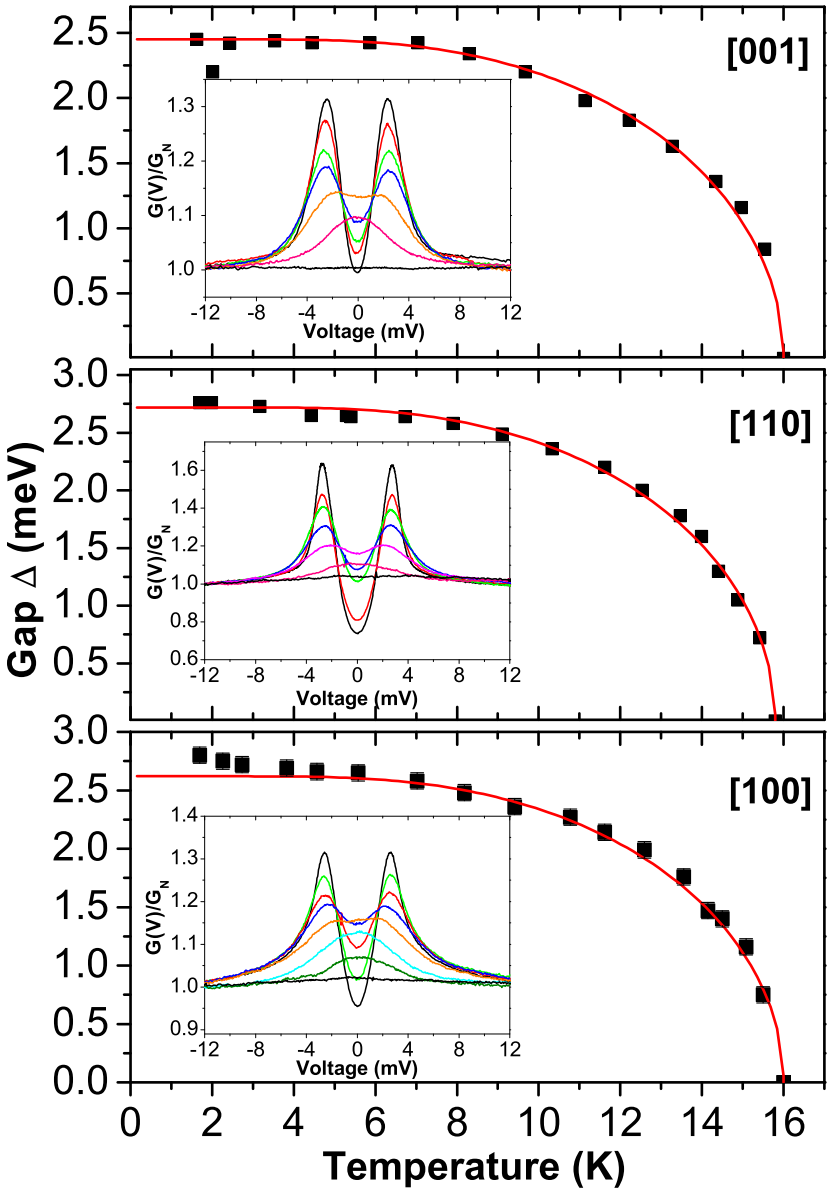

Figure 4.9: Temperature dependence of the superconducting gap extracted from one-gap BTK model in $LuNi_2B_2C$ along (a) [001], (b) [110] and (c) [100] directions in comparison with the standard BCS curve for the second set of samples. The insets are the corresponding point-contact spectra with evolution of temperature.

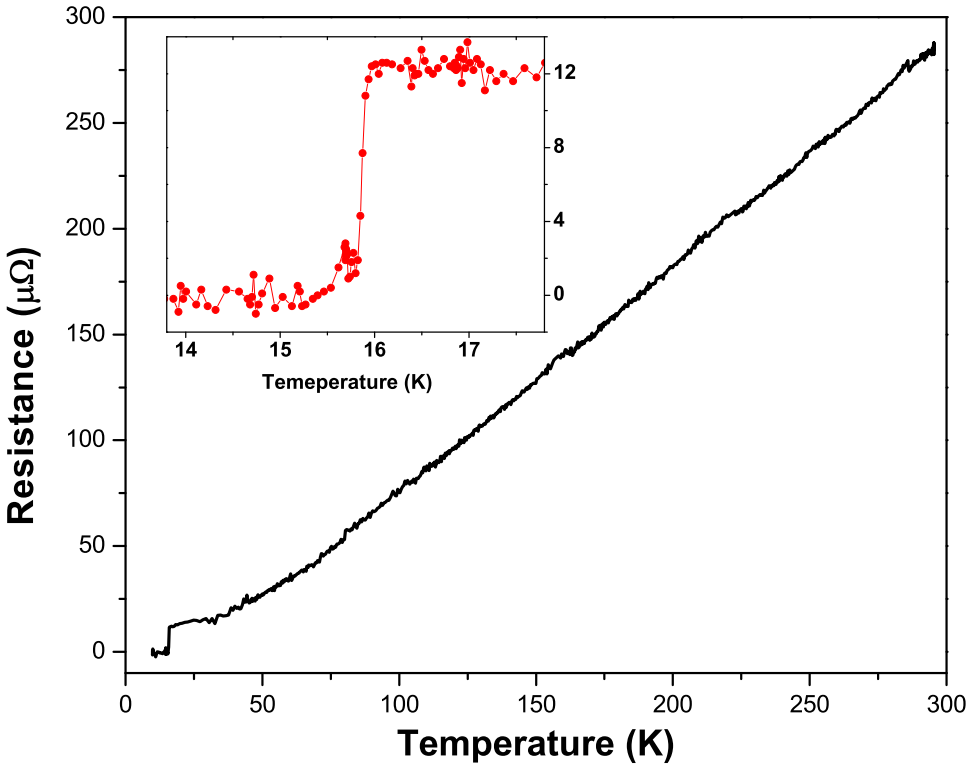

Figure 4.10: Temperature-dependent electrical resistance for the YNi_2B_2C crystals coming from the same chunk. The inset shows the transition details around the superconducting critical temperature.

contacts at low temperature at 2 K are 2.0, 2.1, and 2.5 meV, respectively, for the three major directions. The small gap anisotropy observed here is quite similar to our results on $LuNi_2B_2C$. However, we notice that the gap along [100] is the largest instead among the three major directions for YNi_2B_2C, while it is in [110] orientation for $LuNi_2B_2C$. Fig. 4.12 is the corresponding temperature dependence of the extracted superconducting gaps along different orientations. They all follow the BCS curves with some deviation and this behavior needs more careful analysis.

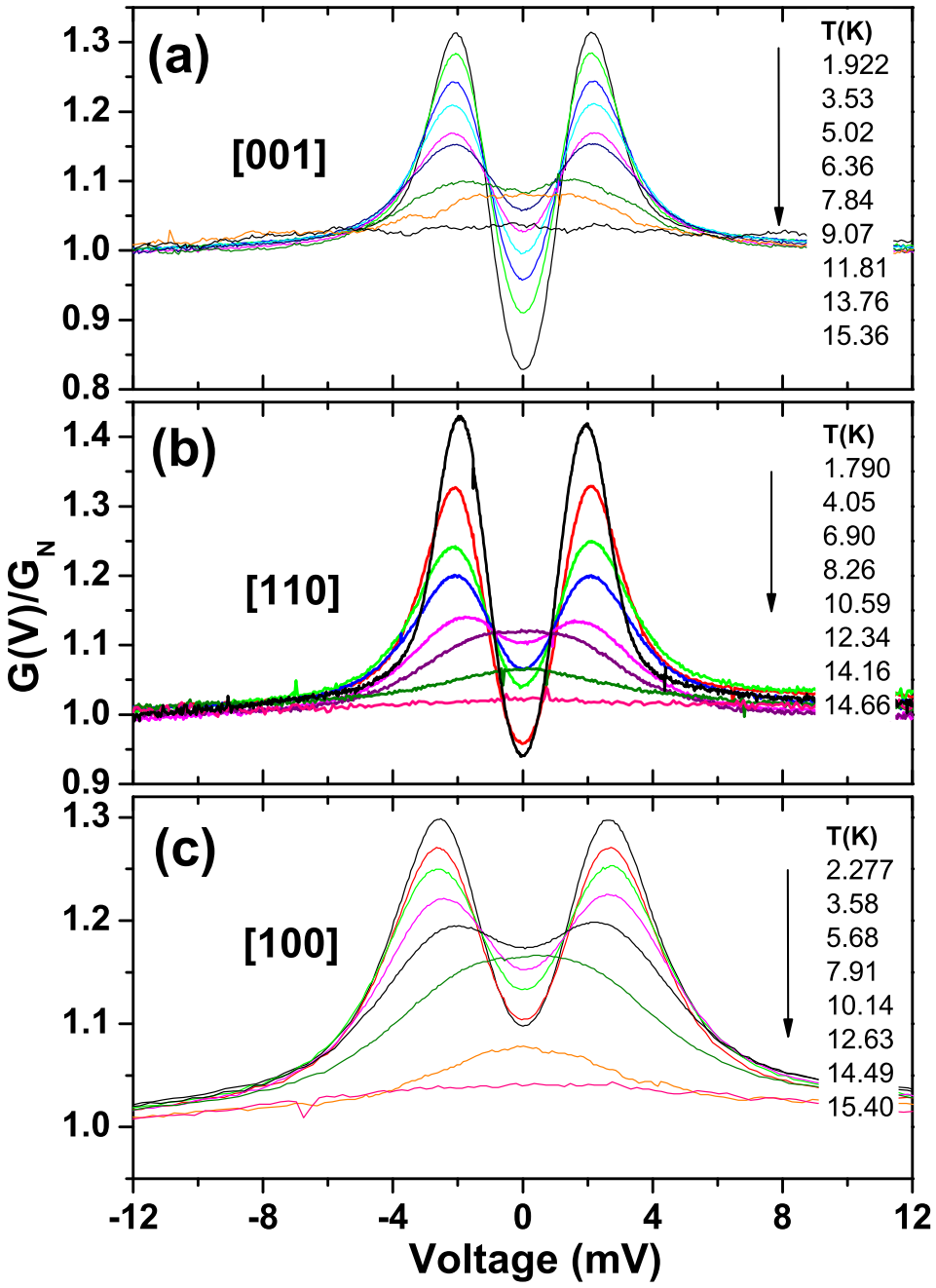

Figure 4.11: Normalized differential conductance spectra of the Au/YNi_2B_2C point-contact junctions along (a) [001], (b) [110] and (c) [100] directions as a function of temperature.

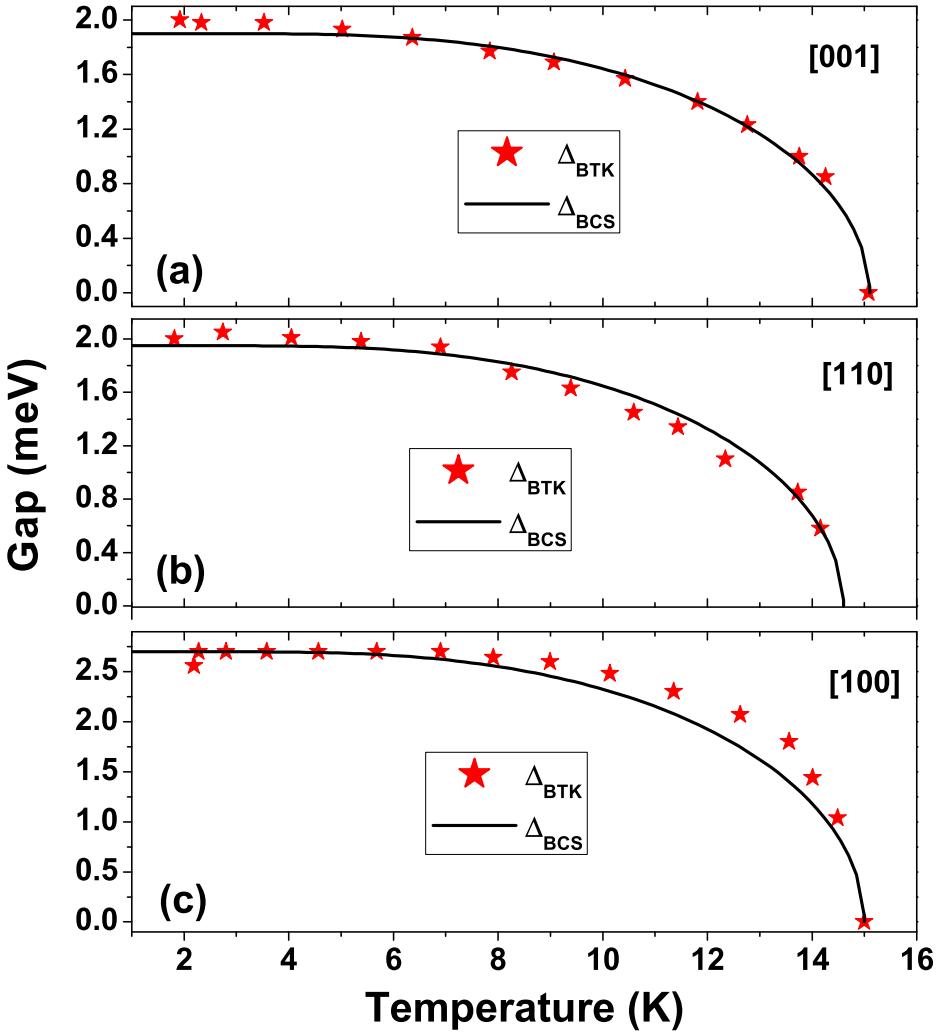

Figure 4.12: Temperature dependence of the superconducting gap extracted from one-gap BTK model in YNi_2B_2C along (a) [001], (b) [110] and (c) [100] directions in comparison with the standard BCS curve.

4.4 Discussions

A small gap anisotropy is observed in the three major crystallographic orientations of $LuNi_2B_2C$ and YNi_2B_2C using nanoscale gold contacts, when our PCARS data are analyzed by single-gap BTK model. This is in contrast with the theoretical predictions of point-nodes in $Y(Lu)Ni_2B_2C$. Fermi surface topology and tunneling cone effect are considered below to explain the

discrepancy in a unified picture. Note thermal conductivity and heat capacity experiments are sensitive to the gap minimum, while PCARS favors to detect the gap maximum and the fine gap structure is usually lost. We would like to consider the Fermi surface topology from band structure calculation and experiments to understand the detailed gap structure. PCARS has a larger tunneling cone for the electrons transporting across the interface: tunneling current not normal to the interface will probe the gap in corresponding directions, and reduce the directional resolution.

A nesting structure on the Fermi surface has been claimed both from band structure calculation and experiments such as ARPES [112], and the electron-positron annihilation technique [113]. It only occupies a small portion of the Fermi surface around the basal plane. According to ref. [104], a point-like gap minimum is expected at the nested Fermi surface points due to AF fluctuation. Ultrahigh-resolution ARPES has revealed a complicated superconducting gap anisotropy in YNi_2B_2C [114]. A sudden decrease and point-like gap minimum ($\sim$ 1.5 meV) is located around X(P)-centered 17th FS sheet along the Γ(Z)-X(P) directions ([110]). They can be connected by the nesting vector $Q \sim 2\pi/a(0.55, 0, 0)$, suggesting the close relationship between the gap minimum and nesting vector. The FS probed by ARPES is off the basal plane with $k_z \sim 0.5$ Γ-Z, which may be the reason why no exact gap nodes are observed in ARPES. Note the gap nodes are in the [100] direction, and they would be probed by directional PCARS in [100]. A sizable SC gap ($\geq$ 2.1 meV) is also reported to open on two walls of an elliptic intersection of 17th FS band parallel to the Γ(Z)-A line ([100]). This large gap would dominate the small nested portions of the FS, masking the gap nodes along [100]. This is consistent with our PCARS measurements in [100] direction where we measure a gap size $\sim$ 2.4 (2.7) meV with a small

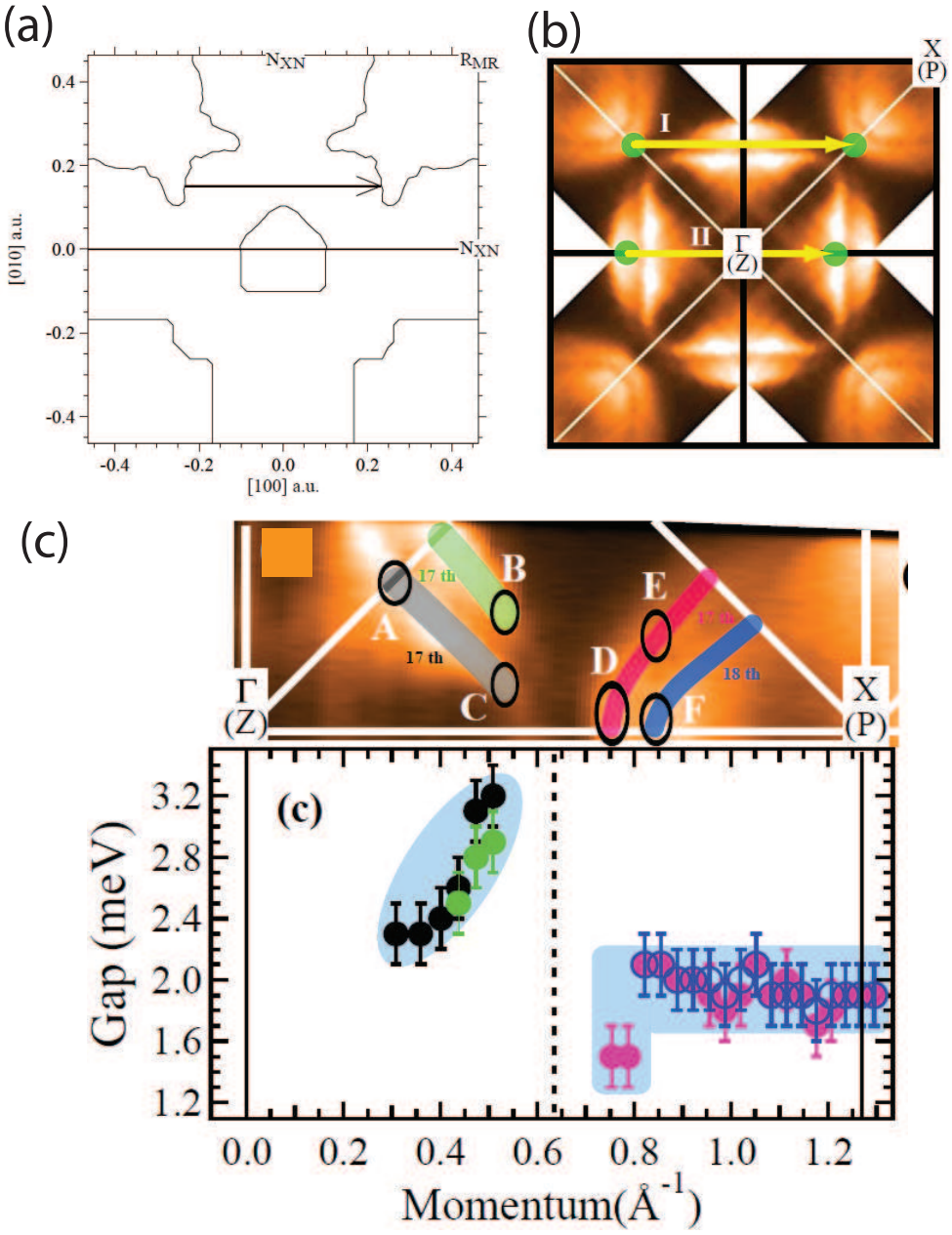

Figure 4.13: (a) The experimental (top) and theoretical (bottom) FS topology of $LuNi_2B_2C$. (Adapted from S. B. Dugdale *et al., Phys. Rev. Lett.* **83** 4824, 1999.). (b) The observed FS from ARPES with symmetrization. Vectors I and II connect the SC gap minima in X(P) centered 17th band and Γ(Z)-centered 17th band, respectively. (Adapted from T. Baba *et al.*, arXiv:0810.0406 (c) The superconducting gap sizes on different FS sheets probed by ARPES. (Adapted from the same source as (b))

gap anisotropy, even if the tunneling cone is taken into account.

The tunneling cone effect is considered when electrons across the interface span a scope of directional angles and therefore probe different gap values in anisotropic superconductors. Compared with a planar tunneling experiment, where the tunneling cone may often be 5 - 10 degrees, PCARS has a much larger tunneling cone due to the small size of the contact. The peak position for the conductance spectra can be simply understood as a weight-averaged gap value. Even if we assume point nodes in the gap structure, they would occupy only a small part of the FS and large gaps would contribute more spectral weight to the conductance and result in a large peak position in [100] direction.

In order to quantitatively show the tunneling cone effect, a first principle calculation of the Andreev-reflection conductance curves is made to compare with the experimental data. Here, we have an SN junction with S = $LuNi_2B_2C$ and N = Au. For $LuNi_2B_2C$ with an anisotropic gap structure, we have to integrate the tunneling current, σ_S, from different incident angles, θ_N, relative to the surface normal. Following Ref. [115], the conductance $\sigma_S(E)$ for a given θ_N can be written as:

$$\sigma_S(E) = \sigma_N \frac{1 + \sigma_N|\Gamma_+|^2 + (\sigma_N - 1)|\Gamma_+\Gamma_-|^2}{|1 + (\sigma_N - 1)\Gamma_+\Gamma_-|^2}$$

where $Z = \frac{Z_0}{cos\theta_N}$, $\sigma_N = \frac{1}{1+Z^2}$, and $\Gamma_\pm = \frac{E-\sqrt{E^2-|\Delta_\pm|^2}}{|\Delta_\pm|}$. Here, Z_0 is the intrinsic barrier strength and $\Delta_\pm$ represent the pairing potentials felt by the transmitted electron-like quasiparticles (ELQ), and hole-like quasiparticles (HLQ), respectively. Thus, for the NS junction, the total conductance,

$\sigma_T(E)$, is the integration of $\sigma_S(E)$ over a solid angle:

$$\sigma_T(E) = \frac{\int d\omega \sigma_S(E) cos\theta_N P(\theta_N)}{\int d\omega \sigma_N cos\theta_N P(\theta_N)},$$

where the parameter Θ_D is used to characterize the tunneling cone for the injected electrons and $P(\theta_N)$ is the electron transmission probability along θ_N. We assume $P(\theta_N) \propto e^{-(\frac{\theta_N}{\Theta_D})^2}$.

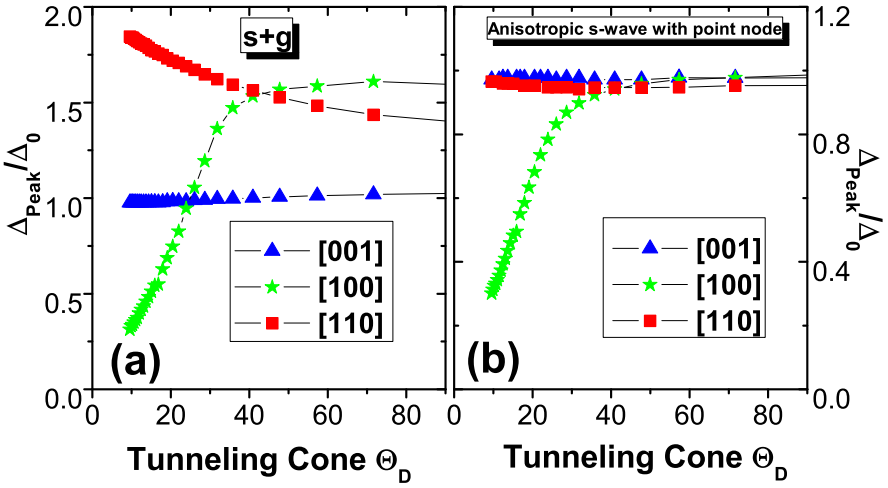

Figure 4.14: Calculated peak position Δ_{Peak}/Δ_0 for the conductance curves as a function of the tunneling cone Θ_D for different surface orientations at a low temperature. The assumed gap structures are (a) s+g pairing symmetry and (b) anisotropic s-wave gap with point-nodes.

We calculate the conductance spectra based on two gap structure models: s+g pairing symmetry and anisotropic s-wave gap both with point-nodes. The proposed s+g gap [101], $\Delta(k) = \Delta_0[1 - sin^4\theta cos(4\phi)]$, requires Δ_{110} to be two times Δ_{001}, while for anisotropic s-wave, for simplicity, we assume $\Delta(k) = \Delta_0[1 - sin^4\theta cos^2(2\phi)]$. The peak positions, Δ, for the conductance spectra along three major directions are calculated for a range of values of the tunneling cone Θ_D. Fig. 4.14 (a) and (b) are the calculated peak positions as a function of the tunneling cone Θ_D size for s+g and anisotropic s-wave

gap structure, respectively. We assume the tunneling cone Θ_D remains the same for different surface orientations: we find the anisotropic s-wave gap with a tunneling cone $\Theta_D \geq 30^o$ is in better agreement with our PCARS experimental results than the s+g pairing symmetry at the same θ_D. The feature of point-nodes in [100] would be masked by the large gaps in other directions due to the large tunneling cone.

In conclusion, our PCARS data show a small gap anisotropy for [001], [110], and [100] crystallographic orientations. Absence of point nodes for PCARS in [100] direction is explained by assuming a sizable SC gap ($\geq$ 2.1 meV) opens on other FS sheets of the 17th band as reported in ARPES experiments. The large tunneling cone Θ_D at the interface for PCARS also prevents the observation of any point nodes. If we consider an anisotropic s-wave with point nodes gap structure in $LuNi_2B_2C$ rather than s+g pairing symmetry, the calculated conductance curves are consistent with our experimental data, assuming $\Theta_D \geq 30^o$. We note that impurity scattering may open a gap on the original nodal points and reduce the gap anisotropy in good agreement with theoretical calculations for s+g gap structure [116]. Planar tunneling spectroscopy, with its higher resolution in k-space and sensitivity to the quasiparticle DoS would help us to achieve more conclusive results. Efforts to make planar junctions in the borocarbides are in progress.

Chapter 5

PCARS studies on Iron-based Superconductors

5.1 Introduction

The recently-discovered iron-based superconductors [117] have emerged as a whole new family of high temperature superconductors, which are complimentary to the study of cuprates. They have attracted intensive study in the community focusing on their physical properties and potential applications. The discovery of these superconductors is of interest itself: based on the LaCuSO structure, H. Hosono *et al.* discover superconducting LaFePO with $T_c \sim 4$ K (later increased to 7 K). With F doping into the O position, the T_c increases to ~ 6 K [118]. In February 2008, The same group found a dramatically increased T_c in $LaFeAsO_{1-x}F_x$ to about 26 K [117]. Soon after this report, Chinese groups in Institute of Physics, Beijing, boosted up the T_c as high as 55 K either with Fluorine doping or oxygen deficiency for other rare earth Ln compounds (Ln=La, Ce, Nd, Sm...) [119, 120, 121, 122]. All these materials can be categorized into Fe-1111 type. Inspired by these works, D. Johrentdt in Germany resumed his work from the 1980s on $BaFe_2As_2$ and found superconductivity in the 40% potassium-doped $BaFe_2As_2$ with $T_c \sim$ 38 K [123]. This class is generally refered as the Fe-122 type. Large single crystals of iron-based superconductors are now availabe which greatly accelerates the expreimental research on these new superconductors. Other types of iron-based superconductors are also developed, such as LiFeAs (Fe-

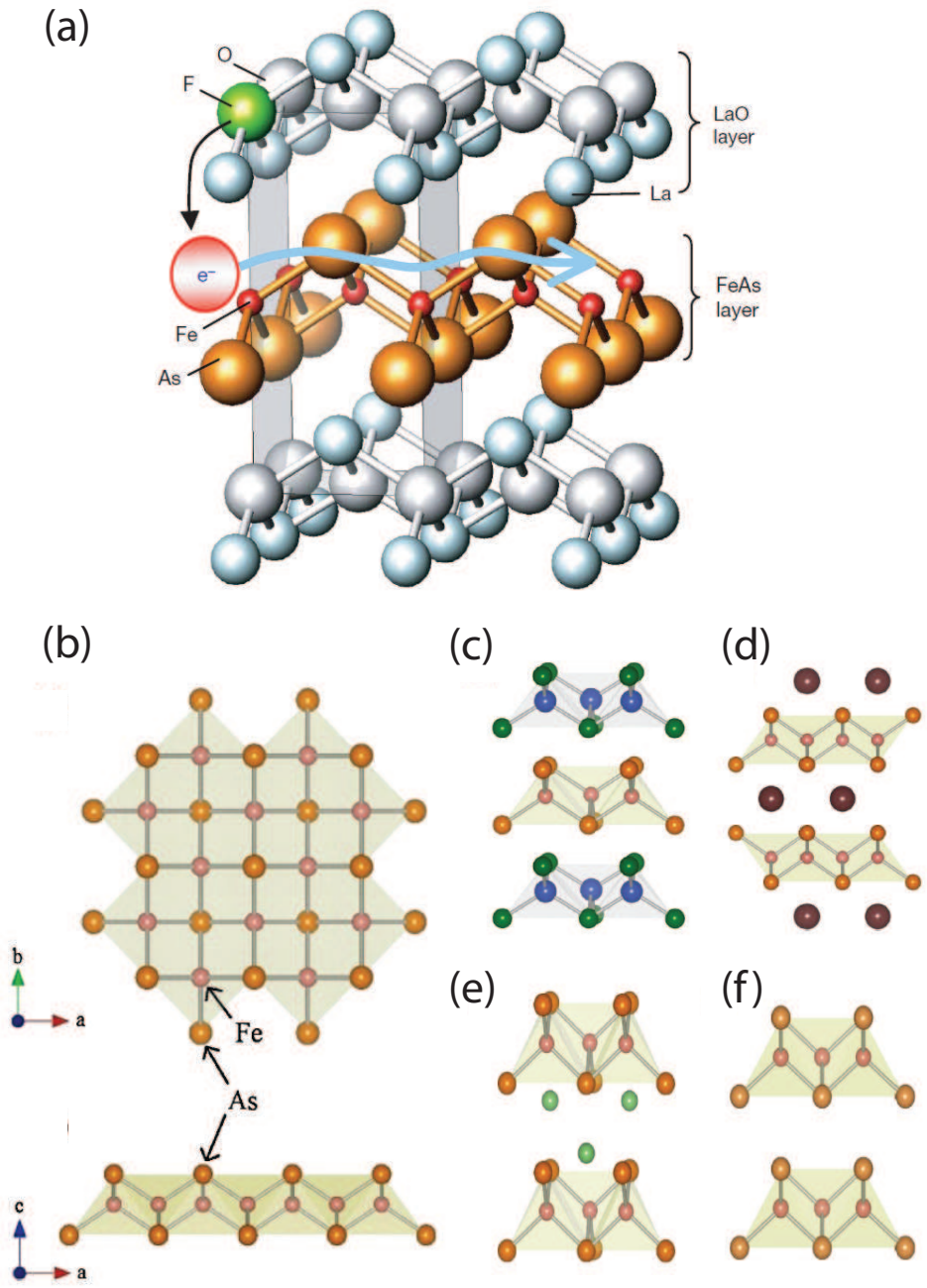

Figure 5.1: (a) Schematic crystal structure of LaFeAsOF. (Adapted from H. Takahashi *et al*, Nature **453**, 376, 2008) (b) the common Fe-As corrugated layer of all iron-based superconductors in different crystals: (c) Fe-1111 (d) Fe-122 (e) Fe-111 (f) Fe-11. (Adapted from K. Ishida *et al*, J. Phys. Soc. Jpn **78**, 062001, 2009)

111) [124], and $Fe_{1+y}Se_{1-x}Te_x$ (Fe-11)[125] but so far, the T_c has never been higher than 55 K. They form a new and rich family of high T_c superconductors after two decades of dominance by cuprates, which inspires researchers to investigate their common and unique features to unveil the mystery of high T_c.

The crystal structure of $LaFeAsO_{1-x}F_x$ is shown in Fig. 5.1 (a) with its alternating layers of $(LaO)^{+1}$ and $(FeAs)^{-1}$ along the c axis. The corrugated FeAs plane, as shown in Fig. 5.1(b), is similar to the CuO_2 plane of cuprates. When replacing some oxygen atoms with fluorine, the extra electrons flow in the FeAs conducting layers and the in-plane conductance is larger than in the perpendicular direction. However, the resistivity anisotropy is much smaller than the cuprates and the electronic properties are not 2-dimensional or quasi 2-D as in the case of cuprates. For the superconducting $(Ba_{0.6}K_{0.4})Fe_2As_2$ single crystals, the critical magnetic field is found to be even more isotropic [126] than the Fe-1111 system, since $(Ba_{0.6}K_{0.4})Fe_2As_2$ does not have the insulating LaO layers. The FeAs layer is commonly observed in distinct iron-base superconducting systems as in Fig. 5.1 (c), (d), (e) and (f).

From band structure calculations, the density of states near the Fermi surface comes almost entirely from the d states of the Fe atoms as shown in Fig. 5.2 (a), even with some hybridization of p states in As. One thing in common between the Fe-based and cuprate superconductor is the existence of an active plane. The FeAs and CuO_2 planes in the Fe-based and cuprate superconductor, respectively, clearly play an important role in the normal-state and superconducting properties. The Fermi surface band structures of these two classes of superconductors are quite different: cuprates at least exhibit a dominating majority band, while the iron-based superconductors have several disconnected electron and hole bands on the Fermi surface, which

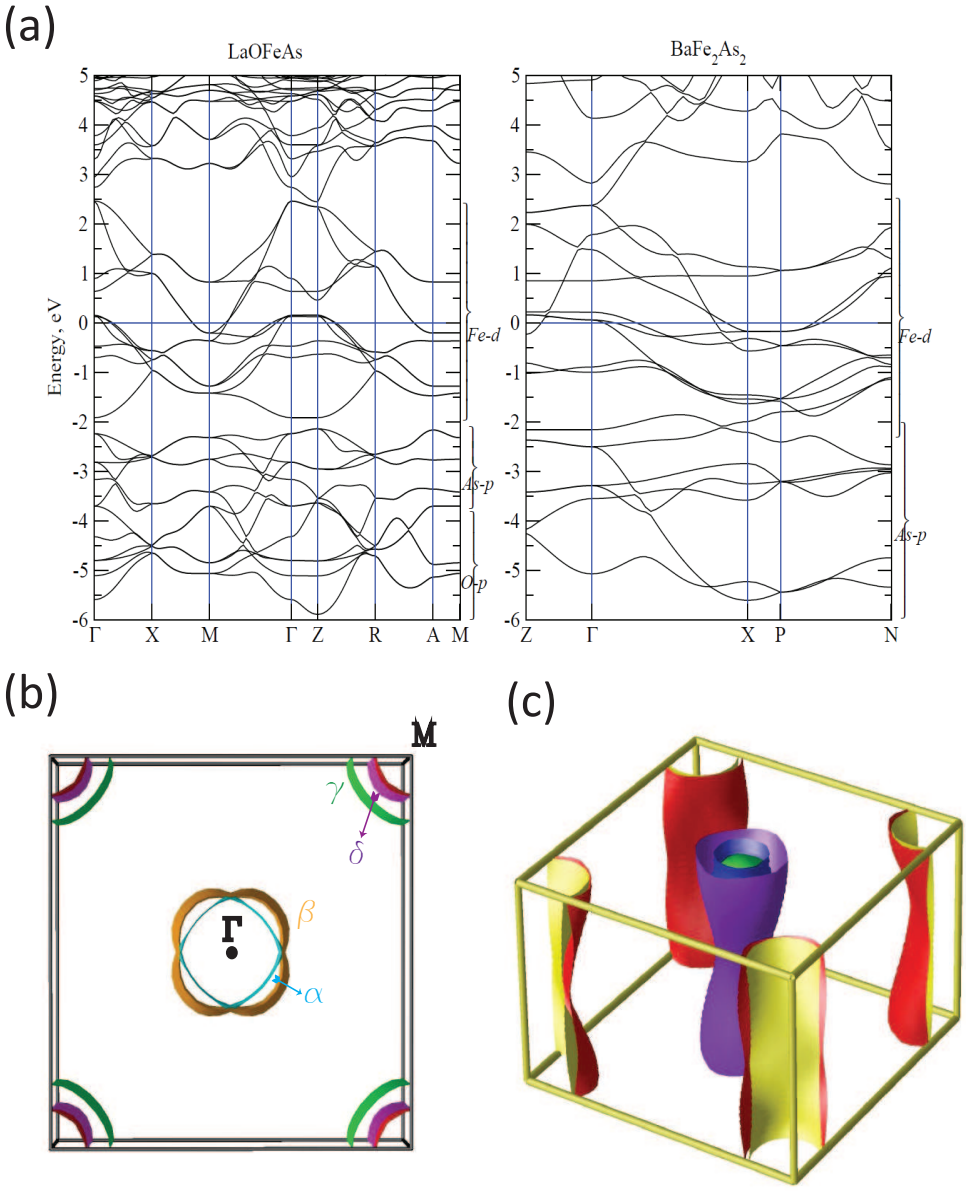

Figure 5.2: (a) Band structure calculation for LaFeAsO and $BaFe_2As_2$. (Adapted from I. A. Nekrasov *et al*, JETP Lett. **88**, 144, 2008) (b) the Fermi Surface sheets for 10% e-doping LaAsFeO from a topview of the Brillouin zone with Γ as the zone center and **M** the zone edge. (c) The Fermi Surface of the 10% Co-doping $BaFe_2As_2$ in the 3D Brillouin zone. (Adapted from I. I. Mazin and J. Schmalian, Phys. C **469**, 614, 2009)

arise from several d orbital sates of Fe in the unit cell. ARPES and quantum oscillation measurements have observed two or more hole-like Fermi surfaces (α,β) near the Brillouin center Γ [k=(0,0)], and two electron-like surfaces (γ, δ) near the M point [k=(π, π)] as shown in Fig. 5.2 (b) for $LaFeAsO_{0.9}F_{0.1}$. Hole or electron doping would shift the Fermi energy and change the relative volume between hole and electron bands, causing some differences in the FS [136, 137, 138, 139, 140].

An antiferromagnetic (AFM) phase is observed in the non-superconducting parent compounds of this family where the spins align in opposite directions for the nearest iron atoms below the Neel temperature T_N [127]. For the Fe-1111 system, a structural transition occurs at a higher temperature than the magnetic transition [127], while, for the Fe-122 system, both the structural and AFM transitions occur at the same temperature [128]. The local or itinerant nature of the AFM order is still under debate: In the local spin perspective, the magnetic interaction is described by the general Heisenberg model with parameters J1, J2 [129]; and in the itinerant picture, an SDW order develops due to the nested Fermi surface between the itinerant electrons on α and γ bands [130, 131]. Unlike the cuprates, the AFM state is metallic indicating a moderate electron Coulomb interaction without localization. Reminiscent of cuprates, the AFM order is suppressed with chemical doping or pressure, and superconductivity emerges as a new ground state for the system. The coexistence of superconductivity and long range magnetic order depends on the specific materials and the existence of such coexistence remains controversial [132, 133, 128, 134].

A first step in unveiling the underlying superconducting mechanism is to determine the paring symmetry in the iron-based superconducting family. I. Mazin proposed that superconductivity in iron pnictides may originate

from AFM fluctuations and an extended s-wave gap structure with a sign reversal ($s\pm$) on different FSs is favored [135]. In this model, the hole-like and electron-like bands are fully-gapped and have a π phase shift in the superconducting state. A fully-gapped state has been confirmed by different experimental techniques such as ARPES [136, 137, 138, 139], penetration depth [141], μSR [142, 143], Hc_1 [144] and specific heat measurements [145]. The Hebel-Slichter coherent peak is absent in NMR measurements [149, 150] and it is argued that is a natural consequence of the extended $s\pm$ model in the superconducting state [151]. However, a universal power law rather than exponential behavior is observed in the London penetration depth measurement for $RFeAsO_{0.9}F_{0.1}$ (R=Nd, La) [146], and $Ba(Fe_{1-x}Co_x)_2As_2$ at various doping levels [147, 148]. There is no phase-sensitive measurement such as Josephson interferometry up to now to prove the sign change among different bands. However, an indirect evidence for the possible $S_\pm$ gap symmetry is from inelastic neutron scattering data for $(Ba_{0.6}K_{0.4})Fe_2As_2$, where a spin resonance in the superconducting state is observed with a resonant excitation energy Ω_0=14 meV and $\Omega_0/2\Delta \sim 0.58$ [153].

Shortly after the discovery of the superconducting LnFeAsO (Fe-1111) family, some PCARS measurements have been carried out, but the results are not yet conclusive, partly due to the polycrystalline nature of the samples. Chen *et al.* report a conventional BCS-like superconducting gap with $2\Delta_0/k_BT_c \sim 3.7$ for $SmFeAsO_{0.85}F_{0.15}$ [154], while multiple gaps are claimed by other groups with different detailed structures in the initial stage [155, 156, 157, 158, 159]. Among those who claim multiple gaps, some merging agreements are being reached where $2\Delta_1/k_BT_c$ ~2-3 and $2\Delta_2/k_BT_c$ ~7-9. We apply PCARS to different AFe_2As_2-type superconducting single crystals to elucidate their gap structure and OP symmetry [160].

5.2 PCARS on (Ba,K)Fe_2As_2

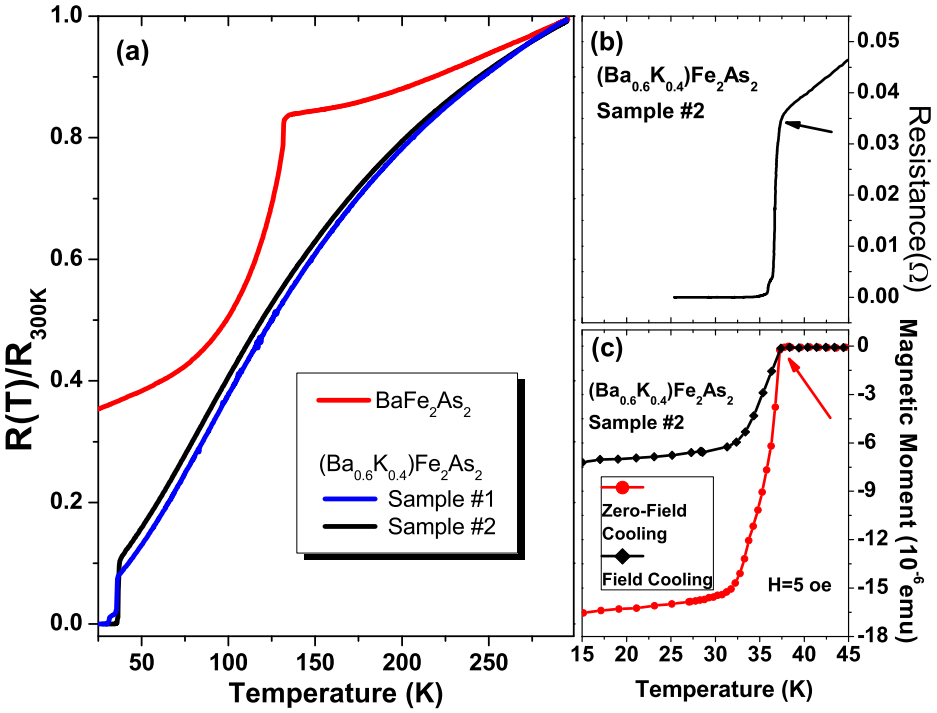

Figure 5.3: (a) Four-contact resistance measurement for $(Ba_{0.6}K_{0.4})Fe_2As_2$ crystals #1 (blue) and #2 (black) in comparison with the parent compound $BaFe_2As_2$ crystal (red); temperature-dependent (b) resistance and (c) magnetic moment for $(Ba_{0.6}K_{0.4})Fe_2As_2$ crystal #2. The superconducting transition is indicated by arrows. The magnetic field is 5 oe for both field and zero-field cooling in (c).

Hole-doped $(Ba_{0.6}K_{0.4})Fe_2As_2$ ($T_c \sim 37$ K) single crystals are grown out of FeAs flux by a high temperature solution method as described in [161]. Point-contact measurements have been performed on two single crystals labeled as #1 and #2. They both show a superconducting onset temperature of ∼37 K in the four-contact resistance measurement as shown in Fig. 5.3 (a). The RRR ($R_{300K}/R_{Tc-onset}$) is $\sim 9-10$, which indicates a reasonable quality of single crystal especially in this initial stage after the discovery of this superconductor. Crystal #2 has a higher Tc_{zero} ∼36.0 K while the crystal #1 has a long tail down to 30.6 K, likely due to inhomogeneities. A double-

transition is observed in crystal #1 at 36.0 K and 30.8 K, with the major resistance drop at 36.0 K. This may indicate a dominant contribution of grains with $T_c = 36.0$ K in this crystal. The temperature-dependent magnetic moment in Fig.5.3(c) in H=5 Oe shows a superconducting transition with Tc_{onset}=37 K for both zero-field and field cooling of crystal #2 with the magnetic property measurement system (MPMS).

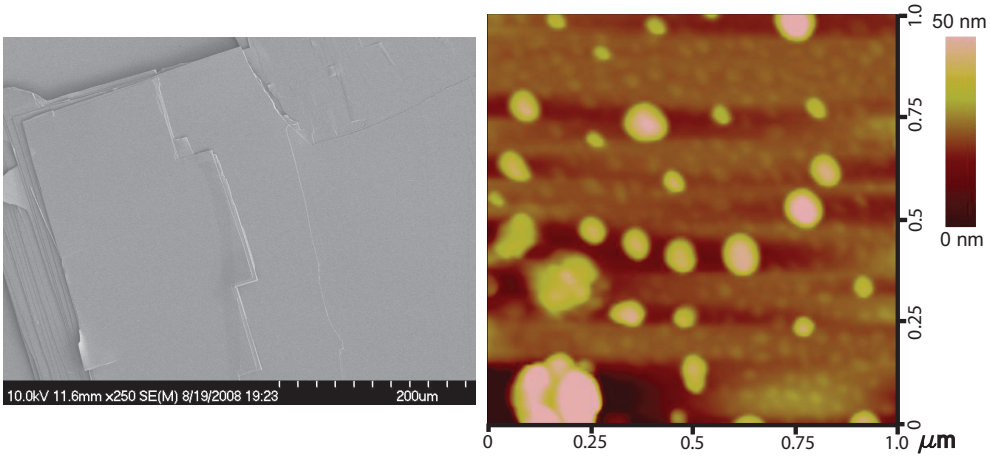

Figure 5.4: (Left) SEM (Right) AFM images on cleaved (Ba,K)Fe_2As_2 surface.

The crystals are plate-like with natural c-axis facets and cleavable simply with scotch tape to expose fresh and shiny surfaces. For PCARS, the crystals are fixed on stycast epoxy for easier handling and electrical insulation. After cleavage, the crystals usually have terrace-like steps on the surface with a scale of few hundreds microns from the SEM image as shown in Fig. 5.4(a). The flat area is large enough compared with the tip size, and it is not difficult to aim the contact to touch the flat region. However, from AFM measurement, as shown in Fig.5.4(b), the surface is not smooth to a micron scale, and a few small "mountains" are scattered around with an averaged mean roughness of around 6 Å.

For point-contacts on (Ba,K)Fe_2As_2 crystals, representatives of the most

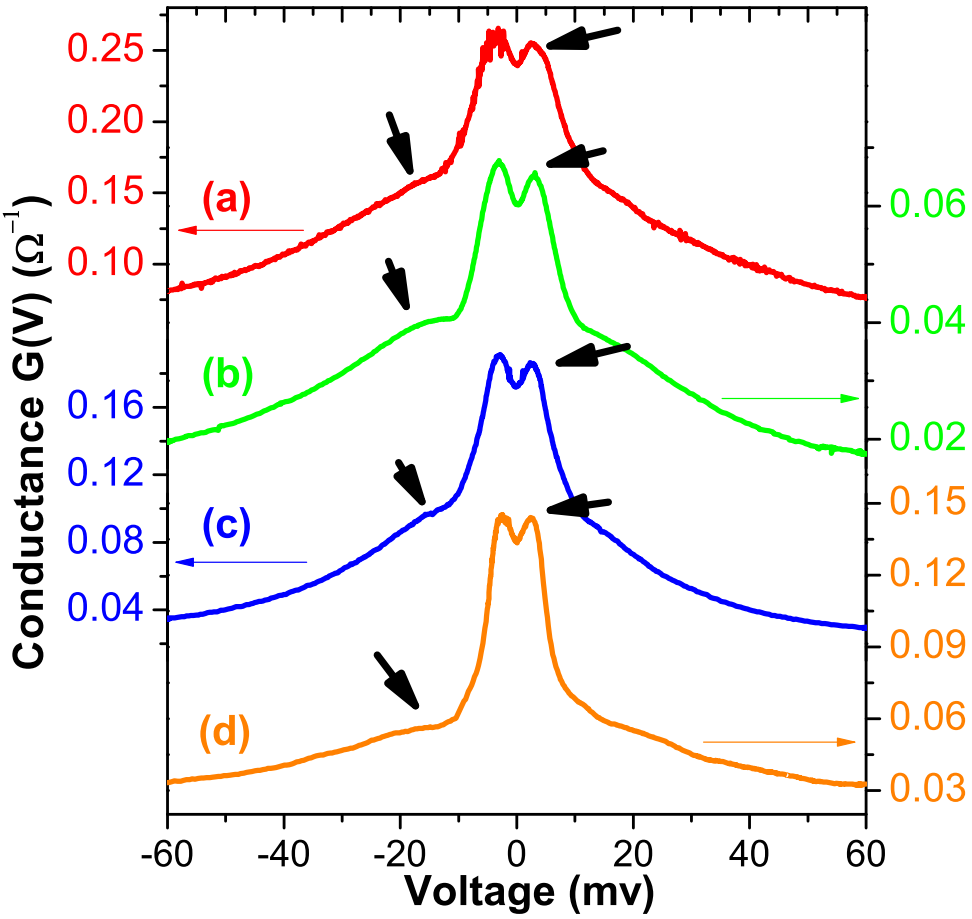

Figure 5.5: Differential conductance spectra G(V) for the $Au/(Ba_{0.6}K_{0.4})Fe_2As_2$ point-contact junctions at low temperatures T∼2 K. The peak and hump structures are indicated by arrows nearby.

frequently observed G(V) curves at low temperatures (∼2 K) are shown in Fig. 5.5 for different contacts. The prominent features are the two peaks at ∼ ±3 meV and a strongly sloping background. A hump structure can also be noticed around ±15 meV as indicated by arrows, and a small conductance asymmetry is systematically observed. Similar broad backgrounds and asymmetries are reported in the recent point-contact measurement on $SmFeAsO_{0.8}F_{0.2}$, where the sloping background is claimed to disappear around the Neel temperature (∼ 140 K) of the parent compound [159]. The temperature dependence as shown in Fig. 5.6(a) verifies that the

low-bias conductance enhancement is due to Andreev reflection. Although the junction resistance changes with temperature, the Andreev reflection signal disappears only above the bulk T_c, giving confidence that we probe the bulk gap. The sloping background survives above T_c so it does not originate from superconductivity and must be due to some other scattering mechanism.

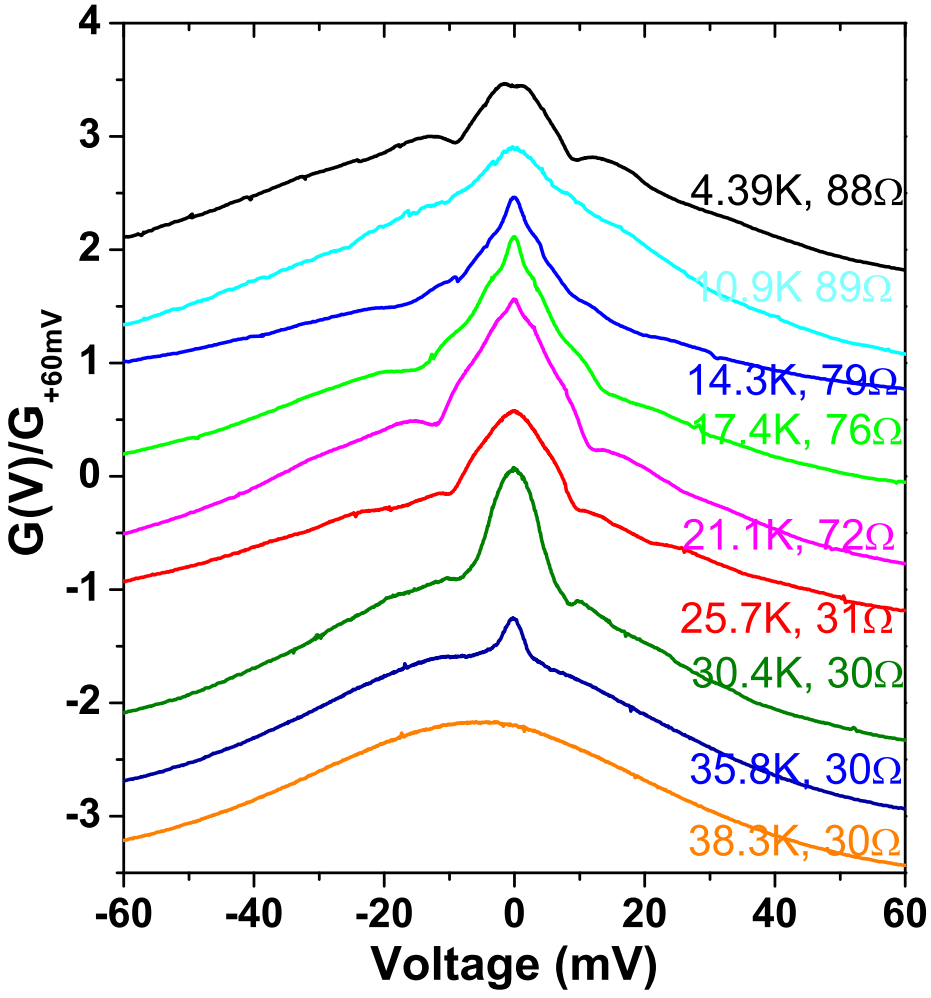

Figure 5.6: Temperature dependence of the conductance curves G(V) for a Au/(Ba,K)Fe_2As_2 point-contact junction on a freshly-cleaved surface (the junction resistance changes with temperature due to instability of the contact). The curves are vertically shifted for clarity.

Since the (Ba,K)Fe_2As_2 material is known to be reactive in air, we try to minimize exposure time between cleavage and cooldown. The usual time is

about 30 minutes. We investigate the effect of a 1 week air exposure as shown in Fig. 5.6(b). The Andreev reflection signal is lost below 16.6 K, lower than that of the bulk. This indicates the air exposure degrades the surface and suppresses the superconductivity. We note the sloping background does not change with the air exposure.

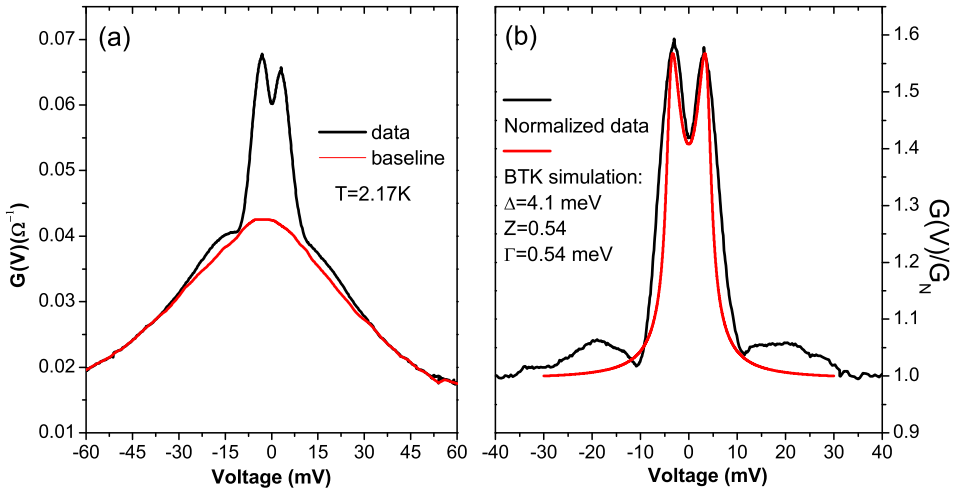

Figure 5.7: (a) A typical G(V) curve for the Au/(Ba,K)Fe_2As_2 point-contact junction and the extrapolated background baseline; (b) The normalized conductance data and best BTK fitting curve.

For the gap analysis, we normalize the conductance to the extrapolated baseline as shown in Fig. 5.7(a). The normalized data are then analyzed by the single-gap Blonder-Tinkham-Klapwijk (BTK) model. The best fit for the energy gap is $\sim 3.0-4.0$ meV, so $2\Delta_0/k_BT_c \sim 2.0-2.6$, smaller than the BCS weak coupling ratio of 3.52. This value is comparable with the smaller gap size probed by PCARS on polycrystalline samples of $LaFeAsO_{1-x}F_x$ [156], $NdFeAsO_{0.9}F_{0.1}$ [157], and $SmFeAsO_{0.8}F_{0.2}$ [159].

We stress that our materials are "Fe-122" single crystals, and we probe in the c-axis orientation. This may account for us not observing the larger gap as follows: An ARPES study on (Ba,K)Fe_2As_2 reveals an isotropic but FS sheet-dependent gap structure, where the β band has an averaged gap size $\sim 5.8\pm$

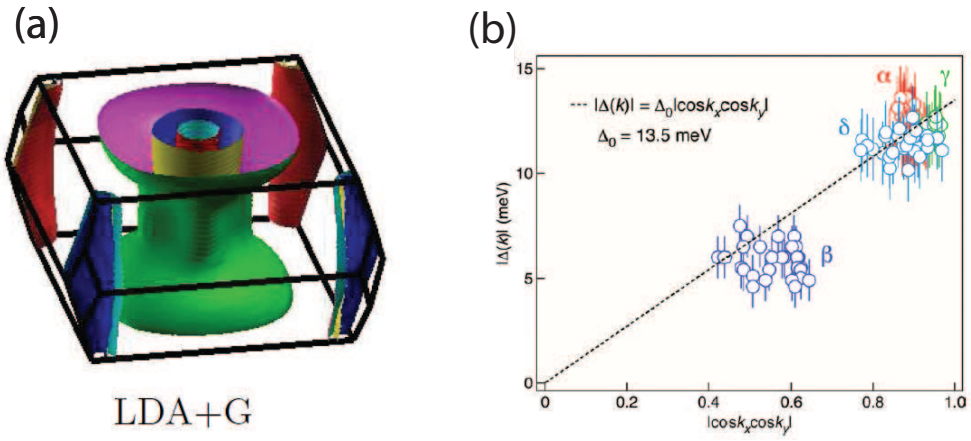

Figure 5.8: (a) Fermi surface topology from the band structure calculation. (Adapted from Ref. [162] (b) Gap values for different bands from ARPES measurements reported in [137].

0.8 meV with $2\Delta/k_BT_c \sim 3.6 \pm 0.5$ and the α,γ and δ bands have comparable gap sizes around 11-13 meV with $2\Delta/k_BT_c \sim 7.0 - 8.0$ as illustrated in Fig. 5.8(b)[137]. Considering the FSs from band structure calculations, the α,γ and δ bands are highly 2-dimensional with cylindrical shapes while the β band is strongly 3-dimensional due to the $d_{3z^2-r^2}$ component [162] shown in Fig. 5.8(a). The small gap observed here may correspond to the 3D β band. Because the Fermi velocity on the α,γ, and δ bands is mostly in the ab plane and perpendicular to the c-axis, these bands contribute a relatively small spectral weight for current flowing in the c-axis, and the coherent peaks from these larger-gap bands are almost absent in PCARS, similar to the case of MgB_2 [34]. Both gaps should then be observable if junction current is flowing within the ab plane. Szabó *et al.* report two superconducting gaps for PCARS measurement in the ab plane with $2\Delta_1/k_BT_c = 2.5 - 4$ and $2\Delta_2/k_BT_c = 9 - 10$ [163]. However, Andreev reflection is totally absent for their point-contact junctions in c-axis. This is distinct from our results and may be due to the sample difference.

The elastic, and inelastic, electron mean free paths, l_{el}, and l_{in}, respec-

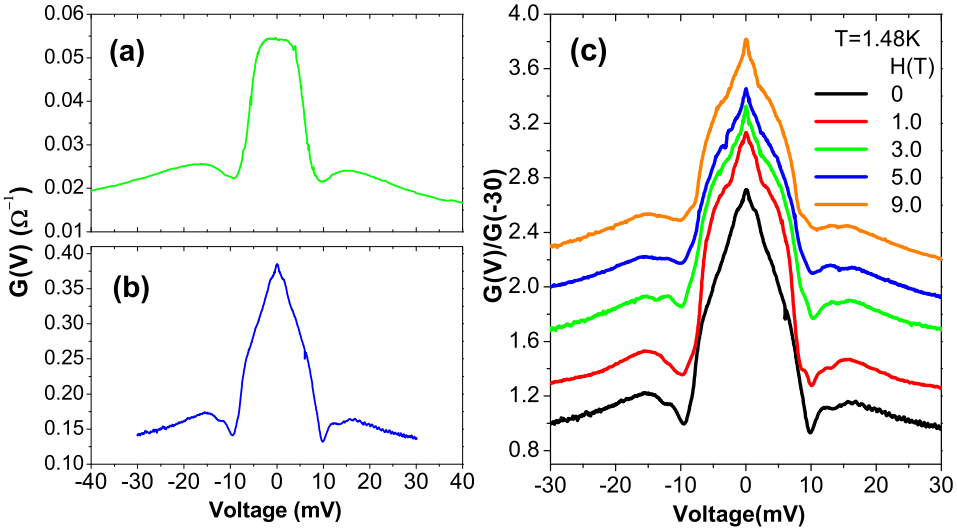

Figure 5.9: (a) & (b) Differential conductance curves G(V) without double-peak structure for the Au/(Ba,K)Fe_2As_2 point-contact junctions. (c) the field dependence of the G(V) in (b) at T=1.48 K. The curves are vertically shifted for clarity.

tively, are not known for (Ba,K)Fe_2As_2 single crystals. However, it is generally believed that they are bad metals and l_{el} could be a few tens of nanometers, making it difficult to form a contact in the Sharvin ballistic limit, (contact diameter d < l_{el}). For the contact in the diffusive regime ($l_{el} < d < \sqrt{l_{el} l_{in}}$), dips may arise from the extra finite resistance of the superconducting electrode when the junction current at a finite voltage bias exceeds the critical current [74]. The humps in Fig. 5.5 are possible signatures of such shallow dips, possibly diminished by the sloping background. As the point-contact is moved further away from the ballistic regime, the dip structure becomes more pronounced and a zero-bias conductance peak (ZBCP) is observed, rather than the usual double-peak. This is the explanation for the ZBCP seen in Fig. 5.9(a) & (b) and more pronounced dips at ± 10 meV than in Fig. 5.5. Although a peak at zero bias may arise from Andreev bound states in a d-wave superconductor [164], the width, the

lack of field dependence as shown in Fig. 5.9 (c), and the pronounced dip structures together indicate the ZBCP is due to the contact not being in the Sharvin limit.

5.3 PCARS on $Ba(Fe_{0.9}Co_{0.1})_2As_2$

$Ba(Fe_{0.9}Co_{0.1})_2As_2$ single crystals are also grown out of FeAs flux by the high temperature solution method as described in [165]. Two single crystals labeled as #1 and #2 are investigated by PCARS, and as shown in Fig. 5.10 (a), both show a superconducting onset temperature at ∼22 K as measured by the four-probe resistance method. The RRR is $\sim 2-3$, which is relatively low compared with the hole doped (Ba,K)Fe_2As_2 crystals, possibly due to enhanced scattering caused by the Co-dopants in the plane. The sharp superconducting transition of crystal #2 at Tc_{onset} ∼22 K as measured by both temperature-dependent resistance and magnetic moment is shown in Fig.5.10 (b) and (c), respectively.

Figure 5.11 displays the characteristic conductance curves for point-contact measurement on cleaved $Ba(Fe,Co)_2As_2$ single crystals at low temperatures. A zero-bias peak with hump features are frequently observed. The fine features change from contact to contact with energy scales independent of the superconducting gap. Sometimes when the Au tip is initially engaged onto the sample surface with a junction resistance around a few hundred ohms, V-shape G(V) curves are observed, as shown in Fig. 5.11. With increased tip pressure, the contact resistance reduces to tens of ohms and a zero-bias conductance peak generally emerges with broad shoulders up to $\sim \pm 20$ meV.

The temperature dependence of the G(V) for another point-contact junction of $Ba(Fe,Co)_2As_2$ is shown in Fig. 5.12. The ZBCP disappears above

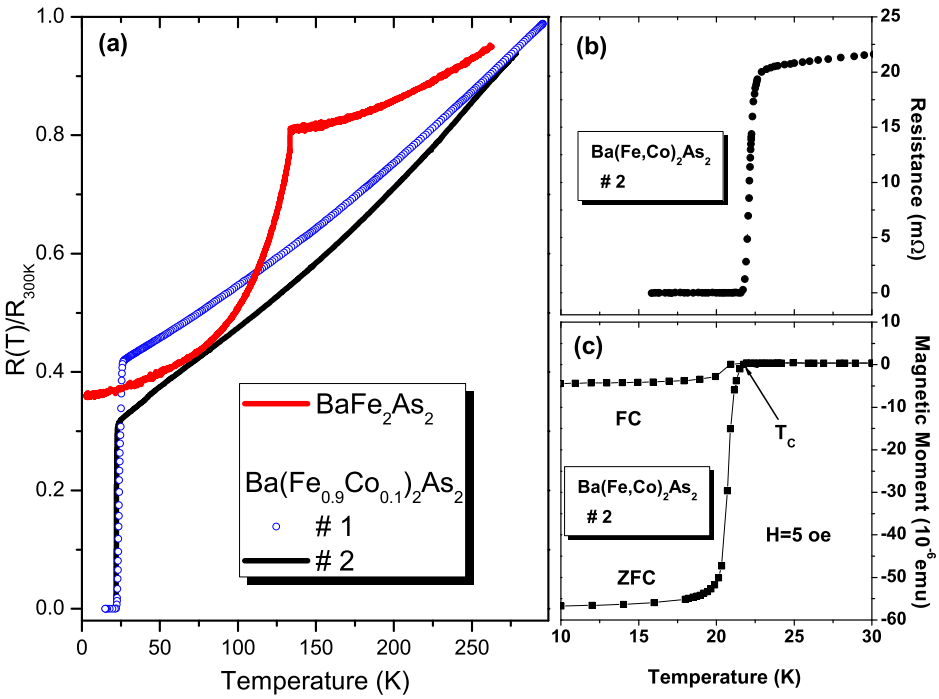

Figure 5.10: (a) Four-probe resistance measurement for $Ba(Fe_{0.9}Co_{0.1})_2As_2$ crystals #1 (blue dot) and #2 (black line) in comparison with the parent compound $BaFe_2As_2$ crystal (red line); temperature-dependent (b) resistance and (c) Field cooled (FC) and zero field cooled (ZFC) magnetic moment for $Ba(Fe_{0.9}Co_{0.1})_2As_2$ crystal #2. The superconducting transition is indicated by arrow. The magnetic field is 5 oe for both FC and ZFC in (c).

the bulk T_c indicating it originates from superconductivity. The shape of the curves and the junction resistance indicate the junctions are not in the Sharvin regime. The reproducibility of the Andreev reflection signal indicates the junction is in the diffusive (not thermal) limit, so some spectroscopic information can be extracted from the conductance data. This is likely due to the relative small mean free path, l_{ie} in these crystals, which is estimated to be around 81 Å with a coherence length, ξ=27.6 Å estimated from the residual resistivity and Hall coefficient measurement (ρ_0=0.23 mΩ cm and R_H=10^{-9} m^3/C) [166]. In order to be in the Sharvin limit, the junction resistance $R = \frac{16\rho l}{3\pi d^2} \gg \frac{16\rho}{3\pi l}$ ~482 Ω, and is difficult to be achieved in our

measurement.

Going back to the more commonly observed spectra of Fig. 5.11, the fine structures seen above the gap energy, varies from contact to contact and thus are unlikely intrinsic. If the fine structure is an interference effect, it should exhibit magnetic field dependence; The field would induce extra phase modulation and suppresses such interference effects. Fig. 5.13

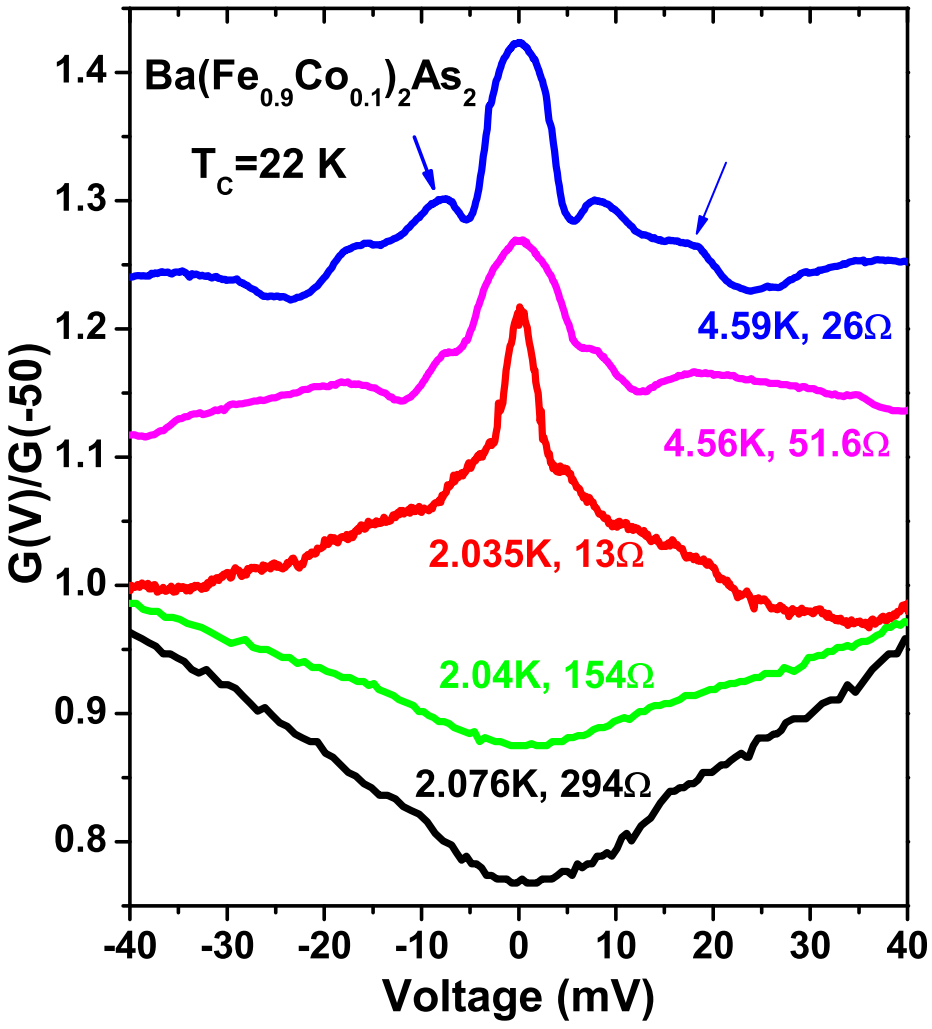

Figure 5.11: The normalized conductance curves, G(V), for Au-$Ba(Fe,Co)_2As_2$ point-contact junctions at low temperatures. The top two curves from different contacts are vertically shifted for clarity. The arrows point to the hump structures frequently observed concomitantly with the zero-bias peak.

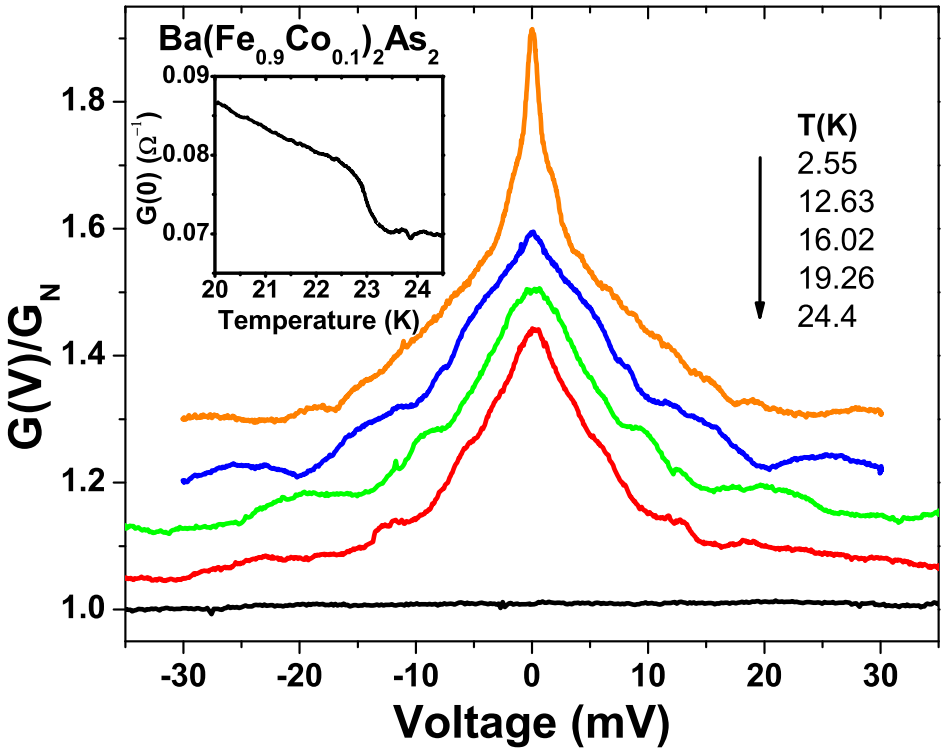

Figure 5.12: The temperature dependent normalized G(V)s for a Au-$Ba(Fe,Co)_2As_2$ point-contact junction with ZBCP. The curves are vertically shifted for clarity. Inset shows the temperature evolution of the zero-bias conductance around the bulk T_c. The junction resistance is 14 Ω just above the Tc.

(a) shows the field-dependent conductance curves, G(V), for a point-contact Au-$Ba(Fe_{0.9}Co_{0.1})_2As_2$ junction. As the magnetic field increases, the fine structure gradually disappears around 4 T while a broad zero-bias peak remains unchanged up to H=8 T. The V-shape background is masked by the Andreev reflection structure, and survives above the superconducting T_c as shown in Fig. 5.13(b), so we do not associate the background with the superconductivity. The field and temperature dependences of the conductance curves indicate the valleys marked by the arrows in Fig. 5.13(b) are not due to the dip structures known to occur in the diffusive regime [74].

Double-peak BTK-like conductance curves are not as frequently observed

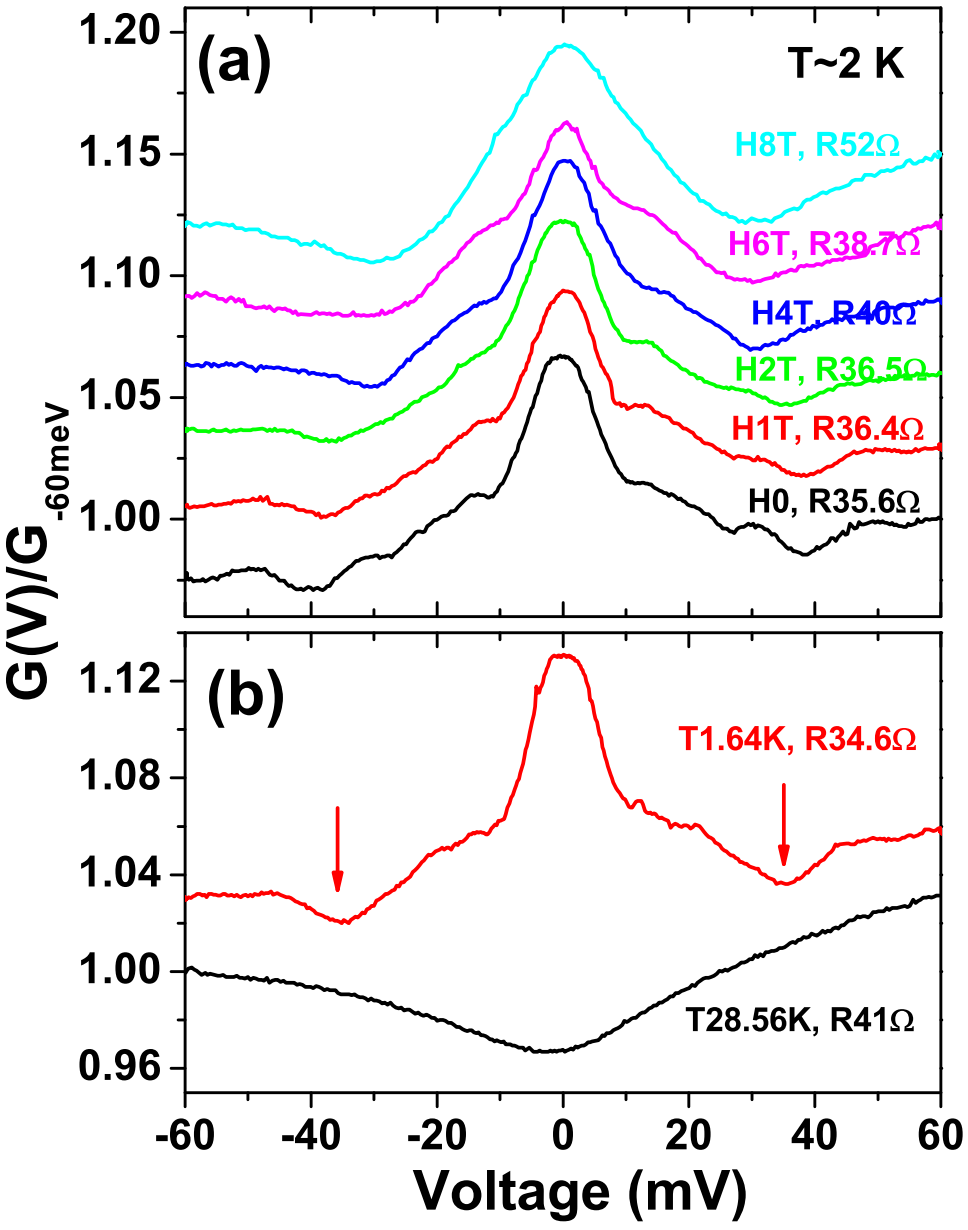

Figure 5.13: (a) The point-contact conductance curve, G(V), for a Au-$(Fe,Co)_2As_2$ point-contact junction as a function of magnetic field applied in the c-axis direction at T∼2 K. (b) G(V) curves for the point-contact at T=1.64 K (red) and 28.56 K (black) with a clear V-shape background. The valley structure is indicated by arrows. Curves are vertically shifted for clarity.

as in (Ba,K)Fe_2As_2. Fig. 5.14 shows such double-peak-like G(V) curves, which are rarely obtained. Note they have a common V-shape background. The amplitude of the Andreev reflection signal is never greater than 10% of the normal state conductance, and this is addressed later with more discussion about the multiple bands. The peak positions are less than thoese reported by Yin et al (the averaged Δ=6.25 meV) as measured by STM [166]. Their measurement puts Ba(Fe,Co)$_2As_2$ in the strong-coupling limit with $2\Delta/k_BT_c$ ~5.7. Since our PCARS data are not taken in the ballistic limit, the peaks may not reproducibly represent the energy gap value, so we do not assign one.

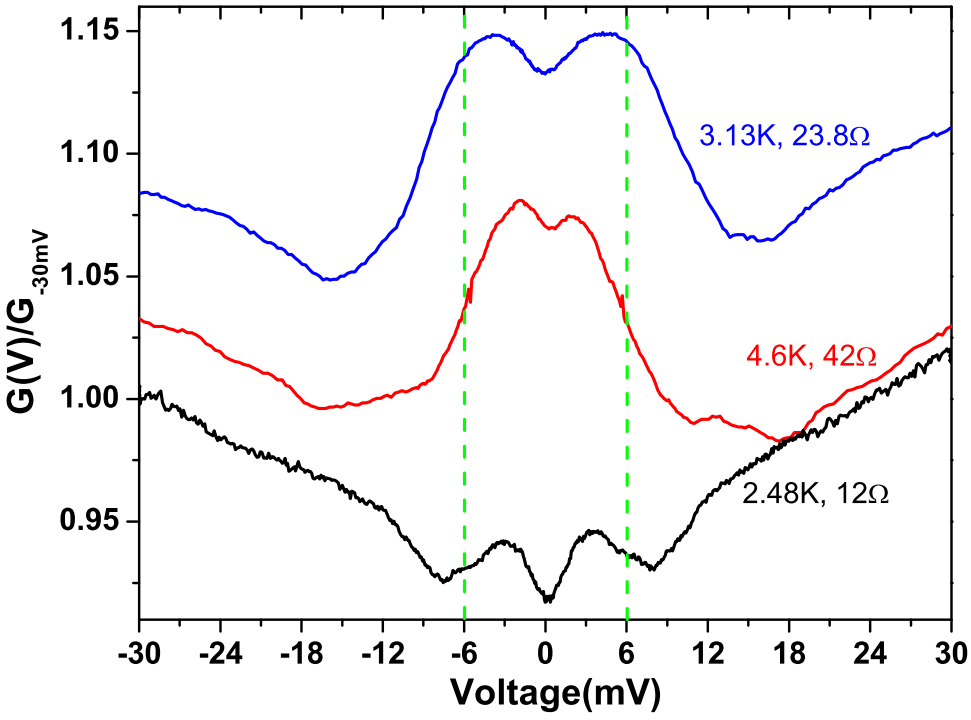

Figure 5.14: Double-peak features rarely observed for Au-(Fe,Co)$_2As_2$ point-contact junctions. The green dashed line marks ±6 mV, corresponding to the averaged coherent peaks observed in STM measurement [166]. The normalized curves are shifted vertically for clarity.

The origin of the V-shape conductance for the initial gentle point-contact

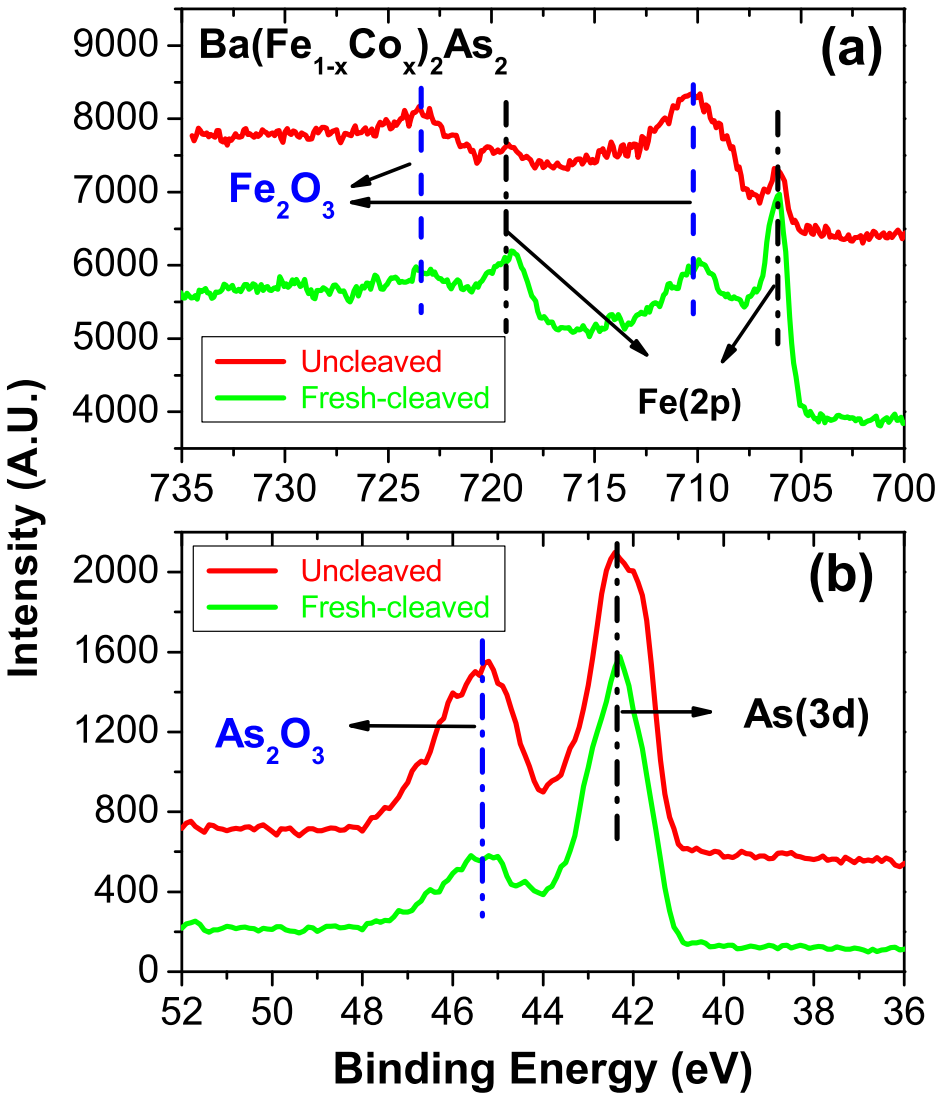

Figure 5.15: X-ray photoelectron spectra (XPS) of (a) Fe 2p-orbit and (b) Se 3d-orbit for the freshly cleaved $Ba(Fe,Co)_2As_2$ crystal (green) and uncleaved crystal exposed in the air for a whole day (red). The binding energies for Fe 2p-orbit are 706 and 719 eV and As 3d-orbit 42.3 eV, while the binding energies of the corresponding oxide shift to 711 and 724 eV for Fe 2p and 45.3 ev for As 3d.

or background for Au-$Ba(Fe,Co)_2As_2$ is not clear, but since increased tip pressure reveals Andreev reflection, it may be due to an oxidized surface layer. In order to check this scenario, X-ray photoemission spectroscopy (XPS) has been done on both uncleaved and freshly-cleaved surfaces, and

compared. XPS is a surface-sensitive technique with probe depth of around 100Å and often applied to detect oxide surface layer. The XPS data sets shown in Fig. 5.15 (a) and (b) show dramatic changes in both the Fe and As signals, respectively. The uncleaved crystal shows more spectral weight from the oxides, while the cleaved cyrstal shows more spectral weight from the pure elements. Clearly an oxide froms on an exposed samples, but the rate of oxide growth is not yet known.

We note that (Ba,K)Fe_2As_2 is more easily oxidized than Ba(Fe,Co)$_2As_2$ crystals [167].That is not consistent with our PCARS data in that we see Andreev reflection more frequently in (Ba,K)Fe_2As_2. We do note the V-shape background is not observed every tip position, implying non-uniformity of the sample surface, which may not be explained simply by a surface oxide layer. Thus, even in the presence of a thin surface oxidation layer detected by XPS, the sharp tip is likely to puncture it and probe the bulk superconductor Ba(Fe,Co)$_2As_2$. The robustness of the V-shape conductance background is then likely related to the intrinsic bulk property. The origin of the V-shaped background is discussed further in a later section.

5.4 PCARS on $(Sr_{0.6}Na_{0.4})Fe_2As_2$ & $Sr(Fe_{0.9}Co_{0.1})_2As_2$

Hole-doped $(Sr_{0.6}Na_{0.4})Fe_2As_2$ and electron-doped $Sr(Fe_{0.9}Co_{0.1})_2As_2$ are also prepared by the high temperature solution method with FeAs flux . The normalized temperature-dependent resistances for two $(Sr_{0.6}Na_{0.4})Fe_2As_2$ crystals overlap with each other as shown in Fig. 5.16, indicating a uniform sample quality with RRR=8 and $T_{c,zero}$ ∼36.5 K. The resistance for $Sr(Fe_{0.9}Co_{0.1})_2As_2$ shows $T_{c,zero}$ ∼20.0K with RRR=7. A kink is observed around 142K, far be-

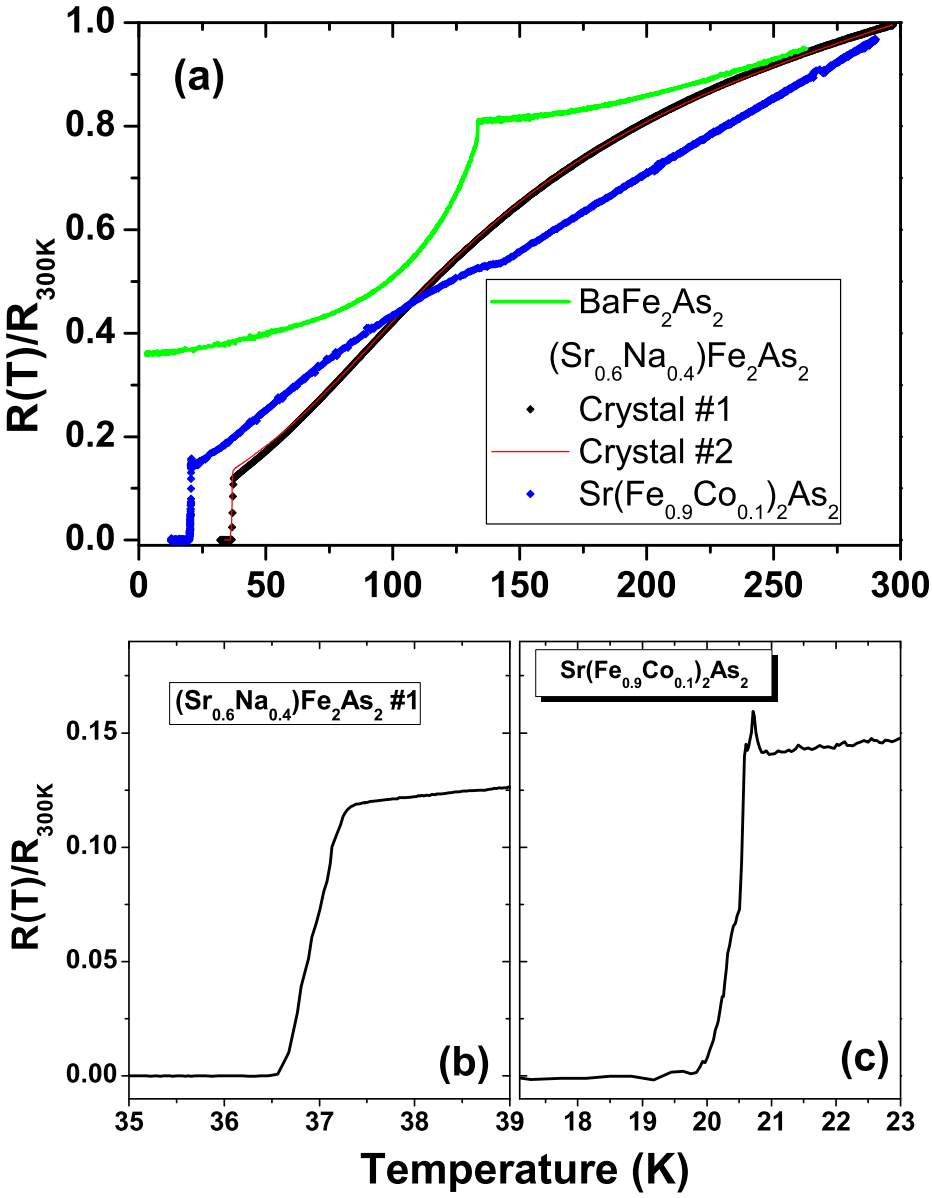

Figure 5.16: (a) Four-probe resistance measurement for $(Sr_{0.6}Na_{0.4})Fe_2As_2$ crystals #1 (black) and #2 (red) and $Sr(Fe_{0.9}Co_{0.1})_2As_2$ (blue) in comparison with the parent compound $BaFe_2As_2$ crystal (green); temperature-dependent resistance details in the transition region for (b) $(Sr_{0.6}Na_{0.4})Fe_2As_2$ crysal #1 and (c) $Sr(Fe_{0.9}Co_{0.1})_2As_2$

low the Neel temperature T_N ~200 K of the parent compound $SrFe_2AS_2$ [168]. The origin of the kink is unknown.

Figures 5.17 (b) and (c) show the typical G(V) curves with reduced con-

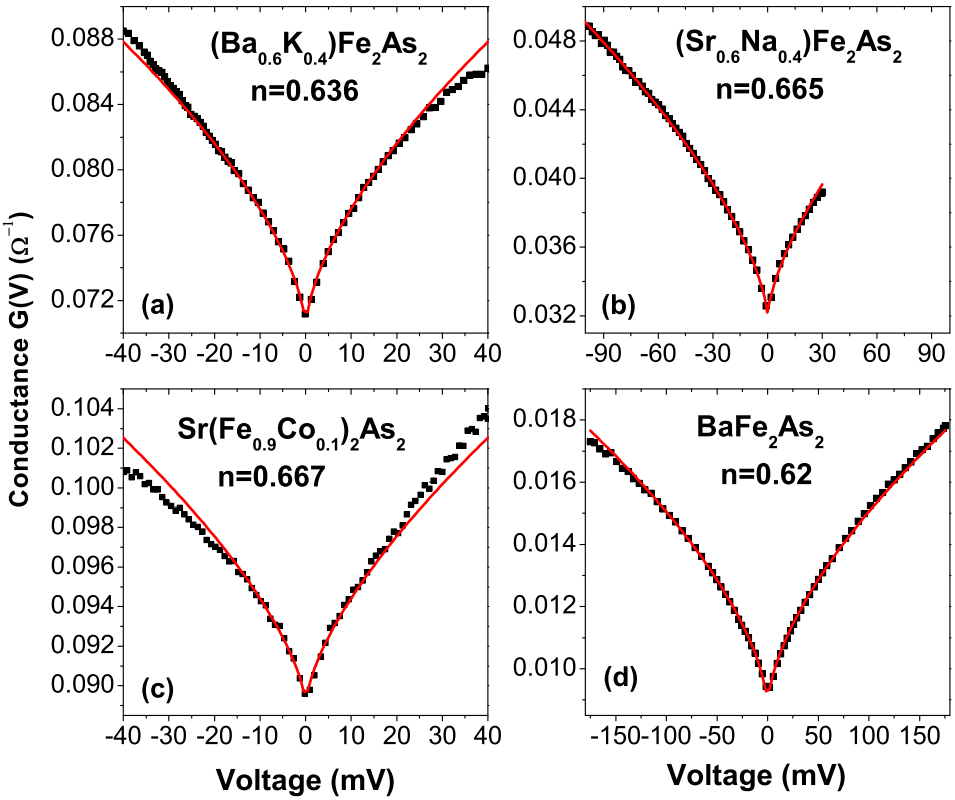

Figure 5.17: V-shape conductance valley (VCV): V-shape G(V) curves observed (black) and power law fit (red) with n as the fitted exponent for the point-contact junctions on different crystals: (a) $(Ba_{0.6}K_{0.4})Fe_2As_2$ at T=2.33 K; (b) $(Sr_{0.6}Na_{0.4})Fe_2As_2$ at T=2.20 K; (c) $Sr(Fe_{0.9}Co_{0.1})_2As_2$ at T=2.17 K; (d) $BaFe_2As_2$ at T=1.95 K.

ductance at lower voltage bias observed for the point-contact junctions on cleaved (Sr,Na)Fe_2As_2 and Sr(Fe,Co)$_2As_2$ surfaces. Similar features are also reported by other groups [157, 158]. Fig. 5.17(a) shows the same V-shape conductance valley (VCV), sometimes observed in the point-contact junctions on the same cleaved (Ba,K)Fe_2As_2 crystals as in section 5.2. We have also observed the same VCV feature for the nonsuperconducting parent compound $BaFe_2As_2$ single crystals even up to 200 meV, as shown in Fig. 5.17(d), where SDW magnetic order exists [169]. All the curves can be fit to a power law function $G(V) = G(0) + c * |V|^n$ with a power coefficient, n $\sim$ 2/3. This may indicate a universal origin of this VCV observed commonly among

different crystals.

Figure 5.18 shows the field dependence of the VCV feature for a point-contact junction on $Sr(Fe_{0.9}Co_{0.1})_2As_2$. No dramatic change of the conductance shape is observed with applied magnetic field up to 9 Tesla. We do not observe any splitting of the conductance valley (or resistance peak) with applied magnetic field, which may rule out Kondo impurity scattering as its origin [170]. This ZBA feature, without Andreev reflection, is probably due to the absence of superconductivity in the probed areas, even though bulk resistance measurements confirmed it. In the nonsuperconducting parent compound $BaFe_2As_2$, a structural transition occurs at the antiferromagnetic ordering temperature, $T_N \sim 135$ K. In doped superconducting Fe-122 materials, phase-separated coexistence of magnetic order and superconductivity is reported in recent muon spin rotation (μSR) studies [171, 172, 173] with a magnetic correlation length >100 Å. Park *et al.* [171] demonstrate the mesoscopic phase-separated coexistence of magnetically ordered and non-magnetic states on a lateral scale of $\sim$ 65 nm in a slightly underdoped $(Ba,K)Fe_2As_2$ system. Whether such coexistence is an intrinsic electronic property for the Fe-122 system or due to some crystalline inhomogeneity remains an open question.

In investigating the possibility that the VCV originates from magnetic order, we note magnetic order can be detected by PCARS [174]. A point-contact junction made on a superconducting region would exhibit Andreev reflection and one on a nonsuperconducting, magnetically ordered region, would not. Instead, a signature due to electron scattering from magnetic order may be detected. This may be the case for $(Sr,Na)Fe_2As_2$ and $Sr(Fe,Co)_2As_2$ where no Andreev reflection-like peak in G(V) has been observed, G(V) curves with the VCV feature are mostly observed. Goko et al. apply μSR to

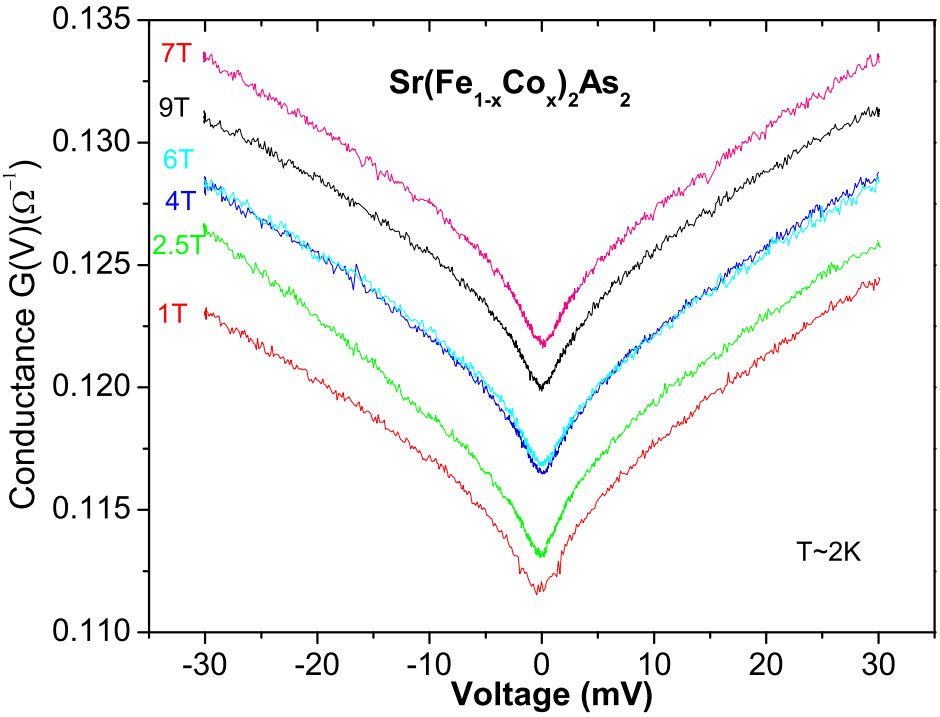

Figure 5.18: The V-shape conductance curves for a Au/Sr$(Fe_{0.9}Co_{0.1})_2As_2$ point-contact junction as a function of magnetic field at T∼2 K. The field is applied perpendicular to the ab plane of the crystal. The V-shape is seen to be robust under magnetic field.

investigate (Ba,K)Fe_2As_2 and (Sr,Na)Fe_2As_2 single crystals (same source as ours) and argue that static magnetism sets in at temperatures well above the superconducting T_c. They estimate the superconducting volume fraction to be 50 % in (Ba,K)Fe_2As_2 crystals and ∼ 90% in (Sr,Na)Fe_2As_2 crystals at low temperatures [173]. This is consistent with our more frequent observation of ZBA features in (Sr,Na)Fe_2As_2 than in (Ba,K)Fe_2As_2 cystals.

Temperature dependent Point-contact measurements for the parent compound $BaFe_2As_2$ reveal the VCV feature is broadened and reduced with increasing temperature, as shown in both Fig. 5.19(a) and (b). As the Neel temperature (T_N ∼135 K) is crossed, no dramatic change in the spectrum is observed, but thermal population effects may mask changes in conductance

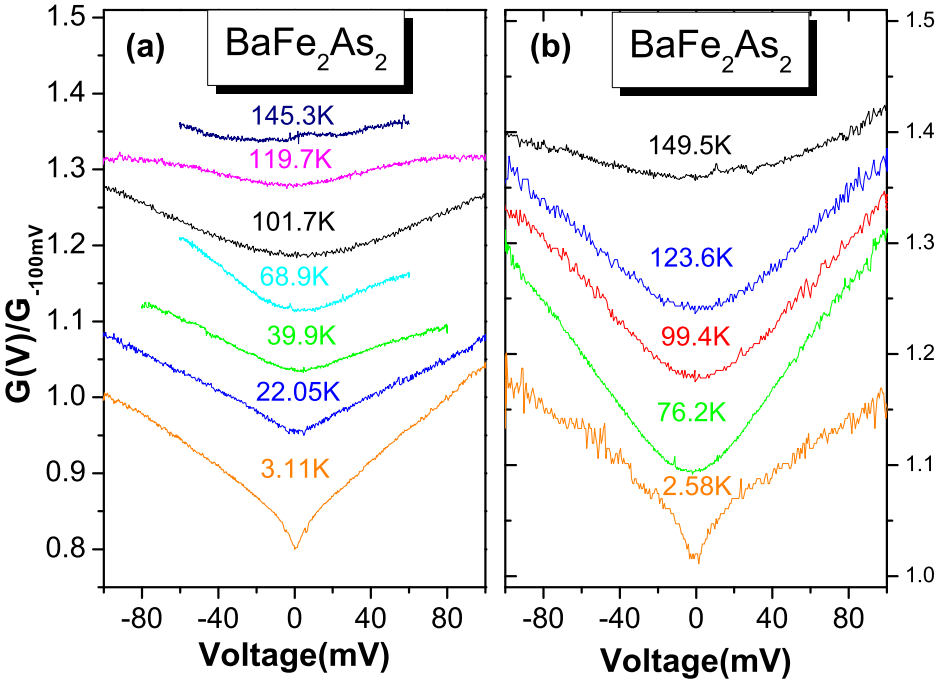

Figure 5.19: Two examples of the temperature dependence of the normalized conductance curves, G(V)/G(V=-100), taken on two locations (a) and (b) on a non-superconducting parent compound $BaFe_2As_2$ crystal with T_N ~135 K. The curves are vertically shifted for clarity.

at the magnetic transition. Above T_N, the G(V) curve is flat in Fig. 5.19(a) while it is still parabolic in Fig. 5.19(b).

5.5 Discussions

Even though the isotope effect is observed in the iron pnictide superconductors [175], their magnetic ground state leads to the possibility that antiferromagnetic spin fluctuations play an important role in the superconducting pairing state. Mazin *et al.* argue that the exchange of spin fluctuations mediates the pairing. In this case, when the signs of the order parameter connected by the SDW vector, $\overrightarrow{\mathbf{Q}}$, are opposite, the total ground state energy can be reduced to form the superconducting state. For the iron-based

family, one or more hole Fermi surfaces (FSs) and electron FSs are displaced by the SDW wave vector. This unavoidably leads to the favored $s\pm$ superconducting state, which forms a fully gapped order parameter with opposite signs for the electron and hole bands [176].

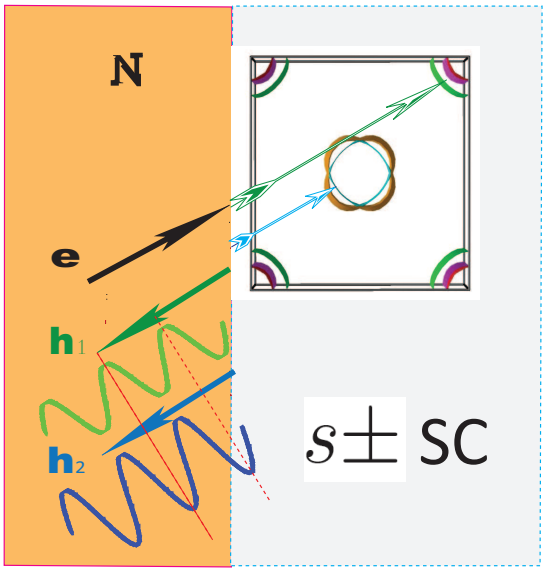

Figure 5.20: Schematic diagram of Andreev reflection across the N/S interface for the $s\pm$-wave iron-pnictide. The green arrows denote the transmission to the electron band in S and related Andreev reflection in N, while the blue arrows denote the transmission to the hole band in S and related Andreev reflection in N. The Andreev reflected holes have a π phase shift.

In the case of s±, from the theoretical point of view, the Andreev reflection from different bands has a profound effect due to the π phase shift: destructive interference of Andreev reflected holes. The corresponding problem is modeled by Golubov *et al* [177] based on the BTK model, introducing another parameter,α, which is the ratio of probability of a quasiparticle entering the first band to that entering the second band. For a normal metal-superconductor contact, the quasiparticle wave function in the superconductor is then:

$$\Psi_s = c\left[\phi_p\begin{pmatrix}\mu_1\\ \nu_1 e^{-i\psi_1}\end{pmatrix}+\alpha_0\phi_q\begin{pmatrix}\mu_2\\ \nu_2 e^{-i\psi_2}\end{pmatrix}\right]+d\left[\phi_{-p}\begin{pmatrix}\nu_1\\ \mu_1 e^{-i\psi_1}\end{pmatrix}+\alpha_0\phi_{-q}\begin{pmatrix}\nu_2\\ \mu_2 e^{-i\psi_2}\end{pmatrix}\right]$$

Applying the same boundary conditions as employed in the BTK model

and the relation $\psi_1 - \psi_2 = \pi$ for the $s_\pm$ order parameter, the coefficients are:

$$\begin{aligned}
\gamma a &= \mu_1\nu_1 - \alpha(\mu_1\nu_2 + \mu_2\nu_1) + \alpha^2\mu_2\nu_2, \\
\gamma b &= (Z^2 + iZ)[\nu_1^2 - \mu_1^2 + \alpha^2(\mu_2^2 - \nu_2^2)], \\
\gamma c &= (1 - iZ)(\mu_1 - \alpha\mu_2), \; and \; \gamma d = iZ(\nu_1 - \alpha\nu_2),
\end{aligned}$$

where $\gamma = (1 + Z^2)(\mu_1^2 - \alpha^2\mu_2^2) - Z^2(\nu_1^2 - \alpha^2\nu_2^2)$. The current, I, flowing across the interface is still given as following:

$$I = \frac{1}{eR_N}\int_{-\infty}^{+\infty}[f_0(E - eV) - f_0(E)][1 + A - B]dE.$$

Fig. 5.21 (a) shows calculated G(V) curves as a function of the band ratio α, for $\Delta_1 = 1$, $\Delta_2 = 2$, and a perfectly transparent interface (Z=0). The conductance enhancement within Δ_1 gets suppressed when $\alpha \sim \sqrt{\Delta_1/\Delta_2}$ because the destructive interference is more pronounced when the two bands have comparable wave amplitude. As the band ratio increases, the spectra get more and more similar, and the single-band BTK model is recovered.

Figure 5.21(b) shows the calculated G(V) curves as a function of the band ratio, α, also for $\Delta_1 = 1$ and $\Delta_2 = 2$, but now in the tunneling regime (Z=10). when $\alpha \leq \sqrt{\Delta_1/\Delta_2}$, sharp sub-gap peaks are seen due to Andreev bound states. For Z$\gg$1, singularity occurs at $\gamma = 0$ and that determines the bound state energies, $E_B = \sqrt{(\Delta_1^2 - \alpha^4\Delta_2^2)/(1 - \alpha^4)}$. The bound states only exist for $0 \leq \alpha \leq \sqrt{\Delta_1/\Delta_2}$ and $\alpha \geq 1$. The bound state energy E_B, changes with the band ratio, α, and is not fixed at zero as it is for the surface-induced Andreev bound states in the d-wave cuprates.

These interesting properties originate from the π phase shift in the hole and electron band. However, in the practice of PCARS measurement, no

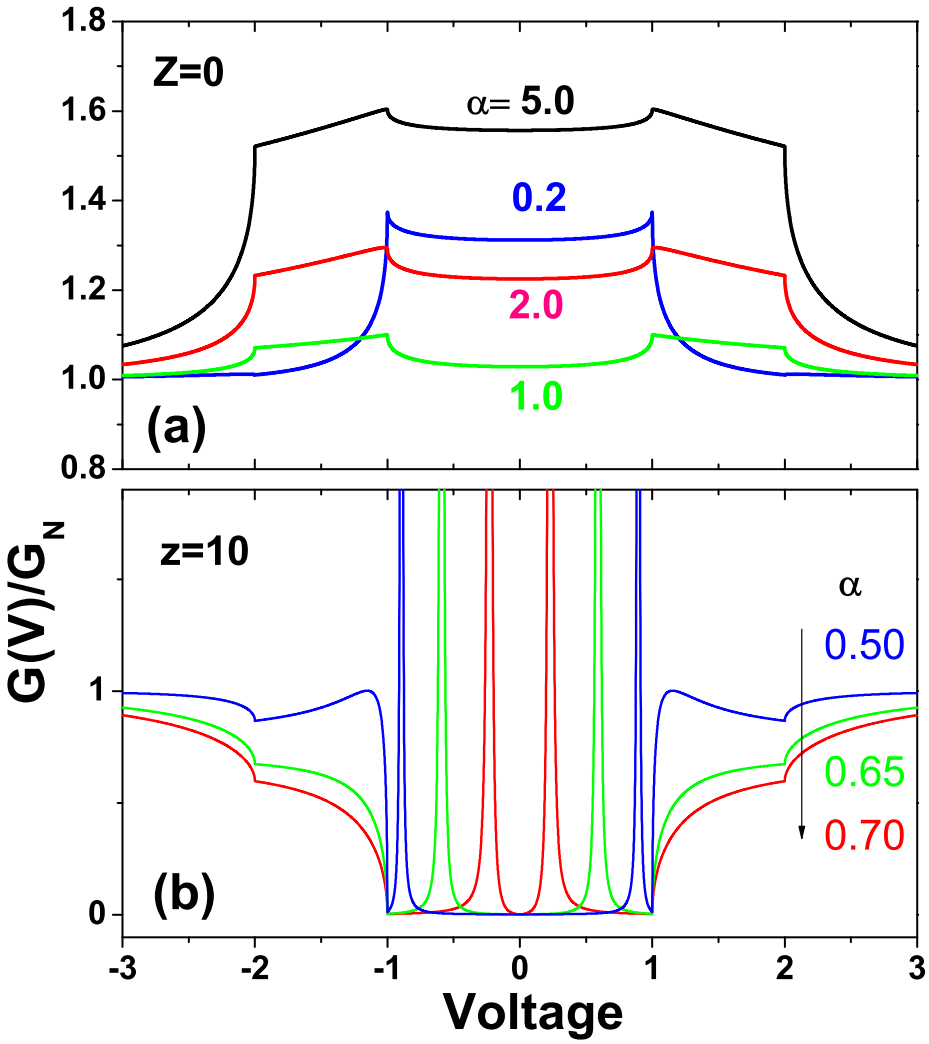

Figure 5.21: Calculated conductance curves of a point-contact junction on an s± superconductor with different band ratios, α, in (a) the perfect transparency limit (Z=0), and (b) the tunneling limit (Z=10), where it is assumed Δ_1=1 and Δ_2=2. The bound states energy in (b) is not fixed at the Fermi level as for a d-wave superconductor but at a finite energy depending on the band ratio, α.

such behavior has been reported so far and all the data are analyzed in the conventional BTK model with either one-gap or two independent gap channels, in the same way as the two-gap superconductor MgB_2 is analyzed [34, 35, 36].

In conclusion, our PCARS measurements on the cleaved (Ba,K)Fe_2As_2

single crystal surfaces show a superconducting gap energy of ~ 4 meV when G(V) curves are analyzed by the single-gap BTK model. For point-contacts on $Ba(Fe,Co)_2As_2$, the junctions are usually not in the ballistic limit. A universal power law behavior of the G(V) curves with the VCV feature in all Fe-122 superconducting samples we measure may be related to the mesoscopic phase-separated coexistence of magnetic and superconducting phases in the 122 system. Further investigations are needed to understand the microscopic origin of the anomaly. Point-contact measurements in the ab-plane would be helpful to explore the in-plane gap structure of these new high Tc superconductors.

Chapter 6

Concluding Remarks

In this thesis we show that quasiparticle tunneling and Andreev reflection across a planar or point-contact junction lead to characteristic conductance curves, G(V), intimately related to the order parameter symmetry and superconducting gap structure. In many cases as presented here, measuring the G(V) curves by the ac modulation method and analyzing the data with the orginal or extended Blonder-Tinkham-Klapwijk (BTK) models allow us to extract the superconducting gap structure and its dependence on temperature and applied magnetic field. We are interested in extending these measurements to study and understand these properties in multiband superconductors.

There is much renewed interest in the "conventional" superconductor $NbSe_2$(T_c ~7.1 K) due to its possible multiband or anisotropic nature of the superconducting gap. G(V) curves for the point-contact Au/$NbSe_2$ junctions are measured as a function of temperature. The simulated gap value at T ~2 K varies from 0.9 to 1.5 meV, consistent with the multigap scenario claimed by other experiments. The superconducting gap follows the BCS temperature dependence for weak-coupling superconductors.

We performed extensive PCARS studies on the nonmagnetic borocarbides $LuNi_2B_2C$ and YNi_2B_2C, with $T_c \sim$ 16.5 K and 15.5 K, respectively. In order to check the gap anisotropy and probe the possible point nodes reported in the literature [98, 99], single crystals in three major crystallo-

graphic orientations ([001], [110], [100]) are prepared and clean surfaces are guaranteed by aqua regia etching. When analyzing the $LuNi_2B_2C$ data with the one-gap BTK model, a small gap anisotropy is observed for PCARS with Δ_{001} ~2.4 meV, $\Delta_{110} \sim 2.6$ meV and $\Delta_{100} \sim 2.3$ meV. PCARS on another set of $LuNi_2B_2C$ samples gives Δ_{001} ~2.5 meV, $\Delta_{110} \sim 2.8$ meV and $\Delta_{100} \sim 2.7$ meV. For the YNi_2B_2C samples, $\Delta_{100} \sim 2.5$ meV is even larger than $\Delta_{110} \sim$ 2.1 meV and $\Delta_{001} \sim 2.0$ meV. Point nodes proposed to exist in the [100] direction, due to the nesting structure in the Fermi surface and corresponding anitferromagentic (AFM) fluctuations, are not observed in our PCARS. This can be explained by the fact that other Fermi surface sheets from the 17th band, with $\Delta \geq$2.1 meV in [100] direction, mask the point-node structure and result in a small gap anisotropy, as observed in our PCARS. A large tunneling cone in PCARS measurements, which would smear the differences for the G(V) curves in three directions, may be another origin of the observed small gap anisotropy. Planar tunneling spectroscopy on borocarbide crystals would help to achieve more conclusive results and efforts to make planar junctions are in progress.

Finally, PCARS is applied to investigate the recently-discovered AFe_2As_2 (Fe-122) family of iron-based superconductors. The observed point-contact junction conductance curves, G(V), can be divided into two categories: one where Andreev reflection is present for $(Ba_{0.6}K_{0.4})Fe_2As_2$ and $Ba(Fe_{0.9}Co_{0.1})_2As_2$, and the other without AR but $V^{2/3}$ shape conductance curves for $Sr_{0.6}Na_{0.4}Fe_2As_2$ and $Sr(Fe_{0.9}Co_{0.1})_2As_2$. The latter is also observed for point-contacts on the nonsuperconducting parent compound $BaFe_2As_2$. The coexistence of phase-separated magnetic and superconducting orders on the mesoscopic scale is considered to explain distinct behaviors in the superconducting samples. A gap size ~3.0-4.0 meV with $2\Delta_0/k_BT_c \sim$ 2.0-2.6 is observed for PCARS on

$Ba_{0.6}K_{0.4}Fe_2As_2$, consistent with the smaller gap size reported in the Ln-FeAsO family ("Fe-1111"). For $Ba(Fe_{0.9}Co_{0.1})_2As_2$, G(V) curves typically display a zero-bias conductance peak, sometimes with a V-shape background. It is necessary to understand the origin of the frequently observed V-shape conductance valley before we can understand the Andreev reflection and superconducting gap. PCARS measurements in the ab plane directions would also be helpful to extract more detailed gap structure. Finally we have shown, especially for the iron based superconductors with multiple Fermi surfaces and possible S± superconducting order parameter symmetry, the importance of taking into account multiple bands exhibiting different phases and the interference which then may arise. Planar tunneling spectroscopy is a promising technique to probe the bound sates resulted from the proposed S± paring symmetry.

References

[1] Kamerlingh-Onnes 1911 *Leiden Communications* **122b** 124c

[2] Meissner W and Oschenfeld R 1933 *Naturwiss* **21** 787

[3] London F and London H 1935 *Proc. R. Soc. London* **A149** 71

[4] Ginzburg V L and Landau L D 1950 *Zh. Eksperim. i teor. Fiz.***20** 1064

[5] Abrikosov A A 1957 *Sov. Phys. JETP* **5** 1174

[6] Cooper L N 1956 *Phys. Rev.* **104** 1189

[7] Bardeen J, Cooper L N and Schrieffer J R 1957 *Phys. Rev.* **106** 162; **108** 1175

[8] Maxwelll E 1950 *Phys. Rev.* **78** 477

[9] Reynolds C A, Serin B, Wright W H and Nesbitt L B *Phys. Rev.* **78** 487

[10] Glover R E and Thinkham M *Phys. Rev.* **104** 844 (1956); **108** 243 (1957)

[11] Corak W S, Goodman B B, Satterthwaite C B and Wexler A *Phys. Rev.* **96** 1442 (1954); **102** 656 (1956)

[12] Giaever I 1960 *Phys. Rev. Lett.* **5** 147

[13] Josephson B D 1962 *Phys. Lett.* **1** 251

[14] Bednorz J G and Müller K A 1986 *Z. Phys.* **B64** 189

[15] Wu K M *et al.* 1987 *Phys. Rev. Lett.* **58** 908

[16] Chu C W, Gao L, Chen F, Huang Z J, Meng R L and Xue Y Y 1993 *Nature* **365** 323

[17] Gao L, Xue Y Y, Chen F, Xiong Q, Meng R L, Ramirez D, Chu C W, Eggert J H, and Mao H K 1994 *Phys. Rev.* B **50** 4260.

[18] Ding H, Norman M R, Campuzano J C, Randeria M, Bellman A F, Yokoya T, Takahashi T, Mochiku T and Kadowaki K 1996 *Phys. Rev.* B **54** R9678

[19] Martindale J A, Barrett S E, Klug C A, O'Hare K E, DeSoto S M, Slichter C P 1992 *Phys. Rev. Lett.* **68** 702

[20] Wollman D A, VanHarlingen D J, Lee W C, Ginsberg D M and Leggett A J 1995 *Phys. Rev. Lett.* **74** 797

[21] Tanaka K *et al.* 2006 *Science* **314** 1910

[22] Kivelson S A and Emery V J 1995 *Nature* **374** 434

[23] Xu Z A *et al.* Xu Z A *et al.* 2000 *Nature* 406 486

[24] Wang Y, Li L and Ong N P 2006 *Phys. Rev.* B **73** 024510

[25] Gomes K K *et al.* 2007 *Nature* **447** 569

[26] Steglich F, Aarts J, Bredl C D, Lieke W, Meschede D, Franz W and Schäfer 1979 *Phys. Rev. Lett.* **43** 1892

[27] Stewart G R, Fisk Z, Willis J O and Smith J L 1984 *Phys. Rev. Lett.* **52** 679

[28] Thompson J D *et al.* 2003 *Phys.* B **329-333** 446

[29] Geibel C *et al.* 1991 *Z. Phys.* B **84** 1

[30] Hertz J 1976 *Phys. Rev.* B **14** 1165

[31] Coleman P and Schofield A 2005 *Nature* **433** 226

[32] Nagamatsu J, Nakagawa N, Muranaka t, Zenitani Y and Akimitsu J 2001 *Nature* **410** 63

[33] Szabó P, Samuely P, Kačmarčík J, Klien T, Marcus J, Fruchart D, Miraglia S, Marcenat C and Jansen A G M 2001 *Phys. Rev. Lett.* **87** 137005

[34] Gonnelli R S, Daghero D, Ummarino G A, Stepanov V A, Jun J, Kazakov S M and Karpinski J 2002 *Phys. Rev. Lett.* **89** 247004

[35] Gonnelli R S, Daghero D, Calzolari A, Ummarino G A, Dellarocca V and Stepanov V A 2004 *Phys. Rev.* B **69** 100504(R)

[36] Yanson I K and Naidyuk Yu G 2004 *Low Temp. Phys.* **30** 261;

[37] Tinkham M *Introduction to Superconductivity*, 2^{nd} ed. 1996 New York: McGraw Hill. Chapter 3

[38] Wolf E L *Principles of Electron Tunneling Spectroscopy* 1985 New York: Oxford University Press.

[39] Esaki L 1958 *Phys. Rev.* **109** 603

[40] Yanson I K 1974 *Sov. Phys.-JETP* **39** 506

[41] Binnig G and Rohrer H 1986 *IBM Journal of Research and Development* **30** 4

[42] Harrison W A 1961 *Phys. Rev.* **123** 85

[43] Andreev A F 1964 *Sov. Phys.-JETP* **19** 1228

[44] Wolf S 1971, Ph. D. thesis (Rutgers University)

[45] de Gennes, P and Saint-James D 1963 *Phys. Lett.* **4** 151

[46] Hu C-R 1994 *Phys. Rev. Lett.* **72** 1526

[47] Wolf E L, Zasadzinski J, Osmun J W and Arnold G B 1980 *J Low Temp. Phys.***40** 19

[48] Blonder G E, Tinkham M and Klapwijk T M 1982 *Phys. Rev.* B **25** 4515

[49] Deutscher G 2005 *Rev. Mod. Phys.* **77** 109

[50] Plecenník A, Grajcar M, Beňačka I C V, Seidel P and Pfuch A, 1994 *Phys. Rev.* B **49** 10016

[51] McMillan W L and Rowell J M *Phys. Rev. Lett.* **14** 108

[52] Giaever I 1969 In *Tunneling Phenomena in Solids* (eds. Brustein E and Lundqvist S), P. 19. Plenum, New York

[53] Garno J P 1977 *J. Appl. Phys.* **48** 4627

[54] Morohashi S, Shinoki F, Shoji A, Aoyagi M and Hayakawa H 1985 *Appl. Phys. Lett.* **46** 1179

[55] Sakamoto Y, Yoshida H, Sahuraba T, Odawara A, Marayama Y and Endo T 1991 *IEEE Trans. Instrum. Measur.* **40** 312

[56] Rowell J M, Gurvitch M and Geerk J 1981 *Phys. Rev.* B **24** 2278

[57] Rudman D A and Beasley M R 1980 *Appl. Phys. Lett.* **36** 1010

[58] Giaever I and Zeller H R 1968 *Phys. Rev. Lett.* **21** 1385

[59] Wang Z, Kawakami A, Uzawa Y and Komiyama B 1996 *J. Appl. Phys.* **79** 7837

[60] Moodera J S, Meservey R and Tedrow P M 1982 *Appl. Phys. Lett.* **41** 488

[61] Murphy R 2008 *Internal report*

[62] Duif A M 1983 Doctoraalscriptie, Nijmegen. (unpublished)

[63] Eliashberg G M 1960 *Sov. Phy.-JETP* **11** 696

[64] Scalapino D J, Schrieffer J R and Wilkins J W 1966 *Phys. Rev.* **148** 263

[65] Ren B, Picardi G and Pettinger B 2004 *Rev. Sci. Instru.* **75** 837

[66] McMinis J 2005, Internal Group Report

[67] Park W K and Greene L H 2006 *Rev. Sci. Instru.* **77** 023905

[68] Naijyuk Yu G and Yanson I K 2005 *Point-Contact Spectroscopy* (New York: Spriner Science+ Business Media, Inc.)

[69] Sharvin Yu V 1965 *Sov. Phys.-JETP* **21** 655.

[70] Kulik I O 1992 *Sov. J. Low Temp. Phys.* **18** 302

[71] Wexler A, 1966 *Proc. Phys. Soc.* **89** 927

[72] Yan H Q, Agterberg D F, Hayashi N, Badica P, Vandervelde D, Togano K, Sigrist M and Salamon M B 2006 *Phys. Rev. Lett.* **97** 017006

[73] Nishiyama M, Inada Y and Zheng G-q 2005 *Phys. Rev.* B **71** 220505(R)

[74] Sheet G, Mukhopadhyay S and Raychaudhuri P 2004 *Phys. Rev.* B **69** 134507

[75] Shan L, Tao H J, Gao H, Li Z Z, Ren Z A, Che G C and Wen H H 2003 *Phys. Rev.* B **68** 144510

[76] Park W K, Sarrao J L, Thompson J D and Greene L H 2008 *Phys. Rev. Lett.* **100** 177001

[77] Straub Th, Finteis Th, Claessen R, Steiner P, Hüfner S, Blaha P, Oglesboy C S and Bucher E 1999 *Phys. Rev. Lett.* **82** 4504

[78] Tonjes W C, Greanya V A, Liu Rong, Olson C G and Molinié 2001 *Phys. Rev.* B **63** 235101

[79] Rossnagel K, Sefarth O, Kipp L, Skibowski M, Voß, Krü ger P, Mazur A and Pollmann J 2001 *Phys. Rev.* B **64** 235119

[80] Valla T, Fedorov A V, Johnson P D, Glans P-A, McGuinness C, Smith K E, Andrei E Y and Berger H 2004 *Phys. Rev. Lett.* **92** 086401

[81] Hess H F, Robinson R B, Dynes R C, Valles J M and Waszczak J V *Phys. Rev. Lett.* **62** 214

[82] Suderow H, Tissen V G, Brison J P, Martínez J L and Vieira S 2005 *Phys. Rev. Lett.* **95** 117006

[83] Yokoya T, Kiss T, Chainani A, Shin S, Nohara M and Takagi H 2001 *Science* **294** 2518

[84] Graebner J E and Robbins M 1976 *Phys. Rev. Lett.* **36** 422

[85] Rodrigo J G and Vieira S 2004 *Phys.* C **404** 306

[86] Boaknin Etienne, Tanatar M A, paglione Johpierre, Hawthorn D, Ronning F, Hill R W, Sutherland M, Taillefer Louis, Sonier Jeff, Hayden S M and Brill J W 2003 *Phys. Rev. Lett.* **90** 117003

[87] Huang C L, Lin J-Y, Chang Y-T, Sun C P, Shen H Y, Chou C C, Berger H, Lee T K and Yang H D 2007 *Phys. Rev.* B **76** 212504

[88] Fletcher J D, Carrington A, Diener P, Rodière P, Brison J P, Prozorov R, Olheiser T and Giannetta R W 2007 *Phys. Rev. Lett.* **98** 057003

[89] Yan Jing, Shan Lei, Wang Yue, Xiao Zhi-Li and Wen Hai-Hu 2008 *Chin. Phys.* B **17** 2229

[90] Guillamon I, Suderow H, Guinea F and Vieira S 2007 arXiv:0711.2161 unpublished

[91] Kohen A, Proslier Th, Cren T, Noat Y, Sacks W, Berger H and Roditchev D 2006 *Phys. Rev. Lett.* **97** 027001

[92] Martínez-Samper P, Rodrigo J G, Agraït N, Grande R and Vieira S 2000 *Phys.* C **332** 450

[93] Soto F, Berger H, Cabo L, Carballeira C, Mosqueira J, Pavuna D, Toimil P and Vidal F 2007 *Physica* C **460-462** 789

[94] Suhl H, Matthias B T and Walker L R 1959 *Phys. Rev. Lett.* **3** 552

[95] Boaknin E, Hill R W, Proust C, Lupien C, Taillefer L and Canfield P C 2001 *Phys. Rev. Lett.* **87** 237001

[96] Yang L S, Klein M V, Cooper S L, Canfield P C, Cho B K and Lee S-I 2000 *Phys. Rev.* B **62** 1291

[97] Yokoya T, Kiss T, Watanabe T, Shin S, Nohara M, Takagi H and Oguchi T 2000 *Phys. Rev. Lett.* **85** 4592

[98] Izawa K, Yamaguchi H, Matsuda Y, Shishido H, Settai R and Onuki Y 2001 *Phys. Rev. Lett.* **87** 057002

[99] Park T, Salamon M B, Choi E M, Kim H J and Lee S-I 2003 *Phys. Rev. Lett.* **90** 177001

[100] Park T, Chia E E M, Salamon M B, Bauer E D, Vekhter I, Thompson J D, Choi E M, Kim H J, Lee S-I and Canfield P C 2004 *Phys. Rev. Lett.* **92** 237002

[101] Maki K, Thalmeier P and Won H 2002 *Phys. Rev.* B **65** 140502

[102] Dugdale S B, Alam M A, Wilkinson I, Hughes R J, Fisher I R, Canfield P C, Jarlborg T and Santi G 1999 *Phys. Rev. Lett.* **83** 4824

[103] Martínez-Samper P, Suderow H, Vieira S, Brison J P, Luchier N, Lejay P and Canfield P C 2003 *Phys. Rev.* B **67** 014526

[104] Kontani H 2004 *Phys. Rev.* B **70** 054507

[105] Shulga S V, Drechsler S-L, Fuchs G, Müler K-H, Winzer K, Heinecke M and Krug K 1998 *Phys. Rev. Lett.* **80** 1730

[106] Mukhopadhyay S, Sheet G, Raychaudhuri P and Takeya H 2005 *Phys. Rev.* B **72** 014545

[107] Naidyuk Y G, Bashlakov D L, Yanson I K, Fuchs G, Behr G, Souptel D and Drechsler S L 2006 *cond-mat/0609769*

[108] Bobrov N L, Beloborod'ko S I, Tyutrina L V, Yanson I K, Naugle D G and Rathnayaka K D D 2005 *Phys. Rev.* B **71** 014512

[109] Drechsler S-L, Rosner H, Shulga S, Opahle I, Eschrig H, Freudenberger J, Fuchs G, Nenkov K, Müller K-H, Bitterlich H *et al.* 2001 *Phys.* C **364-365** 31

[110] Yamauchi K, Katayama-Yoshida H, Yanase A and Harima H 2004 *Phys.* C **412-414** 225

[111] Lu X, Park W K, Kim J-D, Yeo S, Lee S-I and Greene L H 2008 *Physica* B **403** 1098; Lu X *et al.* 2009 in preparation.

[112] Starowicz P, Liu C, Khasanov R, Kondo T, Samolyuk G, Gardenghi D, Lee Y, Ohta T, Harmon B, Canfield P C, *et al.* 2008 *Phys. Rev.* B **77** 134520

[113] Dugdale S B, Utfeld C, Wilkinson I, Laverock J, Major Z, Alam M A and Canfield P C 2009 *Supercond Sci. Technol.* **22** 014002

[114] Baba T, Yokoya T, Tsuda S, Watanabe T, Nohara M, Oguchi H T T and Shin S 2008 arXiv:0812.0406

[115] Kashiwaya S, Tanaka Y, Koyanagi M and Kajimura K 1996 *Phys. Rev.* B **53** 2667

[116] Kamata K, Master thesis, University of Tokyo (2003)

[117] Kamihara Y, Watanabe T, Hirano M and Hosono H 2008 *J. Am. Chem. Soc.* **130** 3296

[118] Kamihara Y, Hiramatsu H, Hirano M, Kawamura R, Yanagi H, Kamiya T and Hosono H 2006 *J. Am. Chem. Soc.* **128** 10012

[119] Ren Z-A, Yang J, Lu W, Yi W, Che G C, Dong X L, Sun L L and Zhao Z X 2008 *Material Research Innovation* bf 12 105

[120] J Yang *et al.* 2008 *Super. Sci. Technol.* **21** 082001

[121] Ren Z-A *et al.* 2008 *Europhys. Lett.* **83** 17002

[122] G Wu *et al.* 2009 *J. Phys: Cond. Matt.* **21** 142203

[123] Rotter M, Tegel M and Johrendt D 2008 *Phys. Rev. Lett.* **101** 107006

[124] Tapp J H, Tang Z, Lv B, Sasmal K, Lorenz B, Chu P C W and Guloy A M 2008 *Phys. Rev.* B **78** 060505(R)

[125] Hsu F-C *et al.* 2008 *Proc. Natl. Acad. Sci.* **105** 14262

[126] Yuan H Q, Singleton J, Balakirev F F, Baily S A, Chen G F, Luo J L and Wang N L 2009 *Nature* **457** 565

[127] de la Cruz C *et al.* 2008 *Nature* **453** 899.

[128] Chen H *et al.* 2009 *Europhys. Lett.* **85** 17006

[129] Yildirim T 2008 *Phys. Rev. Lett.* **101** 057010

[130] Raghu S, Qi X-L, Liu C-X, Scalapino D J and Zhang S-C 2008 *Phys. Rev.* b **77** 220503(R)

[131] Singh D J and Du M-H 2008 *Phys. Rev. Lett.* **100** 237003

[132] Luetkens H *et al.* 2009 *Nature Materials* **8** 305

[133] Zhao J *et al.* 2008 *Nature Materials* **7** 953

[134] Pratt D K *et al.* 2009 arXiv:0903.2833

[135] Mazin I I, Singh D J, Johannes M D and Du M H 2008 *Phys. Rev. Lett.* **101** 057003

[136] Ding H *et al* 2008 *Europhys. Lett.* **83** 47001

[137] Nakayama K *et al* 2009 *Europhys. Lett.* **85** 67002

[138] Kondo T *et al* 2008 *Phys. Rev. Lett.* **101** 147003

[139] Zhao L *et al* 2008 *Chin. Phys. Lett.* **25** 4402

[140] Sebastian S E, Gillett J, Harrison N, Lau P H C, Mielke C H and Lonzarich G G 2008 *J. Phys.: Condens. Matter* **20** 422203

[141] Hashimoto K *et al* 2009 *Phys. Rev. Lett.* **102** 017002

[142] Aczel A A *et al* 2008 *Phys. Rev.* B **78** 214503

[143] Drew A J *et al* 2008 *Phys. Rev. Lett.* **101** 097010

[144] Ren C, Wang Z S, Luo H Q, Yang H, Shan L and Wen H-H 2008 *Phys. Rev. Lett.* **101** 257006

[145] Mu G, Luo H Q, Wang Z S, Shan L, Ren C and Wen H-H 2009 *Phys. Rev.* B **79** 174501

[146] Martin C *et al* 2009 *Phys. Rev. Lett.* **102** 247002

[147] Gordon R T *et al* 2009 *Phys. Rev. Lett.* **102** 127004

[148] Gordon R T, Martin C, Kim H, Ni N, Tanata M A, Schmalian J, Mazin I I, Bud'ko S L, Canfield P C and Prozorov R 2009 *Phys. Rev.* B **79** 100506(R)

[149] Grafe H-J *et al* 2008 *Phys. Rev. Lett.* **101** 047003

[150] Matano K, Ren Z A, Dong X L, Sun L L, Zhao Z X and Zheng G-q 2008 *Europhys. Lett.* **83** 57001

[151] Parker D, Dolgov O V, Korshunov M M, Golubov A A and Mazin I I 2008 *Phys. Rev.* B **78** 134524

[152] Luetkens H *et al* 2008 *Phys. Rev. Lett.* **101** 097009

[153] Christianson A D *et al.,* 2008 *Nature* **456** 930

[154] Chen T Y, Tesanovic Z, Liu R H, Chen X H and Chien C L 2008 *Nature* **453** 1224

[155] Wang Y L, Shan L, Cheng P, Ren C and Wen H H 2009 *Supercond. Sci. Technol.* **22** 015018

[156] Gonnelli R S, Daghero D, Tortello M, Ummarino G A, Stepanov V A, Kim J S and Kremer R S 2009 *Phys. Rev.* B **79** 184526

[157] Samuely P, Szabó P, Pribulová Z, Tillman M E, Bud'ko S and Canfield P C 2009 *Supercond. Sci. Technol.* **22** 014003

[158] Yates K A, Cohen L F, Ren Z-A, Yang J, Lu W, Dong X L and Zhao Z-X 2008 *Supercond. Sci. Technol.* **21** 092003

[159] Daghero D, Tortello M, Gonnelli R S, Stepanov V A, Zhigadlo N D and Karpinski J 2008 arXiv: 0812.1141

[160] Lu X, Park W K, Yuan H Q, Chen G F, Luo G L, Wang N L, Sefat A S, McGruire M A, Jin R, Sales B C, Mandrus D, Gillett J, Sebastian S E and Greene L H 2009 *arXiv:0910.4230*

[161] Chen G L, Li Z, Dong J, Li G, Hu W Z, Zhang X D, Song X H, Zheng P, Wang N L and Luo J L 2008 *Phys. Rev.* B **78** 224512

[162] Wang G T, Qian Y, Xu G, Dai X and Fang Z 2009 arXiv:0903.1385

[163] Szabó P, Pribulová Z, Pristáš G, Bud'ko S L, Canfield P C and Samuely P 2009 *Phys. Rev.* B **79** 012503

[164] Aprili M, Badica E and Greene L H 1999 *Phys. Rev. Lett.* **83** 4630

[165] Sefat A S, Jin R, McGuire M A, Sales B C, Singh D and Mandrus D 2008 *Phys. Rev. Lett.* **101** 117004

[166] Yin Y, Zech M, Williams T L, Wang X F, Wu G, Chen X H and Hoffman J E 2009 *Phys. Rev. Lett.* **102** 097002

[167] Private communication.

[168] Yan J-Q, Kreyssig A, Nandi S, Ni N, Bud'ko S L, Kracher A, McQueeney R J, McCallum R W, Lograsso T A, Goldman A I and Canfield P C 2008 *Phys. Rev.* B **78** 024516

[169] Rotter M, Tegel M, Johrendt D, Schellenberg I, Hermes W and Pöttgen R 2008 *Phys. Rev.* B **78** 020503(R)

[170] Duif A M, Jansen A G M and Wyder P 1989 *J. Phys.: Condens. Matter* **1** 3157

[171] Park J T *et al* 2009 *Phys. Rev. Lett.* **102** 117006

[172] Amato A, Khasanov R, Luetkens H and Klauss H H 2009 arXiv: 0901.3139

[173] Goko T *et al* 2009 *Phys. Rev.* B **80**, 024508

[174] Park W K, Sarrao J L, Thompson J D, Pham L D, Fisk Z and Greene L H 2008 *Phys.* B **403** 731

[175] Liu R H *et al.* 2009 *Nature* **459** 64

[176] Mazin I I and Schmalian J 2009 *Phys.* C **469** 614

[177] Golubov A A, Brinkman A, Tanaka Y, Mazin I I and Dolgov O V 2009 *Phys. Rev. Lett.* **103** 077003

Vita

Xin Lu was born in Xiangfan, Hubei Province of China on July 2^{nd}, 1981. He lived with his parents until he left to attend Xiangfan No. 4 High School in 1996, where he met his wife, Fei. Due to his good performance, he was honored to begin his undergraduate study in Physics at Peking University, China. There, he won Canon scholarship for excellence and Samsung scholarship and started his first research experience of Raman spectroscopic study on GaN nanowires. Meanwhile, he learnt the great opportunity to study abroad in Unite States and prepared the required materials step by step. In 2003, he earned the B. S. degree and flied far way to America to continue his study of Physics at University of Illinois at Urbana-Champaign. Initially, he worked with Prof. James Wolfe on the project of Phonon Imaging of Pb and was attracted to the exciting property of superconductors. He officially joined Prof. Laura Greene's group to focus on the application of point-contact Andreev reflection and planar tunneling spectroscopy in various types of superconductors. This work continued until he received his Ph. D degree and found a post-doc position in Los Alamos national lab at the end of 2009.